José Diogo Gonçalves de Carvalho

Suspension Parameters Analysis for Different Track Conditions
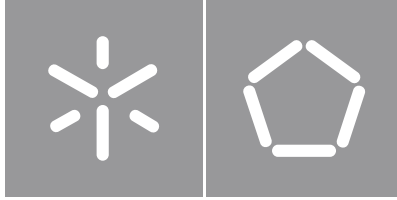
dezembro de 2021

Universidade do Minho
Escola de Engenharia

José Diogo Gonçalves de Carvalho

Suspension Parameters Analysis for Different Track Conditions

Dissertação de Mestrado
Mestrado Integrado em Engenharia Mecânica
Sistemas Mecatrónicos

Trabalho efetuado sob a orientação de
Professor Doutor João Paulo Flores Fernandes
Professor Doutor Pedro Filipe Lima Marques

dezembro de 2021

Direitos de Autor e Condições de Utilização do Trabalho por Terceiros

ACKNOWLEDGMENTS

After an atypical year of working on this dissertation, I would like to show my gratitude towards those who have accompanied me along this journey.

To my supervisor, Professor Filipe Marques, for his full commitment and his willingness to share his knowledge with me. No doubt, without his dedication and attention to detail, this project would not have panned out as well as it did.

To my parents and my sister, Elisa, for their love, patience, and support across my life.

And finally, to all my friends, new and old, for all the great moments over these last 5 years.

STATEMENT OF INTEGRITY

I hereby declare having conducted this academic work with integrity. I confirm that I have not used plagiarism or any form of undue use of information or falsification of results along the process leading to its elaboration.

I further declare that I have fully acknowledged the Code of Ethical Conduct of the University of Minho.

STATEMENT OF INTEGRITY

RESUMO

Este trabalho, aqui apresentado, tem como objetivo o estudo do comportamento do sistema de suspensão de um veículo ao atravessar estradas com obstáculos, como lombas ou buracos.

Para atingir este objetivo, uma vasta revisão literária foi feita. Sendo este um tópico extenso, três tipos de revisão foram feitos. Primeiro, a um estudo global à tecnologia usava hoje em dia em pneus e nos sistemas de suspensão de veículos foi compilado. Uma breve menção à cinemática de veículos é empreendida. De seguida, a dinâmica do contacto pneu/solo é sistematicamente explanada, para compreender os diversos modelos de pneu (força) existentes. Adicionalmente, os conceitos fundamentais da análise da dinâmica multicorpo são expostos para justificar a modelação do veículo como um sistema multicorpo.

Com toda a teoria apresentada, os conceitos previamente explicados são aplicados na prática para a formulação de um método que visa estimar a trajetória de um veículo atravessando uma qualquer estrada. O primeiro passo a executar é a escolha do modelo de pneu a utilizar. Percebe-se que se deve usar modelos matemáticos, culminando na escolha da *Magic Formula*. Os passos seguintes consistem na introdução de uma metodologia, que estima o contacto entre um pneu e o solo, para simular as dinâmicas pneu/solo de um veículo. Dois métodos diferentes são expostos: o primeiro para estradas completamente planas, sem obstáculos; o segundo, para estradas com obstáculos, como lombas ou buracos. Este modelo é posteriormente inserido num programa de análise das dinâmicas multicorpo, MUBODYNA3D, e diversas simulações são realizadas.

Estas simulações começam pela definição do veículo como um sistema multicorpo, com corpos conectados por juntas cinemáticas. As primeiras simulações são realizadas numa estrada plana para validar os modelos e metodologias previamente criadas. O integrador, que integra os resultados das equações do movimento para prever a trajetória, é refinado. Finalmente, simulações com estradas com obstáculos são geradas.

Por fim, os resultados dessas simulações são discutidos, percebendo-se que apresentam um valor inesperado. Ao atravessar um obstáculo, as rodas perdem o contacto com a superfície, provocando a descolagem do carro. No entanto, é concluído que a análise de sistemas multicorpo é de extrema relevância para a simulação de realidades complexas, produzindo resultados precisos.

Palavras-chave

Dinâmica de veículos; Estimativa do contacto; Modelo de pneu; Simulações; Sistemas multicorpo

ABSTRACT

This work, hereby presented, has a primary target of studying the behaviour of a road vehicle's suspension system, while it is traversing roads with big obstacles, such as potholes or speed bumps/humps.

To accomplish this task, a broad literature review was made. Since this is an extensive topic, three types of review were made. Firstly, an overview of the state-of-the-art technology used in tires and suspension systems nowadays is compiled. A brief mention to vehicle kinematics is also made. Then, the dynamics of the contact tire/road are systematically explained, in order to understand the diverse tire force models that exist. Lastly, a rundown of the fundamental concepts of multibody dynamics analysis is exposed to substantiate the modelling of a vehicle as a multibody system later on.

With the theory behind, all concepts previously abridged are put to practice, into the formulation of a method to estimate the trajectory of a vehicle crossing a certain road. The first step to execute this is to choose the tire force model to use. It is seen that, in this case, the mathematical models are the best choice, which culminates in the selection of the Magic Formula model. The following steps consist of introducing the contact estimation methodology created to simulate the tire/road dynamics of a vehicle. Two different methods are exposed: the first for fully flat roads, with no obstacles; the second, for road that possess obstacles, like bumps for example. This model is then inserted into a multibody dynamics analysis program, MUBODYNA3D, and some forward dynamic simulations are performed.

These simulations start with the definition of the vehicle as a multibody system, with bodies connected by kinematic joints. The first simulations are performed in flat roads to validate the models and methodologies created. The solver, that integrates the results of the equations of motion to predict the trajectory, are then refined. Finally, simulations using roads with obstacles are conducted and the results analysed.

In the end, the simulations result in some unexpected behaviour from the vehicle. While crossing an obstacle, it tends to lose contact with the surface and, thus, lift off the road, which is unrealistic. Nonetheless, it is concluded that multibody systems analysis is extremely important to simulate and analyse complex realities, with precise results.

Keywords

Contact estimation; Multibody systems; Simulations; Tire force model; Vehicle dynamics

TABLE OF CONTENTS

LIST OF TABLES

LIST OF SYMBOLS

Chapter 2

Latin symbols

Symbol	Unit (SI)	Description
$c_{\alpha,v,h}$	N/m	Lateral stiffness of the tire
$l_{v,h}$	m	Distance to the vehicle's centre of mass
m	kg	Tire's mass
v	m/s	Vehicle's velocity

Greek symbols

Symbol	Unit (SI)	Description
β	rad	Side slip angle
δ	rad	Steering angle
ψ_v	rad	Heading angle
$\dot{\psi}_v$	rad/s	Yaw rate

Chapter 3

Latin symbols

Symbol	Unit (SI)	Description
A	-	Bristle exit point
b	m	Width of the contact patch
c_z	N/m	Tire radial stiffness
c_s	N/m	Tire longitudinal stiffness
c_α	N/m	Tire lateral stiffness

E	-	Bristle entry point
e	m	Displacement of the point of application of forces
F	N	LuGre friction force
F_C	N	Coulomb friction force
F_S	N	Striction force
F_x	N	Tire longitudinal force
F_y	N	Tire lateral force
F_Z	N	Tire vertical load/force
G_s, G_α	-	Dugoff modifying factors
g	-	LuGre function
k	-	Tread constructive characteristics
k_r	-	HSRI adhesion factor
L	m	Contact patch length
M_x	N·m	Overturning couple torque
M_y	N·m	Rolling resistance torque
M_z	N·m	Self-aligning torque
n_R	m	Variation of the tire caster angle
p_z	N/m	Pressure distribution
r	m	radius
r_0	m	Tire nominal radius
r_{dyn}	m	Tire dynamic radius
r_{stat}, r_s	m	Tire static radius
s, s_A, s_B	-	Longitudinal slip
S_R	-	HSRI comparison factor
t	s	Time

u, u_{max}	m	Deformation of the brush element
V	m/s	Velocity of the wheel's centre
V_G	m/s	HSRI sliding velocity
V_P	m/s	Velocity at the contact point
V_x	m/s	Longitudinal component of the tire's velocity
V_y	m/s	Lateral component of the tire's velocity
v_r	m/s	LuGre relative velocity between two surfaces
v_s	m/s	Stribeck velocity
z	m	LuGre vertical displacement of the bristle

Greek symbols

Symbol	Unit (SI)	Description
α	rad	Slip angle
λ	-	Dugoff factor
δ	-	Stribeck exponent
δ_Z	m	Tire deflection
μ	-	Coefficient of friction between tire and road
μ_G	-	Sliding coefficient of friction
μ_H	-	Adhesion coefficient of friction
μ_{max}	-	Maximum coefficient of friction
σ_0	N/m	LuGre Stiffness coefficient
σ_1	N/m	LuGre Damping coefficient
σ_2	Ns/m	LuGre Coefficient of viscosity
τ_x	N/m^2	Brush element longitudinal shear stress
τ_{xG}	N/m^2	Sliding shear stress

Symbol	Unit (SI)	Description
τ_{xH}	N/m^2	Adhesion shear stress
τ_y	N/m^2	Brush element lateral shear stress
ω	rad/s	Tire angular velocity

Chapter 4

Latin symbols

Symbol	Unit (SI)	Description
A	-	Transformation matrix
D	-	Jacobian matrix of the constraint equations
d_c	-	Damping coefficient for Penalty and Augmented methods
e_0, e_1, e_2, e_3	-	Euler parameters
g	N, N·m	Vector of generalized forces
$\mathbf{g}^{(c)}$	N, N·m	Vector of constraint reaction forces
k_c	-	Stiffness coefficient for Penalty and Augmented methods
M	kg, kg·m^2	Global mass matrix
m	-	Number of independent constraints
m_c	-	Mass coefficient for Penalty and Augmented methods
n_b	-	Number of bodies
n_{DoF}	-	Number of degrees of freedom
P	-	Point fixed in the local system
p	-	Euler parameters vector
q	-	Vector of generalized coordinates
$\mathbf{q}^{(c)}$	-	Corrected vector of generalized coordinates
r	-	Global position vector
s	-	Global position vector on local coordinate system

$\mathbf{s}'$	-	Local position vector
t	s	Time
$\mathbf{u}$	-	Dependent coordinates vector
$\mathbf{u}_\xi, \mathbf{u}_\eta, \mathbf{u}_\zeta$	-	Unit vectors to define the transformation matrix
$\mathbf{v}$	m/s, rad/s	Vector of generalized velocities
$\dot{\mathbf{v}}$	m/s^2, rad/s^2	Vector of generalized accelerations
$\mathbf{v}^{(c)}$	m/s, rad/s	Corrected vector of generalized velocities
xyz	-	Global coordinate system
y_t	-	Auxiliary vector

Greek symbols

Symbol	Unit (SI)	Description
α, μ, ω	-	Coefficients for the Penalty and Augmented methods
$\boldsymbol{\gamma}$	-	Right-hand side vector of the accelerations constraint
$\delta\mathbf{q}$	-	Vector to correct the initial positions
Δt	s	Timestep
$\boldsymbol{\lambda}$	-	Lagrange multipliers vector
ε	-	Tolerance to solve the equations of motion
$\boldsymbol{\Phi}$	-	Vector of kinematic constraints
Φ	rad	Angle to get the Euler parameters
$\xi\eta\zeta$	-	Body-fixed (local) coordinate system
ω	rad/s	Angular velocities vector

Chapter 5

Latin symbols

Symbol	Unit (SI)	Description
$\mathbf{A}$	-	Transformation matrix
a_1, a_2	N/m	TMeasy vertical model coefficients
C_1	N/m	Tire radial stiffness at the nominal load
C_2	N/m	Tire radial stiffness at double the nominal load
c	Ns/m	Damping coefficient
$C_{spx1,2,3,4}$	-	One-dimensional longitudinal spline coefficients
$C_{spy1,2,3,4}$	-	One-dimensional lateral spline coefficients
$C_{x1,2,3,4}$	-	Longitudinal road spline coefficients
$C_{y1,2,3,4}$	-	Lateral road spline coefficients
$\mathbf{d}$	m	Distance vector
d	m/s^2	Deceleration
$\mathbf{d}_x, \mathbf{d}_y, \mathbf{d}_z$	-	Global direction vectors at a certain timestep
F	N	Point-to-point force
F_B	N	Braking force
F_x	N	Tire/road longitudinal force
F_y	N	Tire/road lateral force
F_Z	N	Tire/road contact vertical force
F_{Z0}	N	Nominal tire load
f	m	Tire profile vertical coordinate
$\mathbf{f}_i$	N	Force vector
H	m	Height of the obstacle
k	N/m	Spring stiffness

L	m	Road length
L_b	m	Length of the obstacle
M_x	N·m	Overturning couple torque
M_y	N·m	Rolling resistance torque
M_z	N·m	Self-aligning torque
m_c	kg	Mass of the vehicle
$\mathbf{m}_i, \mathbf{T}$	N·m	Torque vector
$\mathbf{n}$	-	Normal vector to the road
$\mathbf{p}$	-	Iterated vector by *fsolve*
p_x, p_y	-	Road profile gradients
$\mathbf{r}$	-	Global position of the wheel's centre of mass
$\dot{\mathbf{r}}$	-	Global velocity vector
$\mathbf{r}^{A_{1,2,3}}$	-	Global location of the approximation points
$\mathbf{r}^{CP}$	-	Global position of the projected contact point
$\mathbf{r}^P$	-	Global position of the effective contact point
$\mathbf{r}^{y_Q}$	-	Global location of the point of application of forces
r_0	m	Tire nominal radius
r_{dyn}	m	Tire dynamic radius
r_s	m	Tire static radius
s	-	Longitudinal slip
$\mathbf{s}$	-	Global rotation axis vector
$\mathbf{s}_p$	-	Local rotation axis vector
SP_x	-	One-dimensional longitudinal spline
SP_y	-	One-dimensional lateral spline
$\mathbf{spl}_x$	-	Longitudinal spline for the road profile

$\mathbf{spl}_y$	-	Lateral spline for the road profile
t	s	Time
$\mathbf{t}_G$	-	Tolerance vector
$\mathbf{t}_x, \mathbf{t}_y$	-	Tangential vectors to the road
u	m	Tire profile longitudinal coordinates
$\mathbf{u}_l \mathbf{su}_v$	-	Fixed local coordinate system
$\mathbf{V}$	m/s	Velocity vector
V_i	m/s	Initial velocity
V_f	m/s	Final velocity
$\mathbf{V}_T$	m/s	Wheel's real velocity vector
$\mathbf{V}_x$	m/s	Longitudinal velocity
$\mathbf{V}_y$	m/s	Lateral velocity
W	m	Road width
xyz	-	Global coordinate system
$x_{\mathrm{bin}}, y_{\mathrm{bin}}$	-	Spline's endpoints coordinates given by *histc*
x_i, y_i	m	*fsolve* initial approximations
x_p, y_p	m	*fsolve* iterated coordinates
$x_{\mathrm{pf}}, y_{\mathrm{pf}}$	m	Final calculated coordinates of the contact point
$\mathbf{x}_{pts}$	-	Local longitudinal coordinates of the road profile
$\mathbf{y}_{pts}$	-	Local lateral coordinates of the road profile
z_p	m	Contact point iterated vertical coordinate
z_{pf}	m	Contact point vertical calculated coordinate
z_{px}, z_{py}	m	Interpolated vertical coordinates
$\mathbf{z}_{sx}$	-	Vertical matrix for the longitudinal splines

Symbol	Unit (SI)	Description
$\mathbf{z}_{sy}$	-	Vertical matrix for the lateral splines

Greek symbols

Symbol	Unit (SI)	Description
α	rad	slip angle
Δt	s	Timestep
δ	m	Spring deformation
δ_i	m	Spring undeformed length
δ_x	m	Approximation tolerance
δ_Z	m	Tire deflection
δ_{Z0}	m	Tire static deflection (at nominal load)
θ	rad	Angle between the velocity vector and the rotation axis
θ_x, θ_y	rad	Gradient of the road
μ	-	Coefficient of friction between tire and the road
$\xi\eta\zeta$	-	Local coordinate system
τ_A	N·m	Acceleration torque
τ_{AW}	N·m	Acceleration torque for one wheel
τ_W	N·m	Braking torque
$\boldsymbol{\omega}$	rad/s	Wheel's angular velocity vector
ω	rad/s	Angular velocity
ω_r	m/s	Angular velocity represented as a linear velocity
ω_s	rad/s	Angular velocity around the global axis of rotation

Chapter 6

Latin symbols

Symbol	Unit (SI)	Description
e_0, e_1, e_2, e_3	-	Euler parameters
E_m	J	Mechanical energy of the vehicle
F_x	N	Longitudinal tire force
F_y	N	Lateral tire force
F_Z	N	Vertical tire force
g	m/s^2	Gravitational acceleration
L_{road}	m	Road length
r_0	m	Tire nominal radius
$\mathbf{r}_{in}^k$	-	New global position of any point within the vehicle
$\mathbf{r}_{io}^k$	-	Original global position of any point within the vehicle
t	s	Time
t_f	s	Time of simulation
$V_{2.5s}$	m/s	Velocity at $t = 2.5$s
V_f	m/s	Velocity at the end of the simulation
V_0	m/s	Initial velocity
W	m	Road width
xyz	-	Global coordinate system
x_f	m	Final longitudinal position of the front-left wheel
x_i	m	Initial longitudinal position of the front-left wheel
z_c	m	Vertical translation
$z_{chassis}$	m	Vertical coordinate of the chassis

Greek symbols

Symbol	Unit (SI)	Description
δ_Z	m	Tire deflection
δ_{Z0}	m	Initial tire deflection
δ_{Zf}	m	Tire deflection at the end of the simulation
μ	-	Coefficient of friction between tire and road
$\xi\eta\zeta$	-	Local coordinate system
τ_a	N·m	Acceleration torque
τ_b	N·m	Braking torque
ω_0	rad/s	Initial angular velocity

C

Camber angle	Angle between the wheel vertical plane and the vertical plane of the vehicle, which is perpendicular to the road.
Caster angle	Angle between the steering axis and the vertical axis of the wheel, when looking from the side of the car. A positive caster keeps the tire straight, by creating a torque that opposes the steering input when the steering wheel is let go of.
Contact patch	Area of a tire that is in contact with the road at a certain point in time.

H

Holonomic constraint	Geometric constraint that is integrable into a form that only involves coordinates.

N

Nonholonomic constraint	Constraint that is not integrable.

O

Oversteer	When the rear tires slip angle is greater than the front tires slip angle. Happens when the rear tires are overloaded, causing the rear tires to slide out. The turning travelling path would become much sharper than the intended one

R

Rheonomic constraint	Constraint that is an explicit function of time.
Rolling resistance	On a tire, it can be defined as the energy loss per distance travelled.

S

Self-aligning torque	Torque generated by the tire as it rolls. It tends to restore the alignment of a tire back to a zero-slip angle situation.
Scleronomic constraint	Constraint that is not an explicit function of time. Its equation is described by generalized coordinates.
Slip	Relative motion between the tire and the surface it is traversing.
Slip angle	Angle between the direction of the wheel's centre velocity and the longitudinal axis of the tire.

T

Toe angle	Angle between the wheel's longitudinal axis and the vehicle's longitudinal direction.

U

Understeer	When the front tires slip angle is greater than the rear tires slip angle. Happens when the front tires are overloaded (when accelerating and turning at the same time), causing the travelling path to be much wider than the one desired. On a limit case, the turning radius of the car would become infinite.

1. INTRODUCTION

In the first chapter of this work, the dissertation done across several months will be introduced. This chapter begins with an overview and the scope of this thesis, while specifying the objectives and methods used across this work.

1.1   Motivation and Scope

An automobile's suspension system determines the comfort level and, also, the safety level that a vehicle provides to the passengers (Schramm et al., 2014). Over the years, automobiles in general have evolved like no other technology. From the first cars with wooden wheels and no suspension whatsoever to the modern state-of-the-art performance cars, the automobile industry is always adapting to new technologies and necessities. Look at the Anti-lock Braking System (ABS) design in the 1970's to stop the blocking of the wheels during braking and avoid sliding (Burton et al., 2004). Once a novelty not available to all, now a guaranteed system in every single modern car. The automotive industry is constantly changing.

To ensure a safe and comfortable drive, it is essential to quantify the driving safety, stability, and comfort by studying the dynamics of road vehicles. Other kinds of vehicles, such as off-road and competition vehicles, usually discard most of the comfort to obtain maximum performance. Nevertheless, the dynamics of road vehicles must be studied in order to evaluate their performance when subject to dynamic solicitations. These can be external, like the shape of the road, sometimes flat, sometimes with obstacles like bumps or potholes; or internal, usually promoted by the driver's actions, such as steering inputs.

To study the effect of dynamic solicitations on a vehicle's performance, big and expensive test rigs must be used. This type of equipment is extremely expensive, which makes testing a very financially demanding exercise. Hence, new solutions needed to be implemented. To study and project the subsystems that compose a vehicle, computational methodologies have been used for some time. These are getting better as computational advancements are being made, which makes them able to give precise and reliable results. One of those computational techniques is known as multibody dynamics, that have been growing substantially (Blundell & Harty, 2004). These consist of characterizing a mechanism, comprised of multiple bodies, as a system with multiple bodies connected by kinematic joints, that restrain the movement (Flores P. , 2015). To simulate a certain multibody system, all bodies

must be defined, as well as the elements that connect them and all the external and internal forces acting. With a good computational simulation, a vehicle under dynamic solicitations is easily studied, and the results obtained can be transcribed and compared to reality.

In this work, it is intended to study the influence of the suspension parameters on a vehicle's behaviour, when it is crossing a road with obstacles, like bumps or potholes. For that purpose, it is necessary model the vehicle as a multibody system, discretising several types of suspension and representing forces always acting on a tire, obtaining in the end a sensibility study of the parameters that mostly influence the results.

1.2   State of the Art

Vehicle modelling and simulation has been around for quite a few years now, and the literature and methods available are extensive. From Chapter 2 to Chapter 4 of this work, the state of the art for vehicle dynamics, multibody dynamics and simulation will be thoroughly clarified, so there is no need to introduce it here. Nevertheless, it is necessary to highlight some of the most important literature used in this work.

Vehicle dynamics have been studied ever since the inception of the very first vehicle, which makes them integral to this specific work. General topics about vehicles, its components and kinematics have been derived from works such as (Guiggiani, 2014; Schramm et al., 2014; Reimpell et al., 2001). These are particularly relevant to understand the composition of a vehicle, how it is made and how the components act together. (Schramm et al., 2014; Guiggiani, 2014) are extremely insightful into the constructive principles and types of tires, usually stating that a tire is a cluster of radial layers covered by an elastic tread of rubber, which allows the contact with the road. As for the various types of suspensions, its historical evolution, and some constructive principles, (Reimpell et al., 2001; Schramm et al., 2014) are cited. In short, there are multiple types of suspensions systems, but only some of them are relevant these days, such as the Macpherson (Dehbari & Marzbanrad, 2018) strut or the multilink axle (Schramm et al., 2014). Following this, some vehicle kinematics are presented, mainly based on (Schramm et al, 2014; Guiggiani, 2014). The last two sources provide an excellent overview of two-dimensional models used to characterize vehicle kinematics, such as the bicycle model. Other authors, such as (Zhou & Liu, 2010; Hu et al., 2019) extend these concepts and present more complex kinematic configurations, like the 7 DoF model, that considers all four wheels of the car. These models are relevant to the study of yaw motions (Schramm et al., 2014).

As for general comprehension of the tire/road dynamics, (Schramm et al., 2014) is a relevant reference. It provides all the information necessary to understand the steady-state generation of frictional

forces in the contact patch between the rubber and the road. Briefly, the contact between tire and road generates a normal force that consequently creates two other forces in the lateral and longitudinal direction, dependent on quantities of slip. This is seen by using the Brush model, that physical explains why these forces exist (Schramm et al., 2014; Mavros et al., 2005). However, the Brush model paved the way to the creation of several other models, utilized in computational scenarios that can predict faithfully the behaviour of the contact in certain conditions. One of the first models to be used in the industry was the Dugoff Model (Dugoff et al., 1969). Several changes have been made to it over the years, culminating in a modified model, by (Bian, 2014; Bhoraskar & Sakthivel, 2017). Nevertheless, the staple of all models is the Magic Formula, by Hans B. Pacejka (Bakker et al., 1987; Bakker et al., 1989; Pacejka, 2002). This is a semi-empirical model that faithfully recreates the steady-state behaviour of a tire, under normal loads. Other works have been created over the years, creating more diverse and complex models that can predict a dynamic/transient behaviour of the tire. Refer to (A.J.C. Schmeitz; Besselink, 2004; Canudas-de-Wit T. V., 2002; Hoogh, 2005; Korunovic et al., 2008; Svendenius, 2007; Rill & Castro, 2020).

Since the car must be studied as a multibody system, considerations about the multibody formulation were derived mainly from (Flores P. , 2015; Nikravesh P. E., 1988; Nikravesh, 2007). The methods to resolve the equations of motion, such as the augmented Lagrangian method are thoroughly explained in (Marques et al., 2017; Flores P. , 2015). Still, about the car as a multibody dynamic system several works have been done over the years, especially considering (Ambrósio & Verissimo, 2009), where the behaviour of joints under different car manoeuvres was analysed. Blundel & Harty (2004) presented a multibody approach to the dynamics of vehicles, which is an extensive collection of data for such type of simulations. Other works, such as (Hegazy et al. , 2000; Schramm et al., 2014), must also be considered to study the vehicle as a multibody system.

To create a simulation, based on concepts present in the previous references, (Flores P. , 2012) was used. Some mathematical and numerical concepts, innate to software used to simulate the multibody system can be found in (A. Keller, 2018; Kahaner, 1988). To clarify some expectable results and conclusions (Filipozzi et al., 2021; Garcia-Pozuelo et al., 2015) were used. In these articles similar cases of study were analysed, when it comes to the generation of vertical force and bump modelling.

1.3 Objectives

In this work, it is expected to study complex multibody models of road vehicles, mainly cars through the development of advance techniques of automotive modelling.

Firstly, it is necessary to get a good familiarization with the spatial multibody dynamics methodology. This is of extreme relevance to understand and develop dynamic models of vehicles. Also, to fully understand how a vehicle behaves dynamically, it is imperative to study the different types of tire/road contact models. The forces generated in the contact patch can heavily influence the dynamic behaviour of a car's suspension system and, therefore, the right contact model must be chosen. It is also expected to see the connection between the contact forces and the suspension behaviour.

To study the dynamics between tire and road, a dynamic model must be created, using programming tools such as MATLAB. A program for MATLAB known as MUBODYNA3D (Flores P. , 2012) will be used to perform three-dimensional multibody simulations. The simulation model must be comprised of the multibody model of the vehicle, the contact forces model, and some miscellaneous codes, like the road and the tire profile. The roads should start as fully flat and gradually move on to ones with obstacles, like potholes and bumps.

Finally, in the end of this work, it is expected to analyse the dynamics the vehicle in the face of imposed solicitations to its suspensions system, having always in mind the different models and the obstacles that can be found in a road.

1.4   Structure of the Dissertation

This dissertation is divided into 7 chapters. Each chapter is divided into sections and subsections as will be seen below.

Chapter 1 is the introductory stage of this work. It highlights its purposes and objectives, while presenting a general overview of the dissertation.

In Chapter 2, a literature review on the modern vehicle is presented. This chapter focusses on the tire and the suspension system of vehicles, the two most crucial components for this work. Additionally, some a brief overview of vehicle kinematics is made.

Chapter 3 is also a literature review. It describes the fundamental dynamics between a tire and the road. It gives a brief physical explanation to the phenomena that acts on a tire, while also presenting several ways to model these dynamics.

In Chapter 4, a brief discussion about multibody dynamics is made. The fundamental concepts about the modelling of multibody systems and how to predict their behaviour across time are introduced. This chapter is particularly important to understand the simulations made in this work.

In Chapter 5, the computational work starts. Here, the methods used to simulate a car going over a road are fully explained. Firstly, the choice of tire model is justified. Then, the simulator used is presented

and its method explained. Finally, a model to estimate the contact between the tire and the road is created for both flat and uneven roads.

In Chapter 6, the methodologies and algorithms created before are tested, in a number of different numerical simulations. Some computational experiments are done to validate the concepts introduced before and the behaviour of the suspension system across different roads is examined.

Chapter 7 presents the outcomes and conclusions of this work, as well as the limitations found and suggestions for future works.

1.5   Contributions

This work succinctly describes and gives a general overview of the tire/road dynamics and how those could be connected to the simulation and analysis of multibody systems. A vehicle is just that: a number of components connected via kinematic joints that imposed restrictions on the movement of the bodies.

This work firstly provides an overview of some of the most important literature about vehicle dynamics with focus on the frictional contact dynamics. The tire/road contact is thoroughly overviewed, and some of the most relevant models to describe it are presented. Also, a general overview of multibody dynamics is presented, while explaining some methods to solve the equations of motion and predict the trajectory of multibody systems.

Furthermore, the concepts studied before are applied and a contact model is created, its algorithm dissected. In short, a tire/road contact model is implemented and through an "in-house" 3D multibody dynamics code, the contact between tire and road is detected. This is used to calculate the forces and contact point of a vehicle's tires, to be used on multibody simulations. These simulations are done to validate the models created and to study the influence of suspension parameters on the vehicle's behaviour over roads with obstacles.

2. The Vehicle

Modern vehicles have come a long way since their inception. In less than a century, the main means of transportation evolved from animal pulled carriages to cars. Even cars mutated across time, being simple mechanisms with wooden wheels to state-of-the-art super-cars that can travel at 300 km/h. Components such as the engine, the wheels and the suspension system have also come a long way, although their function fundamentally remained the same. For example, the engine has always been the main power source of the car, where fuel is transformed in mechanical energy that can imprint movement to the vehicle. The tires, once simple wheels of wood and now extremely complex components made of rubber, have always been responsible for the creation of a platform for that power to be transmitted to the road. In short, the fundamental functions of these components and systems that make a car has never really changed.

In this chapter, the state of the art of modern vehicles will be presented. Since this work relies heavily on tires and the suspensions system, only those two components will be discussed. To know more about all the other systems that compose a road vehicle, consult (Schramm et al., 2014).

2.1 The Tire

Since the early days of vehicle mobility, the tire has always been a crucial component to the good functioning of wheeled vehicles. Although not always made of rubber, one can affirm that the tire has always had this one specific function: to create a connection between a vehicle and a surface.

The development of the automotive industry has undoubtedly promoted the evolution of the tire: from the iron that was placed on wooden wheels built into carriages, to the bands of leather used on the first automobiles to protect wooden rims, converging at the creation of the pneumatic tire, made of rubber, by Robert William Johnson in 1845. Of course, as history repeats itself, the first attempt at the creation of the rubberized inflatable tire was unsuccessful, being that the tire created by Johnson was too expensive. Another attempt was made, this time by John Dunlop, and even though it turned out quite successful, Dunlop's pneumatic tire patent was intended for bicycle use. The first people to implement a pneumatic tire on an automobile were the Michelin brothers, but theirs turned out to be flimsy. The broad use of the pneumatic tire on automobiles was only possible by 1911, when Philip Strauss created the combination of tire and air inner-filled tube (Bellis, 2014).

Nowadays, almost all road vehicles have pneumatic tires covering a system that is called "wheel". In fact, the development of the tire throughout the years, has promoted the conception of fast and comfortable road vehicles (Schramm et al., 2014).

Before studying the specific details of the pneumatic tire, one should first establish the wheel as an apparatus of its own. The wheel is defined as the system that encompasses the rotating components of the vehicle undercarriage that spin around the wheel axis (Schramm et al., 2014). The so-called system encloses components like the wheel carrier, the rim, rotating parts of the braking system, parts of the driveshaft and drivetrain and the tires.

Even though an isolated system of its own, the wheel can be considered as an integral part of two different subsystems: the suspension and the drivetrain, being that both subsystems convey severely different functions. Anyhow, in each case, it represents the vehicle's interface with the road (Schramm et al., 2014). Each vehicle has a set of wheels, usually four for cars (trucks might possess more than four wheels), with a set of properties, such as absorption of loads, protection of some components, protection of the passengers from impacts, transmission of acceleration and braking forces and forces generated during cornering (Schramm et al., 2014)

Now that the concept of wheel has been introduced, it is important to focus on the tire. The tire can be defined as a "ring-shaped component that surrounds a wheel's rim to transfer a vehicle's load from the axle through the wheel to the ground and to provide traction on the surface over which the wheel travels" (Tire, 2021).

Tires, nowadays with pneumatic characteristics and made of rubber, are fundamental elements that ensure the vehicle's contact with the road, making the transmission of multidirectional forces possible. Some of its main features are the flexibility and the low mass, that allow for the contact with the road the be maintained, even on uneven surfaces. The rubberized layers ensure high grip. It is then possible to assume that the tires significantly affect the handling properties of vehicles, making them complex viscoelastic components with nonlinear behaviour and dynamic characteristics.

Nowadays, there is a variety of types of tires, specifically constructed for different purposes. Each type of vehicle is dependent on a specific set of tires. However, some characteristics, or constructive requirements, are widely shared throughout the big catalogue of these rubberized components (Schramm et al., 2014):

- Driving safety
- Handling
- Comfort

- Service life

Obviously, even these requirements differ from one tire to another. A truck's tire should have a much bigger service life that a passenger car's tire, but this only happens because the vehicle, in a way, has a different task to fulfil. The principle behind a truck and a car is fundamentally the same, so one can consider some of these requirements to be similar, while they ultimately end up performing the exact same task: providing a contact surface with the road.

This contact surface is of extreme importance (it will be mentioned throughout this work) and is often called the tire "contact patch". To fully understand this concept, one can regard the contact patch as the footprint of the tire, which is merely the area of the tread that is contact with the road. It is where all the forces and torques, created between the tire and the road, are transmitted via pressure and friction (Guiggiani, 2014).

A tire should be able to provide several properties, so that a vehicle's handling is safely executed. Firstly, a tire must yield a high coefficient of friction in each operating condition, as well as a good cornering stability, which is achieved by securing a steady build-up of lateral forces without any sudden changes (Guiggiani, 2014). Also, a tire, together with the drivetrain and steering system, must have a direct and immediate response to steering inputs. Finally, a tire must keep its properties at a sustained maximum speed, while only exhibiting small fluctuations in wheel load. Additionally, a tire must provide, on its own, good suspension and damping properties and a long-term durability, guaranteeing a high-level of riding comfort (Schramm et al., 2014). The aforementioned characteristics can be modified to any specific case, which may vary from vehicle to vehicle. Nevertheless, they represent the starting point, from where a tire should be designed.

To study, both physically and mathematically a tire, it is of most relevance to understand its basic construction principles. A tire, depicted in Figure 2.1, is built from several different layers which can be stacked up in different ways, such as radially or diagonally. Nowadays most tires are built upon the radial layers' basis. Nonetheless, both constructive principles share some similarities as the basic tire constitution.
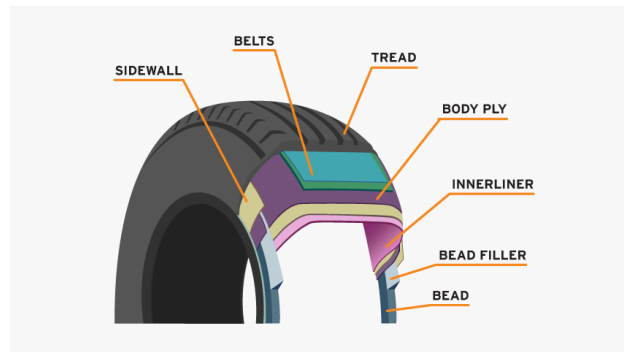
Figure 2.1 - Different layers that compose a radial-ply tire.

A tire is primarily a highly composite structure and can be considered as a carcass of flexible cords encased in a matrix of soft rubber, inflated with air. It can change along the bead relevant actions with the rim, which is always said to be rigid. This results in actions such as traction, braking, steering and load support. Also, air pressure is used to increase the structural stiffness of the tire, so that the highest the air pressure, the lower the sidewall bending (Guiggiani, 2014). A tire is made of 4 primary layers (Schramm et al., 2014):

- **Tread**: made of rubber. Contains the tread profile, which is the pattern that can be seen on the exterior lateral side of the tire.
- **Carcass**: assembled of tensile surfaces covered in rubber. Alongside with the tire's pressure, it provides the necessary strength.
- **Belt**: layer of steel that rests on the surface of the carcass. Encloses the tire from the outside and gives the tread its strength.
- **Bead rings**: ensure a tight fit of the tire on the wheel and guarantee a seal between the tire and the rim.

The tire's design includes two different types: diagonal layers, also known as cross-ply tires, and the radial-ply tires, both being depicted in Figure 2.2.
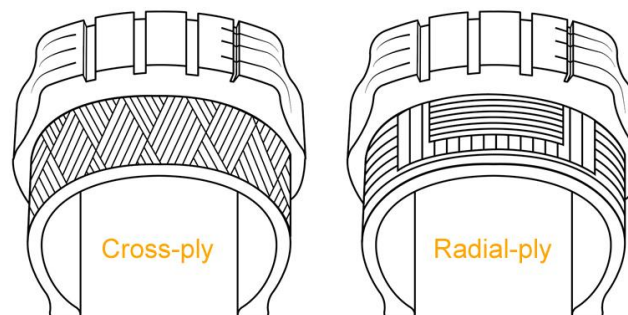
Figure 2.2 - Types of tire designs. Adapted from *(ProTyre's website, s.d.)*.

As for the cross-ply tires, the layers of the tire are placed diagonally across each other at a certain angle to the centre plane of the tire. The carcass has two layers of rubberized cord fibres, made of rayon, nylon or even steel cord. At the feet of the tire, the ends of these layers are wrapped around the core of the tire bead on both sides, and two wide rings, along the folded ends of the layers form the bead, that is the frictional connection, or seat, to the rim (Reimpell et al., 2001). The tread is then applied to the outer diameter of the structure. On the tire's side, the tread blends into the shoulder, which is connected to the sidewall that protects the tread itself. Both shoulder and sidewall, in this case, are made of rubber blend since these layers are barely subjected to wear.

It should be noted that cross-ply tires are no longer used on passenger cars, though they can still be found in some different cases, such as spare tires, racing cars, due to the lower moment of inertia, or agricultural vehicle, which do not need to reach great travelling speeds.

On the other end of the spectrum, radial-ply tires are the most commonly found in modern vehicles. As the name implies, all layers are constructed radially, making them independent features that grant more flexibility to absorb shocks generated by the contact with the road.

In radial tires, two bead cores are joined together via the carcass, which is usually made of rayon or nylon. The interior side of the tire consists of a belt of steel cords, which provides the necessary stiffness to handle all road obstacles. The external part is comprised of both the tread and sidewall and, also, the inner lining, which ensures that the tire is always hermetically sealed. The sidewall is extremely flexible, due to the positioning of steel cords on top of each other (Schramm et al., 2014). This enhances the vehicle's stability and leads to a maximum contact with the road. It allows for a more comfortable ride and higher durability, and, in the case of heavy machinery, like tractors, for an operation at higher loads. Radial-ply tires have a better braking behaviour, especially when aquaplaning. At the same tire pressure, greater, transferable lateral forces are generated, while having a lower rolling resistance (Guiggiani, 2014).

2.2   The Suspension System

The suspension system has a clear and straightforward function: to connect a vehicle's body with the wheels, so it is possible to carry the body along the driving way and to transmit the contact forces. This way, the generation of accurate and reproductible wheel movements becomes feasible.

Another purpose of this system is to give the wheel the potential to follow a vertically aligned movement, along the horizontal motion given through the drivetrain. This creates the opportunity for a wheel to travel through paths with uneven surfaces. Additionally, the use of spring and damping elements

results in the reduction of body movement, which helps achieving a great amount of driving comfort and a safe driving behaviour (Schramm et al., 2014).

The front suspension of a vehicle helps transmit the steering movements to the wheels, usually over a special connecting rod, known as tie rod or, in some cases, steering knuckle. These rods are usually mounted on rubbery-elastic manufactured bearings, which play a major role in accomplishing a good driving behaviour and high comfort (Reimpell et al., 2001). Besides, the suspension system's geometry and spring and damping influence the position of the wheel relative to the road, so that there happens to exist a systematic impact on the dynamic driving characteristics of the vehicle. Lastly, the suspension system plays an active role in guiding the forces and torques, created during the wheel/road contact, onto the vehicle's body (Guiggiani, 2014).

Nowadays, there is a great variety of suspension systems, which can be used in a wide range of applications. However, all of them share the three basic components: joints, dampers, and springs. These components, working together, can set up a basic suspension system.

Springs, depicted as the red component in Figure 2.3, actuate by storing energy, in a compression state, that is released when they return to the normal state. There are different types of springs to be used, although the coil type is the most common and found in most vehicles. They are compact, easily assembled, and are extremely long-lasting.

Figure 2.3 - Example of a spring-damper actuator. Adapted from (What is a damper, 2019).

Dampers, also illustrated in Figure 2.3, on the other hand, moderate the spring's oscillations and vibrations, returning the wheel to its initial vertical position after a load cycle. Usually, dampers use a piston/cylinder system, with control valves to determine and apply a damping force. To dampen oscillations, the damper dissipates energy to stabilize any components, such as springs.

A modern vehicle's suspension system must satisfy several conflicting requirements, due to the different conditions in which a vehicle operates, such as follows (Schramm et al., 2014):

- Load or without load

- Acceleration or braking

- Flat or uneven road

- Driving in a straight line or cornering

The suspensions' requirements can be divided into two categories to create a comfortable driving, and to achieve the best handling and driving safety. To achieve driving comfort, a suspension must (Schramm et al., 2014):

- Oppose the oscillations promoted on the wheel by the unevenness of the road

- Be compliant and flexible to reduce the rolling stiffness of the tire and the motions created by small longitudinal blows, due to the tire's contact with the surface

- Not upset the development of lateral forces and therefore the turning precision

As for optimal handling characteristics:

- Establish the suspension's geometry and kinematics makes to prevent diving or lifting during braking or acceleration, assuring the non-existence of oversteer

While the previous requirements give a general guideline to design a suspension system, one must divide suspensions into three general categories:

- **Rigid Axles (dependent)**: two wheels are connected rigidly to an axle, that controls both wheels at the same time.

- **Independent Suspension**: each wheel is allowed to move vertically, without the influence from the other wheel on the same axle

- **Semi-rigid axle**: Combines some characteristics from both previous types

2.2.1 Rigid Axles

This type of suspension, illustrated in Figure 2.4, is the oldest of the three and is also known as beam-axle. It can be found in some commercial vehicles, as a power-driven rear axle (rear axle with drive shaft). Even if it is not ideal for modern standards, it can be used, rarely, as a front axle in all-terrain vehicles, since it provides good off-road characteristics (Reimpell et al., 2001).
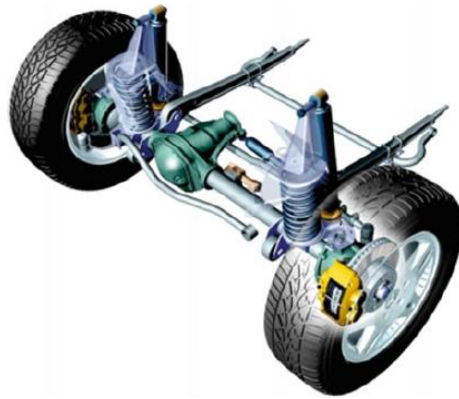
Figure 2.4 - Example of a rigid axle suspension system. Adapted from (Schramm et al., 2014).

A beam axle can be defined as a solid connection of two opposing wheels via a lateral axle. Those two wheels can influence each other. The axle is usually constructed of 4 bodies, connected by 6 spherical joints, making it a simple, but heavy structure to build (Schramm et al., 2014). The kinematic coupling of both sides of the car, through the solid connection of both wheels, arouses a large camber variation, which is not ideal.

2.2.2 Semi-rigid axle

Semi-rigid suspensions, also known as twisted-beam axles (represented in Figure 2.5), substitute the rigid connection between two wheels for a compliant and flexible link. The semi-rigid axle allows relative motion between both wheel carriers because of the torsion of the axle beam, to which are given elastic properties.
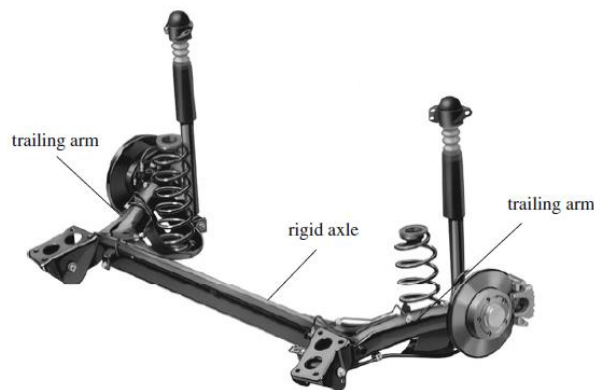
Figure 2.5 - Example of a semi-rigid axle suspension. Adapted from (Schramm et al., 2014).

In this case, both wheel carriers are attached to torsional stiff and deflection-resistant trailing arms, which are transversally connect via a profile with low torsional stiffness. Movement, force, and positional control are supplied to the wheels through the beam's elastic deformation (Reimpell et al., 2001). This type of suspension is composed of 4 bodies, usually connected by 1 revolute joint with torsion spring, 2

spherical joints, 1 prismatic joint and 1 cylindrical joint (Schramm et al., 2014). As for advantages of this design, one can list the following:

- Little need of mounting space
- Establishment of a stabilizing effect through a cross member
- Low weight
- Good roll compensation

Nevertheless, the semi-rigid axles are difficult to implement and have limited potential for optimizing the driving and steering dynamics.

2.2.3   Independent suspensions

Independent suspensions are the most found in modern cars, due to some benefits like the little amount of space needed to assemble the system, the low weight, the better turning capabilities, and, especially, the non-influence between wheels on the same axle. Unlike the previous types, it is necessary to divide the independent suspensions into two categories: the ones with one rotation axis and the systems with more than one rotation axis. As can be seen Table 2.1, each different type branches itself into several different technologies of independent suspension systems.

Table 2.1 - The different types of independent suspension systems.

One rotation axis	Trailing Arm
	Semi-Trailing Arm
	Wishbone
More than one rotation axis	MacPherson Strut
	Double-Wishbone
	Multilink

Before talking specifically about the different types of independent suspension systems, it is important to mention one big downside of using this system. Since each wheel has its own independent system, the wheels will tilt with or against the body of the vehicle. With this, when travelling along a curve, the exterior wheels will absorb most lateral forces, attaining a positive camber angle. The interior wheels will then possess a negative camber angle, which reduces the tire's lateral grip (Schramm et al., 2014). Albeit, these effects are, in fact, avoidable. For this, the kinematic camber's changes need to be considered, being adjusted as the car rolls, and the body roll, in a curve, must be kept as small as possible

(lateral forces generate a torque that reinforces a vehicle's body roll while travelling). These effects are obtained by using stiffer springs, or anti-roll bars, or even by transferring the body roll centre to a higher location in the vehicle (Schramm et al., 2014).

The trailing-arm axles, portrayed in Figure 2.6, are a type of independent suspension with a single joint between the wheel carrier and the body. Each wheel has its own trailing arm, which, in turn, absorbs the longitudinal and lateral forces created on the contact between wheel and road. This allows a swing motion of the wheel around a sole rotational axis, which is perpendicular to the longitudinal axis of the vehicle.
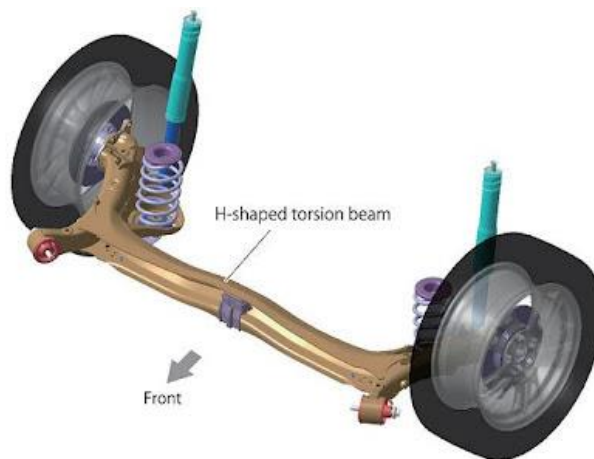
Figure 2.6 - Representation of a rear axle trailing arm suspension. Adapted from (Rear Axle Trailing Arm Suspension, 2012).

The single link is rigidly connected to the wheel carrier and to the chassis via a revolute joint. Furthermore, the links can be elastically mounted to the body, so that they move longitudinally, for improved performance and comfort (Schramm et al., 2014). This system requires little to no space, as it is easily constructed and assemble onto the body. Unilateral suspension allows for variables like track width, toe-in and camber angles to be kept constant. Its small size and compactness promoted the almost non-existence of unsprang masses (Reimpell et al., 2001). Despite the number of advantages brough by this system, it has a design restriction for axle kinematics and has no roll compensation, as it keeps the centre of rotation low. It creates a strong rolling tendency.

The double-wishbone suspensions, represented in Figure 2.7, are commonly found in modern vehicles, especially as the rear-axle in passenger cars, albeit they can be mounted at the front. These are characterized by having two transverse links, known as control arms or wishbones, in each side of the vehicle, which are mounted to rotate.
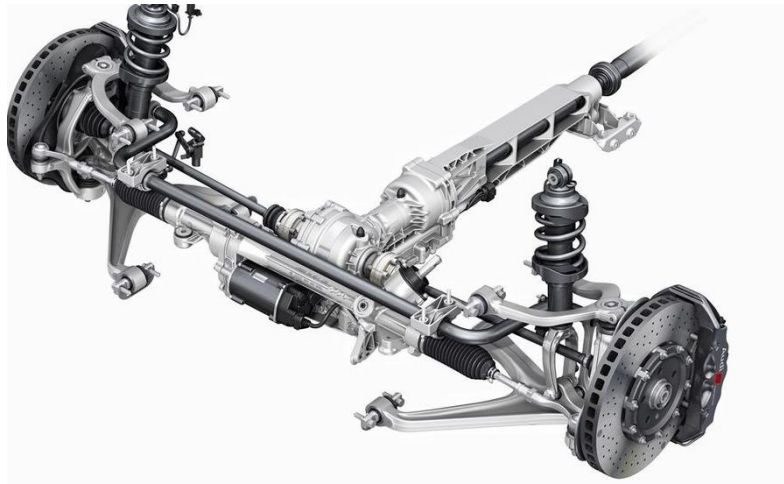
Figure 2.7 - Representation of a double-wishbone suspension system. Adapted from (Robinson, 2018).

One wishbone is located above the centre of wheel and the other one can be found below it. The bigger the distance between links, the smaller the reaction forces on both suspension's arms, which leads to less deformation and therefore a more precise control of the wheels (Schramm et al., 2014). If mounted as the front axle, it is needed to connect both rods to the steering rod, or tie rod, which prohibits or defines the steering. The tie rod is attached to the double links via spherical joints, and it undertakes the transmission of the steering forces towards the wheel carrier (Schramm et al., 2014).

The position of one wishbone in relation to the other ends up determining the body roll centre's height and pitch pole. Different wishbone's lengths can have an influence on the wheel's angular motions, either in compression or in rebound. With a smaller upper wishbone, wheels being compressed acquire a negative camber, while rebounding wheels stay with a positive angle. This, in fact, cancels (opposes) the camber's sudden change, prompted by the vehicle's body roll, increasing comfort, and driving stability. The position of the body roll centre is particularly important, since, if it is not located at the wheel's centre, it produces an anti-dive (car's nose, or front, dive - Figure 2.8) mechanism and, also, reduces the squatting of pulled rear axles (Reimpell et al., 2001). As well as allowing a largely free designability for characteristics like the toe and camber angles and track width, the double-wishbone suspension is very well suited for powering. Still, it requires large spaces to fit in, due to its complex structure and hard elasto-kinematic setup.
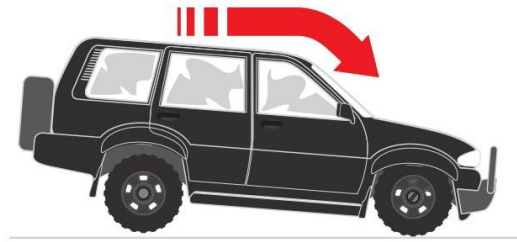
Figure 2.8 - Illustration of a car's nosedive.

Although the double-wishbone suspension can be easily found in modern vehicles, the MacPherson Suspension (outlined in Figure 2.9), or strut, is also commonly used in modern passenger vehicles.
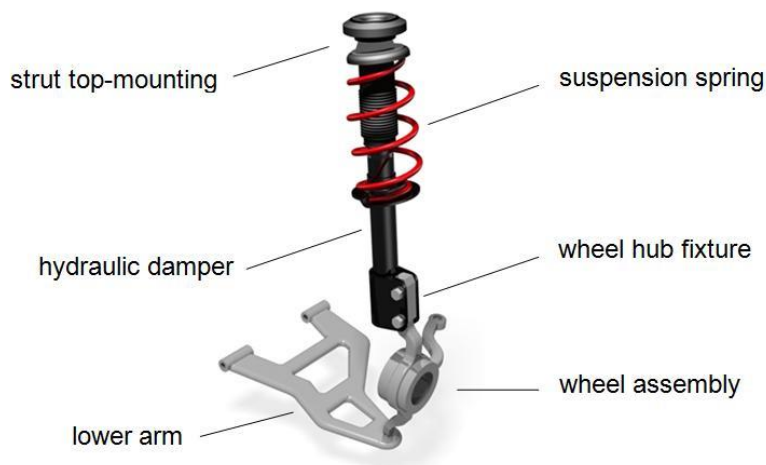
Figure 2.9 - Example of a Macpherson spring strut. Adapted from (Czop, 2011).

Comparatively with the double-wishbone suspensions, the MacPherson principle exchanges the top transverse wishbone for a shock absorber/spring combination (pivot point), known as strut, which connects to the wheel hub at the bottom, and, at the top, directly to the body. Still, the lower control arm is kept. A steering link also connects to the hub, where the strut is coming in (Schramm et al., 2014).

The MacPherson struts are divided into two designs:

- **Spring Struts**: the damper uses the clearance in the helical slip and at the same time supports both ends of the spring. The spring is mounted on the damper.
- **Damper Struts**: the spring is mounted separately from the damper

Despite the difference in struts, a standing damper is always tightly connected to the wheel carrier and the piston rod of the damper is mounted to the chassis. This leads to the creation of a cylindrical joint that enables both steering and spring displacement for the wheel carrier. There are also two rods: one functions as the steering rod, which is connected to the steering; and the other, works at the lower

tier, as a triangular wishbone, for the guidance of the wheel. Every single part of this assembly provides suspension and control. Schramm et al. (2014) state that MacPherson struts are usually comprised of 5 bodies, connected by 6 joints: 1 revolute joint, 2 prismatic joints and 4 spherical joints.

This design is usually cheaper, simpler, and lighter than a double-wishbone, having benefits in weight and cost savings. Since there is available space in the centre area of the suspension (in the wheel hub, between the wishbone and the strut), it allows space to install a driveshaft. This is especially great for front wheel drive vehicles. Finally, the strut is narrower than a double wishbone, which is perfect for fitting in tighter areas. Nonetheless, forces from all directions are concentrated at the pivot point, causing a bending torque in the piston rod, which impairs responding qualities (Schramm et al., 2014). The MacPherson strut is taller than a double wishbone, which can be bad in some cases. Also, there is no camber gain, which means that, while cornering, it will not promote a better contact with the road, as the body roll increases. This does not happen with the double-wishbone, which allows for a vertical movement of the tire.

The last type of independent suspension, with more than one rotation axis, is the multi-link suspension, represented in Figure 2.10.

Figure 2.10 - Example of a multi-link suspension system. Adapted from (Toyota's website, s.d.).

The multilink axles are usually made of 4 or more independent link. None of those links can be rigidly connected to the wheel carrier. This means that every rod needs to be fixed by virtue of a movable joint. The installation of a trapezoidal link leads to a fully integral link-suspension. The absorption of torques can be realized through a perpendicular additional link. This design, although expensive, provides a precise suspension, both laterally and longitudinally. The elasto-kinematics are also well adjustable.

2.3   Vehicle Kinematics

To fully understand the behaviour of road vehicles, it is of major importance to study their kinematics, which influence the behaviour of a vehicle during manoeuvres like cornering. In this chapter, a brief introduction to some concepts and definitions behind a car's kinematic response is provided.

A vehicle is usually free to rotate in three dimensions, as seen in Figure 2.11, and for that reason a car has three major motions: roll, pitch, and yaw. Each one of these represents a rotation around one of three axes:

- **Roll**: rotation around the longitudinal axis (x)
- **Pitch**: rotation around the lateral axis (y)
- **Yaw**: rotation around the vertical axis (z)
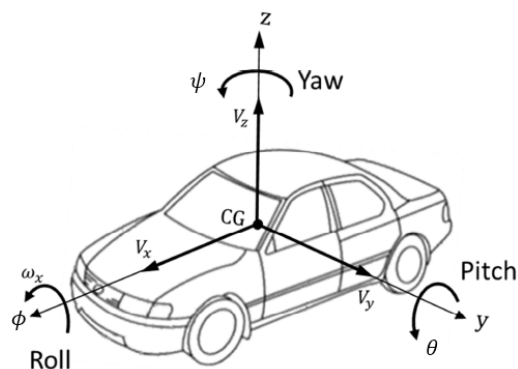
Figure 2.11 - Vehicle axis system, as represented in ISO 8855-2011. Adapted from (Kissai et al., 2019).

Each motion always exists in a car, although both roll and pitch can be neglected, since each amount is relatively small and most of the time are a result of the suspension's reactions. However, the yaw motion should not be neglected when studying car kinematics.

Schramm et al. (2014) define handling as the control of the path and speed of the vehicle. As is the norm, a car can turn, changing its path from a straight line to a curve. While making a turn, the motion of the wheels changes the direction in which the car is actively pointing at, and thus rotating the body around the vertical axis. The yaw plays a major role in vehicle kinematics, especially because it is seen at a macro level and has direct effects on the body's behaviour. Both roll and pitch are also seen at the macro level but are mere reactions to the state of the road, which is not studied by the kinematics. There are many ways to represent a car, either on a 2- or 3-dimension plane. Figure 2.12 shows a simple two-dimension plane representation, considering all four wheels.
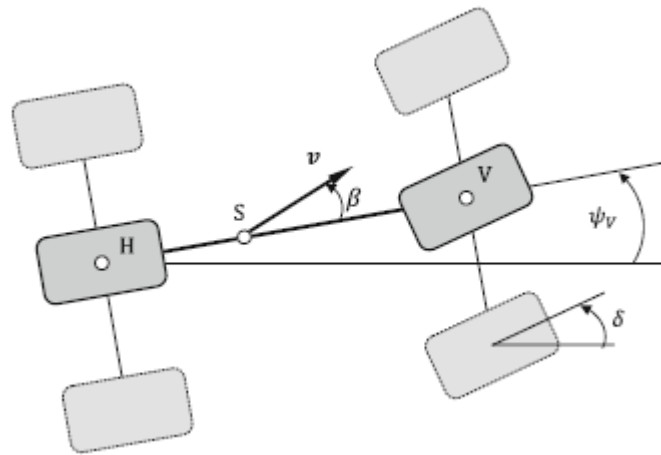
Figure 2.12 - 2-dimensional representation of vehicle. All wheels are highlighted but comprised into a bicycle model. Adapted from (Schramm, Hiller, & Bardini, 2014).

Figure 2.12 depicts several relevant variables. The forward velocity, v, is the component of the velocity vector in the longitudinal direction and can be assumed as constant. On the other hand, the lateral velocity is the velocity component in the lateral direction. The heading angle is the angle between the trace of the xy plane of the vehicle's x-axis and the x-axis of the global fixed reference system. When a car is turning, the heading angle is due to some changes over time, so that the vehicle can follow a desired direction. This angular variation leads to a concept known as yaw rate, which can be defined as the time rate of change of the heading angle (Schramm et al., 2014; Li, 2009).

Furthermore, it is possible to specify the action of making a turn on a vehicle. Making a turn can be divided into three different stages:

- Entry
- Steady State Cornering
- Exit

In the first stage, also known as transient turn entry, the yaw rate and the lateral velocity build up from zero to a new value. In the middle stage, the values of the yaw rate and lateral velocity are kept constant (alongside the slip angles of the tires, which will be studied in a later stage), and the vehicle is moving along a path with unvarying radius. Finally, in the turn exit, both yaw rate and lateral velocity start to change again, but this time returning to zero (Guiggiani, 2014).

To further understand the kinematics of a vehicle, it is necessary to study its equations of motion recurring to a dynamic model. There are several of them, but for the sake of simplicity, it will be used the Linear Single-Track model, or, as is commonly known, the Bicycle Model, depicted in Figure 2.13.
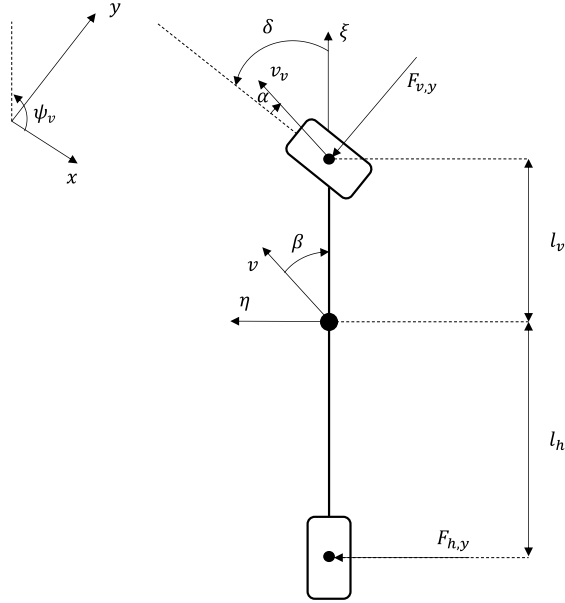
Figure 2.13 - Discretization of the bicycle model.

A car is composed of two pairs of wheels, one at the front and one at the rear. Within each pair, both wheels have almost the exact same behaviour, which is not true when comparing a rear and a front wheel. So, the bicycle model streamlines the representation of a 4-wheel car, by dividing it along the longitudinal axis. The result is a model that possesses only two wheels, one at the front and one at the rear. The front and rear tires are represented as a single tire on each axle. This massively helps the simplification of the number of variables, which, in turn, creates easier and less extensive equations. The equations are always the same, for any given author, but let us take (Schramm et al., 2014) as an example, and present the finals state space equations for the Bicycle model

$$\ddot{\psi}_v = \left[-\frac{1}{v} \frac{c_{\alpha,v} l_v^{\,2} + c_{\alpha,h} l_h^{\,2}}{\theta} - \frac{c_{\alpha,v} l_v + c_{\alpha,h} l_h}{\theta} \right] \dot{\psi}_v + \frac{c_{\alpha,v} l_v}{\theta} \delta \qquad (2.1)$$

$$\dot{\beta} = \left[-1 - \frac{1}{v^2} \frac{c_{\alpha,v} l_v + c_{\alpha,h} l_h}{m} - \frac{1}{v} \frac{c_{\alpha,v} + c_{\alpha,h}}{m} \right] \beta + \frac{1}{v} \frac{c_{\alpha,v} l_v}{m} \delta \qquad (2.2)$$

where β is the side slip angle and δ the steering angle, while ψ_v is the heading angle and $\dot{\psi}_v$ the yaw rate. All these variables are only defined for the front wheel because it is the only one with an ability to turn. $c_{\alpha,i}$ represent the lateral stiffness of the wheels. Schramm et al. (2014) and Guiggiani (2014) clearly show how to get to these final equations and, even, extend them to stationary steering behaviour and cornering. This model has some important considerations:

- The velocity of the vehicle's centre of gravity is considered as constant along the longitude of its trajectory

- The vehicle's mass is assumed to be concentrated at the centre of gravity

- The wheel-load distribution between front and rear axle is assumed to be constant

Although this is a possible model, there are other, such as the twin track model and the 7 DoF model. The former is thoroughly explained in (Guiggiani, 2014; Schramm et al., 2014), while the latter seen in (Zhou & Liu, 2010), where a stability control is designed.
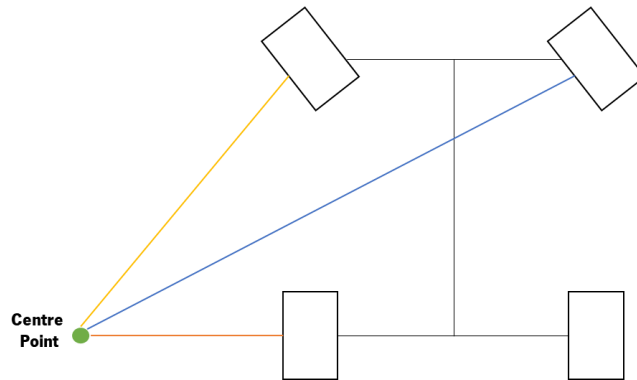
Figure 2.14 - Graphical representation of the Ackermann steering principle.

The final consideration about car kinematics has to do with the action of turning. As seen in Figure 2.13 and Figure 2.14, the tires are connected to a thread, that represents the way the tires turn around a corner, which is known as Ackermann Steering (Schramm et al., 2014).

The Ackermann Steering is a principle that was implemented to prevent the slipping of the tires, while they are turning (Guiggiani, 2014). It consists in an imaginary centre point, which all tires are rotating around to travel through a bend. Each tire is distinctly spaced from that centre point, meaning that all four tires will have a different radius to advance around. This, in turn, means that each tire is rotating at a different rate. The outside tires, for example the right-hand side on a left turn, will have more distance to travel, so they need to rotate more quickly than the inside tires (the left-hand side). Likewise, the front tires will always move faster that the rear tires, thus preventing the tires from slipping. Nevertheless, this can be problematic for 4 wheel-drive vehicles, as they would need the installation of several differentials, so it would be possible to split the speed of the front and rear tires (Schramm, Hiller, & Bardini, 2014).

3. TIRE-ROAD DYNAMICS

In this chapter the basis for this work will be introduced. To properly study a vehicle, it is necessary to know about its dynamics. The contact between vehicle and road is made by the wheels, which provide a platform for the generation and transmission of forces in all directions. These forces, known as contact forces, allow the car to move along a road. The study of these phenomena is of extreme relevance to this work and will be done in this chapter.

3.1   Background

The dynamics of vehicles will be of extreme importance to study and analyse the behaviour of a car going over obstacles. These dynamics can be evaluated by studying the interaction between the tires and the road. Apart from aerodynamics, which are not addressed in this work, the contact road-tire is the only interaction between the vehicle and the surrounding environment, which influences its motion. A vehicle is only able to traverse a said path because of the contact between road and tire. The friction between road and rubber is the main responsible of generating forces that will influence the tire locally, which, in turn, makes the motion of the vehicle possible (Schramm et al., 2014)

The contact road-tire actively influences the motion of a vehicle, such as a car, since it creates a patch, or point, where all forces and torques will be transmitted. These forces come from all directions, be it the lateral forces generated during cornering, or the tangential longitudinal ones created during transmission of acceleration or braking torques. This means that the forces need to be studied in all three spatial directions. Each force generates a torque that will actively influence the tire (Schramm et al., 2014).

Across several years, experts in this area studied this phenomenon and in (Schramm, Hiller, & Bardini, 2014) is presented a comprehensive and general explanation for it. The same work will be used as a reference to all formula and calculations needed to study the contact tire-road. Several other works analyse this thematic, such as (Guiggiani, 2014; Rill & Castro, 2020; Blundell & Harty, 2004; Pacejka, 2002). The formulation discussed in the next section presents a general formulation for the contact between tire and road. Not all authors use the same methods to model this contact. Pacejka (2002) introduces this topic and presents several models. Also, sources such as (Canudas-de-Wit et al., 2002; Rill G. , 2019) explain other ways of formulating this problem.

3.2 Tire Dynamics

As stated before, all forces and torques originated due to the contact between tire and road are transmitted on a patch, called the contact patch, represented in Figure 3.1. This singular definition is probably the most important to understand the dynamic being studied.

Figure 3.1 - Graphical representation of the tire contact patch. Adapted from (Contact Patch, s.d.).

The transmission of force between a tire and a road takes place on a contact patch. This patch is nothing more than the area on the tire's surface that is in contact with the road. It was seen in chapter 2.2 that a modern tire is made of several radial layers, the outer layer being known as the tread. In practice, the only layer in contact with the road is the exterior one, the tread.

Being this an elastic layer, the vertical loads generated will induce a deformation, known as tire deflection, on the tread. Theoretically, this deflection flattens the surface of the tread as demonstrated in Figure 3.1, which, in fact, is just a physical manifestation of the contact patch.

The forces between the road and the tire are described as contact forces and are represented in Figure 3.2. The primary contact force is the normal reaction with the road, the vertical force, F_Z. Nevertheless, the contact force can be decomposed into three components, one acting in each direction. Both longitudinal, F_x, and lateral forces, F_y, are described as functions of the kinematic properties of the contact patch, also known as slip, s and slip angle, α. The decomposition of the forces is possible by splitting the current velocity of the wheel centre into lateral and longitudinal components. These components are associated through the slip angle.
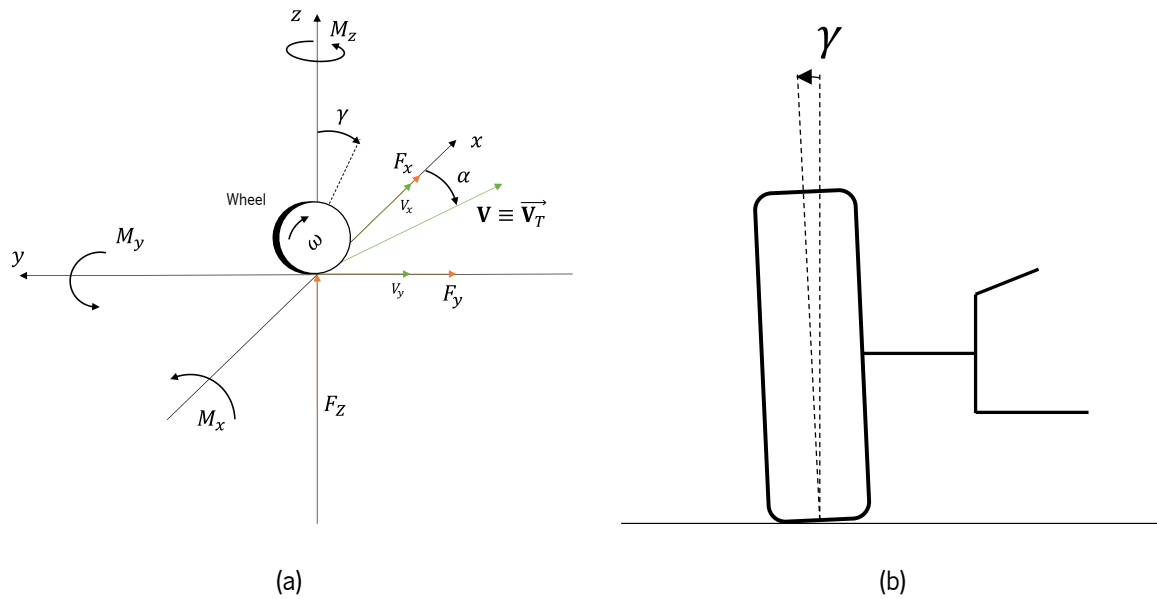
Figure 3.2 – (a) Three-dimensional discretization of the tire/road dynamics; (b) Representation of the camber angle.

The vertical direction, z, must be associated with a unidirectional force transmission mechanism, since only compressive forces will be transmitted (Schramm et al., 2014). The longitudinal and lateral forces are parallel to the road, in other words, tangential. These are transmitted by friction mechanism, which makes dependent on the friction material pairing between tire and road.

3.2.1   Vertical Loads

A tire possesses stiffness in the radial direction. Thus, the tire is commonly represented as a spring in the radial direction (Schramm et al., 2014), as depicted in Figure 3.3.
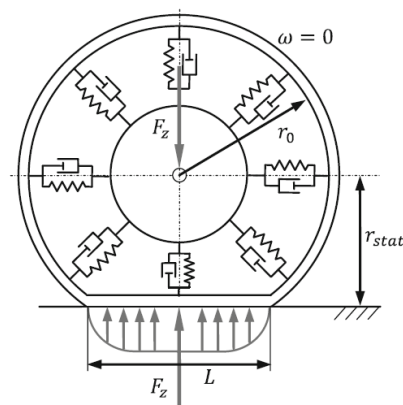
Figure 3.3 - Vertical force acting on the contact patch. Adapted from (Schramm et al., 2014).

The vertical load, F_Z, creates the so-called contact patch at the contact region with the road surface, generating a deformation, known as tire deflection.

$$\delta_z = r_0 - r_{stat} \tag{3.1}$$

This means that the vertical load induces a deflection on the construction tire radius, r_0, causing a compressing deformation. In a static position, the surface pressure will be symmetrically distributed across the length of the contact patch, given by (Schramm, Hiller, & Bardini, 2014)

$$L \approx \sqrt{2r_0\delta_z} \tag{3.2}$$

This equation gives an estimation of the length of the contact patch, although does not possess an extreme precision. This value is usually calculated through experimentation and testing on a real test rig. The wheel load, or vertical force, depends primarily on the tire deflection. In (Schramm, Hiller, & Bardini, 2014), this force is given by a nonlinear spring as

$$F_z = \begin{cases} c_z\delta_z + c_{z,3}\delta_z{}^3 \text{ if } \delta_z > 0 \\ 0 \text{ if } \delta_z \leq 0 \end{cases} \tag{3.3}$$

A vertical load equal to zero represents the lifting of the wheel off the ground, which can occur and, hence, should always be considered in any computation. The previous formulation is just an example of how to calculate the normal load acting on a wheel, while stationary (a rolling wheel, however, utilizes the same formulation). Many others have been designed (e.g., (Pacejka, 2002; Rill & Castro, 2020)) but all of them state that the vertical load is a function of the deflection and the tire's radial stiffness. Some formulations, such as Rill's, (Rill & Castro, 2020; Rill G. , 2019), consider two different members: a static, present in Eq. (3.3), dependent on the stiffness, and a dynamic, that is created by the tire's damping (which is dependent on the wheel's deformation velocity, thus only used for rolling wheels). Figure 3.3 shows that a tire includes stiffness and damping, much like several spring-damper actuators. However, the damping of a normal tire is usually extremely low, especially when compared with the suspension's damping. Thus, that value has almost no expression in the final value, and, hence, many authors, such as Pacejka (2002) or Rill (2020), consider unnecessary to add that contribution to the equation.

3.2.2 Rolling Resistance

In the previous subsection, it was considered that the wheel was in a static position. While it helped formulate some concepts, a vehicle's wheel must be studied when it is rolling. Thus, let us apply a rolling torque, with no acceleration, to the wheel, like that represented in Figure 3.4.
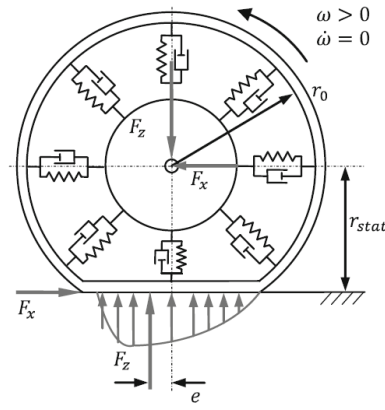
Figure 3.4 - The effect of the rolling resistance on the force application point. Adapted from (Schramm et al., 2014).

The rotation of the wheel over a surface changes the deflection over time. On a perfect surface, without any roughness, the deflection is mostly constant. Nonetheless, there are no perfect surfaces, so the rotation of the wheel will change the deformation continuously, while energy is being dissipated due to the viscoelastic properties of the carcass of the tire (Schramm et al., 2014).

It is known that a tire possesses damping and stiffness in the radial direction, represented by the dampers and springs in Figure 3.4. The dampers account for the damping provided by the tire's rubber, hence it is never a big damping. Nevertheless, the rolling will provoke an increase in normal pressure in the direction of rolling, which is velocity dependant, at the front part of the contact patch along the direction rolling. This increase is due to the generation of a longitudinal tangential force, F_x, at the contact patch, which is opposite to the direction of rolling. That said, there will also be a decrease in pressure at the rear side of the stated area. Across literature, it is said that the value of the vertical force does not change due to the rolling of the wheel. Also, the definition of the wheel's static radius will hold for dynamic cases. As seen, the surface pressure will be displaced to a forward position, which causes the point at which the normal load, F_z, is acting to be displaced in the direction of rolling. A torque balance must then be made. Let e be the displaced length (Schramm et al., 2014)

$$F_x r_{stat} - F_z e = \text{Constant} \tag{3.4}$$

The rolling resistance, which is a torque opposite to the rolling direction and gives the energy dissipation of a rolling wheel, is given by

$$M_y = F_x r_{stat} \tag{3.5}$$

3.2.3 Longitudinal Forces

Longitudinal forces are generated through accelerating or braking a vehicle. Both actions are directly associated with the tire. The first is transmitted by the driving shaft to the driven wheels and the second is directly applied to the wheel by the mechanical brakes. The transmission of longitudinal forces happens through friction, more specifically by adhesion, depicted in Figure 3.5, or hysteresis between the tire and the road. These concepts are nothing more than types of friction mechanisms.
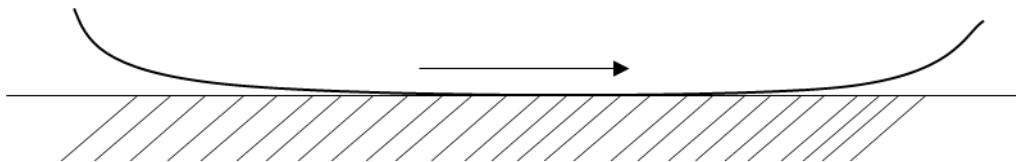
Figure 3.5 - Graphical representation of the adhesion friction mechanism.

Adhesion is created by intermolecular bonding forces between the rubber and the road's surface. For movement to happen, these chemical bonds need to be broken through shear forces. It is the dominant mechanism on dry asphalt roads, but it is significantly reduced on wet roads. This model usually represents smooth surfaces (Guiggiani, 2014).

Assuming the vertical force is the total force of contact, a ratio between it and the longitudinal force can be defined as

$$\mu = \frac{F_x}{F_Z} \tag{3.6}$$

The longitudinal forces are created due to the shear deformation of the tread in conjunction with the friction between the rubber and the road. This shear deformation is described by the longitudinal slip, or just slip. This variable represents the state of motion of a wheel, whether it is being driven, braked or non-driven. Let us define slip as s.
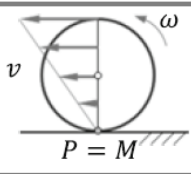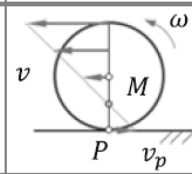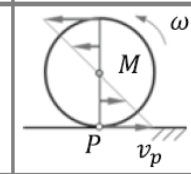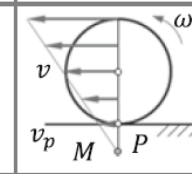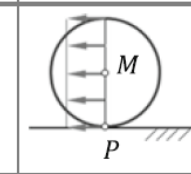
$v = \omega r$	$v < \omega r$		$v > \omega r$	
Rolling wheel	Driven wheel	Spinning wheel	Braked wheel	Blocked wheel
No slip	Drive slip		Brake slip	
$s_A = 0$ $s_B = 0$	$s_A = \dfrac{v_P}{\omega r} = \dfrac{\omega r - v}{\omega r}$	$s_A = 1$	$s_B = \dfrac{v_P}{v} = \dfrac{v - \omega r}{v}$	$s_B = 1$

Figure 3.6 - Types of motions derived from slip for a wheel. Adapted from (Schramm et al., 2014).

A wheel has two states of motion: pure rolling, when the velocity at the centre of the wheel, V, is equal to the rotational velocity, $\omega \times r$; rolling and sliding, when both velocities are different. As seen in Figure 3.6, a fictional contact point must be defined, P. Instead of representing the full contact patch, one can say that the contact forces are acting upon this singular point. The velocity of this point may be known as V_p, and it correlates the rotational velocity and the centre point velocity of a wheel. So, if a wheel is in a pure rolling state, then (Schramm, Hiller, & Bardini, 2014)

$$V_p = 0 \tag{3.7}$$

The slip is given as the relation between V_p and the larger of the two values, V and $\omega \times r$, and it is written as a relative value, given in the interval [0, 1] or in percentage. For a driven wheel, one knows that the angular velocity of the wheel will be bigger than the linear velocity, V. The acceleration longitudinal slip is then calculated by

$$s_A = \frac{V_p}{\omega r} = \frac{\omega r - V}{\omega r} \tag{3.8}$$

An extreme case for this value would be if $s_A = 1$. This means that

$$\omega r \neq 0 \text{ and } V = 0 \tag{3.9}$$

Eq. (3.9) physically means that the wheel would be spinning while staying at the same place.

A braking slip means that a braking torque is acting on the wheel, and so the angular velocity decreases more than the actual linear velocity. In this case

$$S_B = \frac{V_p}{V} = \frac{V - \omega r}{V} \tag{3.10}$$

If $S_B = 1$, the wheel will be blocked, which means it would be moving linearly without any rotation. Although a variable r was used to calculate the rotational velocity of the wheel, it has not been explained what it in fact means. This variable on a normal situation would be the nominal radius of the tire, r_0. Due to the tire deflection, it rotates around with a smaller radius than the construction one. This is known as dynamic radius (Schramm et al., 2014; Guiggiani, 2014), given by

$$r_{dyn} = \frac{2}{3}r_0 + \frac{1}{3}r_s \tag{3.11}$$

The rotational velocity would now become ωr_{dyn}, instead of ωr.

To formalize the surge of tangential forces, on driving or braking situations, a model has been created. The Brush model depicted in Figure 3.7 indicates that the tread of a tire is represented through elastic beam elements, known as profile elements, that will suffer shear or sliding motions. This model helps to understand the behaviour of a tire under longitudinal forces, since its own friction with the road changes from purely adhesion to only sliding, if some conditions are met (Schramm et al., 2014). The Brush

model is the basis for all tire dynamics and, especially, for the tire force models that will be discussed later.
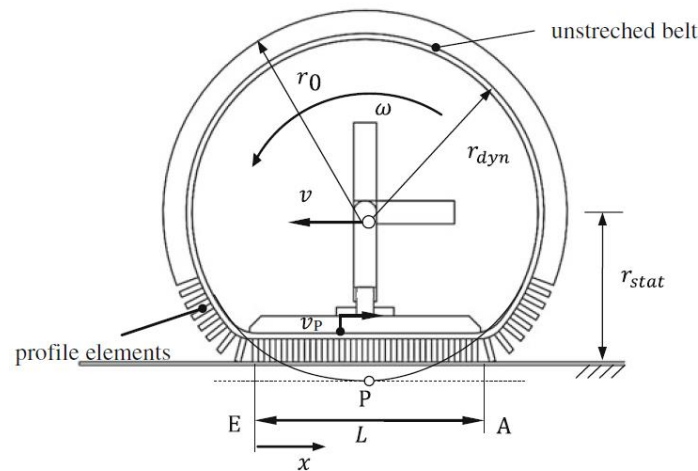
Figure 3.7 - Representation of the tire brush model as in (Schramm et al., 2014).

A profile element enters the contact point at E and exits it at A, like in Figure 3.8, with a velocity equal to ωr_{dyn}. Again, V_p represents the velocity of the contact patch. If there is no slip, then the patch is said to be at rest, meaning no shear or sliding motions will be applied on the elements. For a driven wheel, the profile elements will be sheared towards the front, while if a wheel is being braked, the profile elements will be sheared to the back. Looking at Figure 3.8, it is possible to state that at the entry point, the profile will be totally adhered to the surface (remember the wheel is travelling to the left, so the contact patch will evolve from the left to the right with the rotation of the wheel). The horizontal deformation of the element is given by $\hat{u}(t)$ or $u(x)$, if $x = \omega r_{dyn} t$. As the element moves along the patch, there will be an increase in deformation in the direction of E and the maximum deformation will happen at the exit point, u_{max} (Schramm et al., 2014).
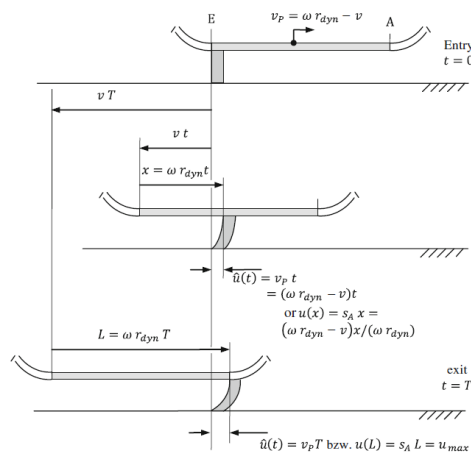
Figure 3.8 - Behaviour of a profile element at the contact patch by (Schramm, Hiller, & Bardini, 2014).

Assuming a profile element is in adhesion across the total length, the shear stress on each element is (Schramm et al., 2014)

$$\tau_x(x) = ku(x) \tag{3.12}$$

The constant, k, depends on some tread characteristics, such as the height and the shear modulus of the rubber. With the shear stress is possible to compute the longitudinal force transferred by all the profile elements over the contact surface, C, with a breadth of b (Schramm et al., 2014)

$$F_x = \int \tau_x(x)d(C) = \int_0^L \tau_x(x)bdx = \frac{1}{2}kbL^2s \tag{3.13}$$

The vertical force can also be calculated using the brush model. Assuming a Coulomb friction for the adhesion between the profile elements and the road surface, and a constant pressure distribution over the patch (Schramm, Hiller, & Bardini, 2014)

$$F_Z = \int p_z(x)d(C) = \int_0^L p_z(x)bdx \tag{3.14}$$

If the tangential stress surpasses the adhesion boundary at any given point, the profile elements will begin to slide. The adhesion condition is given by (Schramm et al., 2014)

$$\tau_x(x) \leq \tau_{xH}(x) \text{ with } \tau_{xH}(x) = \mu_H p_Z(x) \tag{3.15}$$

The sliding condition yields

$$\tau_{xG}(x) = \mu_G p_Z(x) \tag{3.16}$$

The adhesion friction coefficient must always be bigger than the sliding friction coefficient. A rule of thumb is

$$\mu_G < \mu_H \rightarrow \tau_{xG}(x) < \tau_{xH}(x) \tag{3.17}$$

The contact area, outlined in Figure 3.9, can then be divided into two different regions: the adhesion region and the sliding region. Being G the adhesion boundary (EG – Adhesion zone; GA – Sliding zone), it is possible to conclude that as the slip increases, so does the sliding area. The tire would then lose its adherence with the road and start sliding across it, which causes the wheel to either block or spin (Schramm et al., 2014; Guiggiani, 2014). The longitudinal force can only be described in relation with the longitudinal slip, s. This results in a curve dependent on the tire's behaviour.
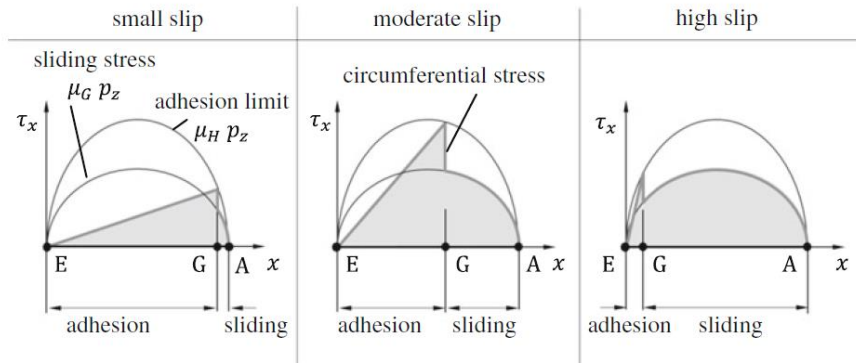
Figure 3.9 - Division of the contact length in terms of adhesion and sliding areas. Adapted from (Schramm et al., 2014).

Figure 3.10 is a typical representation of a force-slip curve for the longitudinal force. For small slip values, below s_{max}, the adhesion region extends over the entire contact patch length. In this region, the longitudinal force, F_x, increases linearly and is proportional to the triangular surface under the tangential stress distribution (left case in Figure 3.9). In fact, that distribution is only valid for adhesion scenarios over the entire patch. The longitudinal force is of the type (Schramm et al., 2014)

$$F_x = c_s s$$ (3.18)

where c_s is the longitudinal stiffness of the tire.
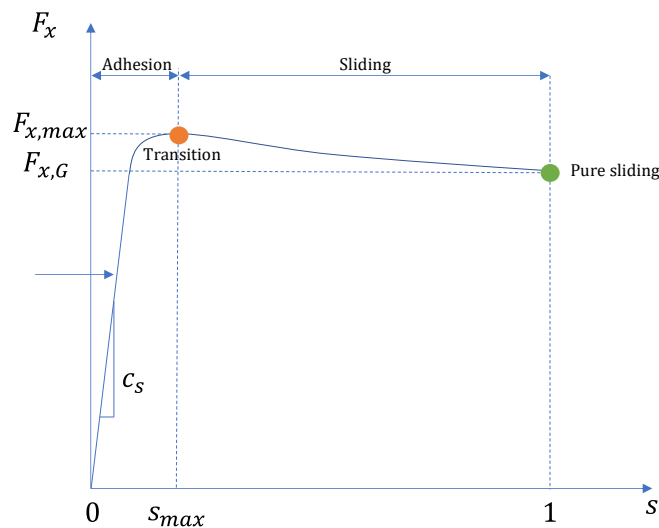
Figure 3.10 - Typical longitudinal force-slip curve.

If the slip increases further past s_{max} value, the sliding region starts to increase disproportionately (Figure 3.9 – middle). The longitudinal force between the road and the tire reaches the maximum possible, where the coefficient of friction is given by

$$\mu_{max} = \frac{F_{x,max}}{F_Z} \tag{3.19}$$

It must be said that the maximum value of the adhesion friction in the patch can be achieved only in the transition zone between adhesion and sliding regions. For very high slip values, the longitudinal force starts to decrease, with the increase of slip, until it reaches a final value, $F_{x,G}$, during pure sliding. At this point the wheel is either blocked (during braking) or just spinning (during acceleration). The sliding friction coefficient corresponds to

$$\mu_G = \frac{F_{x,G}}{F_Z} \tag{3.20}$$

Considering no lateral forces are being transmitted (this is just a case where only longitudinal forces exist), the curve represented in Figure 3.10 is influenced by:

- Constructive Parameters: Increasing the longitudinal stiffness of the tread dislocates s_{max} towards smaller values of slip.

- Vertical Load, F_Z: Only the longitudinal force changes, the maximum value of slip remains the same. Increasing the vertical load leads to bigger longitudinal stiffness and therefore a bigger initial slope. The linear zone enlarges, while the friction coefficient stays the same.

- The limits of the longitudinal forces increase proportionally with the vertical load up to a "statistical point". From there the increase starts to be degressive, due to deformation of the tire structure.

- μ_{max} and μ_G: if these values are modified, a stretch on the ordinates and abscissas with respect to the origin is generated. The initial slope remains the same because it is only affected by the shear stiffness. The maximum value of the longitudinal force will move for bigger values of slip. The combination of increment in both vertical load (increases the slope) and maximum adhesion coefficient moves the transition point to greater slip values. This produces a later entrance into the sliding zone. For dry surfaces and bigger values of vertical load, the maximum longitudinal force, which also increases, is due to higher values of slip, s, as seen in Figure 3.11.

33
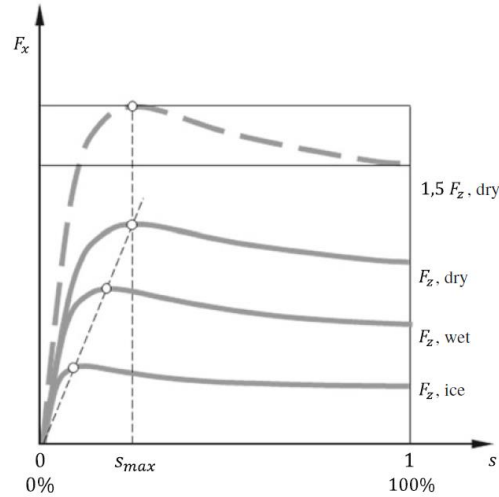
Figure 3.11 - Changes to curve with variable vertical load. Adapted from (Schramm et al., 2014).

3.2.4 Lateral Forces

To study lateral forces, no longitudinal forces will be considered. A rolling wheel that is subject to a lateral force, F_y, generates a velocity component lateral to the rolling direction (Schramm et al., 2014). Lateral forces are generated primarily during cornering when the slip angle, sketched in Figure 3.12 is different from zero.
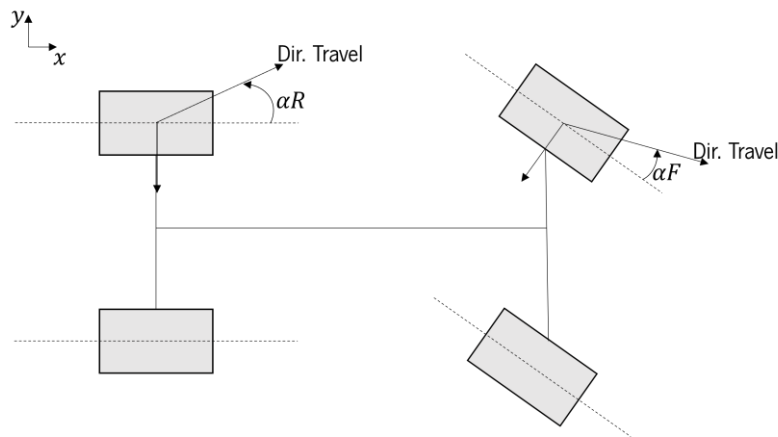
Figure 3.12 - Graphical representation of the slip angle.

The lateral slip, or slip angle, is simply calculated as

$$\alpha = \text{atan}\left(\frac{V_y}{V_x}\right)$$

(3.21)

One can assume that the tread exhibits similar deformation characteristics in the longitudinal and lateral directions, so it is also possible to use the brush model to investigate the lateral case. Let us consider that a profile element adheres to the surface of the road. This beam element will be deformed

laterally until it reaches the exit point of the patch, as represented in Figure 3.13. It is known that for small slip angles, the element adheres from one the patch's end to the other. Here the lateral tangential stress will increase linearly. The lateral force will be given by (Schramm, Hiller, & Bardini, 2014)

$$F_y = \int \tau_y(x)d(A) = c_\alpha \sin(\alpha)\cos(\alpha) \qquad (3.22)$$

c_α is nothing more than the cornering stiffness of the tire.
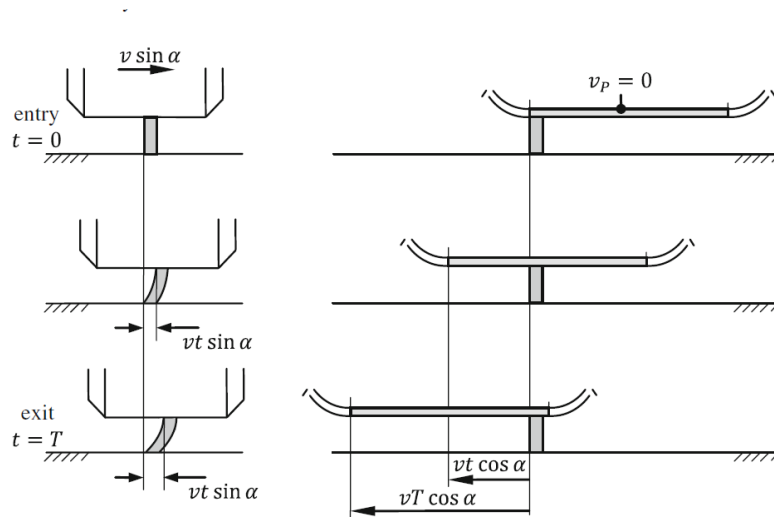
Figure 3.13 - Brush model for the lateral side of the tire. Adapted from (Schramm, Hiller, & Bardini, 2014).

Much like for the longitudinal force, a curve relating the lateral force with the slip angle can be created as seen in Figure 3.14. The lateral force increases proportionally with the slip angle. At larger angles, the deflection of the patch elements and the tangential stress will increase towards the posterior patch boundary. The adhesion friction limit will be exceeded, and the sliding will begin. In the adhesion region, the force increases linearly. In the sliding region, the lateral force will no longer increase linearly, but will do it so digressively with respect to the slip angle. With an increasing slip angle, the sliding region will move towards the front of the patch, till it encompasses the entire surface, at maximum slip angle (Schramm et al., 2014).
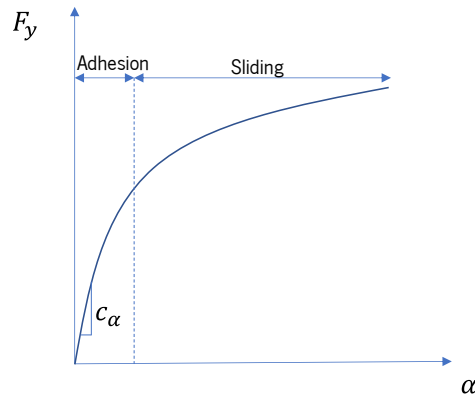
Figure 3.14 - Typical lateral force-slip angle curve.

The increase in lateral stress in the direction of the patch exit will cause the resultant lateral force to act slightly behind the middle of the patch as in Figure 3.15. This creates a torque that tries to reduce the slip, called the self-aligning torque. It opposes the slip angle in such a way that it is trying to return it to zero. It is given by

$$M_z = n_R F_y \tag{3.23}$$

n_R describes the tire caster angle (see the Glossary).
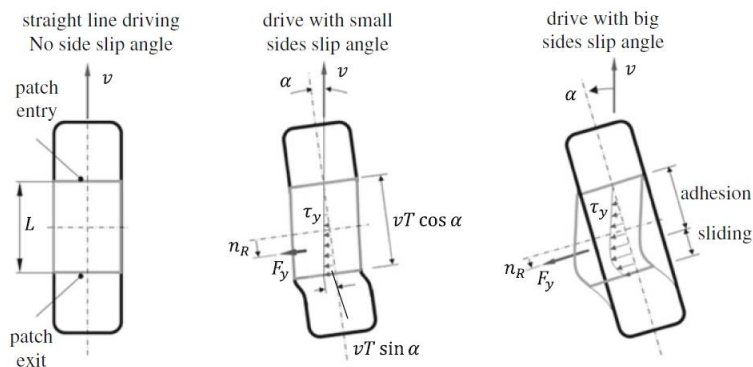
Figure 3.15 - Changes in the contact patch due to the slip angle and lateral tangential stress. Adapted from (Schramm et al., 2014).

3.2.5   The slip angle and Influence of Tire Load on the Patch Surface

The slip angle is the angle between the rolling velocity and the speed of travel of the tire. In other words, it is the angle formed between the direction of motion of the tire centre point and the longitudinal direction of the wheel (Guiggiani, 2014), much like the one represented in Figure 3.16.
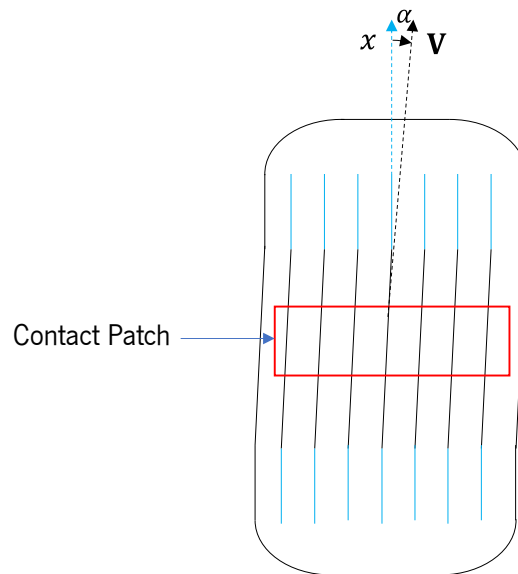
Figure 3.16 - Representation of the contact patch deformation and its relationship with the slip angle.

When the wheel is cornering, the friction between the tire and the road creates a lateral force that acts upon the tire, thus generating a deformation, amplified by the viscoelastic properties of the rubber. The wheel is then deformed in the direction the wheel is heading, like in Figure 3.16. The slip angle of a vehicle may not be the same for every wheel. Each pair of wheels (front or back) will have the same slip angle, but rear tires might have a different slip angle than the front tires. These events lead to different situations:

- Understeer: α Front $> \alpha$ Rear
- Oversteer: α Front $< \alpha$ Rear
- Neutral Steering: α Front $= \alpha$ Rear

In normal working conditions, both longitudinal and lateral forces have a linear relationship with the normal load, F_Z. However, if the vertical load increases and surpasses the constructive operating load (that one the tire was built for), the friction in the contact decreases with the increase of the contact force and, consequently, the longitudinal force increases degressively with respect to the tire load.

3.2.6   Superposition of Longitudinal and Lateral Forces

Pure longitudinal forces or pure lateral forces are hardly found. The former only happen if the car is following a purely straight line, while the latter only occurs during a steady state cornering, with constant velocity. Although these situations can happen, in real driving situations both forces are overlapped. Most of the time, longitudinal forces and lateral forces are transmitted at the same time. According to Coulomb's friction law (Schramm et al., 2014)

$$\sqrt{{F_x}^2 + {F_y}^2} \leq \mu_{max} F_z \hspace{4cm} (3.24)$$

which represents the rule that must be followed by any tire: the sum of lateral and longitudinal forces cannot be higher than the maximum amount of friction force due to the vertical load. It arises a new concept: the friction circle.

Figure 3.17 represents the friction circle, in which the inner circle is known as sliding region, while the outer circle is called adhesion region. In normal working conditions, a tire should work inside the outer circle. This concept creates some limitations to the forces. The maximum lateral force, when a simultaneous longitudinal force occurs, is reduced, it needs to follow the rule of Eq. (3.24). For real driving situations, accelerations or braking torques, that increase in modulus the longitudinal force, reduce the maximal possible lateral forces generated on a bend. The opposite is also true.
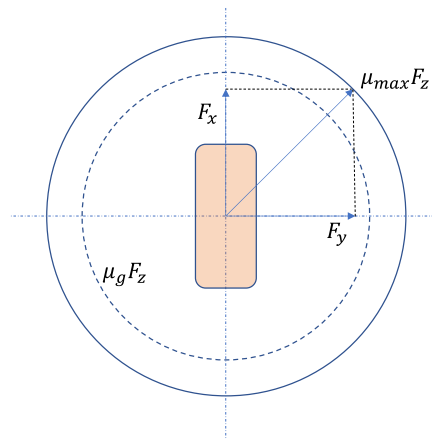
Figure 3.17 - Graphical representation of the friction circle for the contact forces.

Although the usual representation of this concept uses a circle, another theoretical hypothesis is being used nowadays. The limit of the transmissible tangential forces is, in fact, an ellipse, where the adhesion limit in the longitudinal direction is larger than in the lateral direction. This means that the slip-force curves for acceleration and braking will not be symmetrical.

3.2.7 The Deformation of the Tire

One of the main purposes of a tire is to reduce vibrations caused by the road, which makes its elastic and damping properties extremely valuable. For an effective damping, big vertical deformations are required, although it causes worse handling. Handling is also dependent on horizontal deformation, which is provided by softer tires (Schramm et al., 2014).

The vertical flexibility of the carcass gives the dynamic behaviour and is the main source of rolling resistance. Longitudinally, the minimum deflection of the exterior rubber bands determines the

characteristics of the longitudinal force-slip conditions. In the lateral direction, the same characteristics are provided by the exterior bands and the deflection on the carcass.

3.3 Tire Force Models

3.3.1 Background

The contact between road and tire has been a highly debated theme ever since vehicle dynamics started to be studied. In fact, the contact dynamics play a very important role in the design of both tires and vehicles. There are several ways to study these dynamics, known as tire models.

These so-called tire models represent forces and torques that are generated on a tire during the contact with the road. Tire models are particularly helpful to either design tires or to fully understand the behaviour of a vehicle on the road. Every tire model is different, in that it represents the same physical phenomena in a different manner, leading to results with different precision. There are two types of models, i.e., the mathematical and the physical. It is possible to consider a third type, which is the combination of both mathematical and physical models.

Mathematical models represent physical characteristics of tires through purely mathematical description (Schramm et al., 2014). Being totally made from mathematical functions, these are not the most precise and correct models, since they cannot truly characterize a tire's behaviour over time, especially in the non-linear regions.

Nevertheless, it is not theoretically possible to get perfect results for these occurrences, like longitudinal forces or rolling resistances, from the get-go with purely mathematical models. Thus, it can be necessary to derive these mathematical models into what is called the Semi-Empirical Models. Before generating functions of the behaviour of a tire, some of its parameters are empirically measured in different conditions, usually on a test rig. After the measurements are made, the results are stored as mathematical curves. It is important to note that the measurements do not need to be extremely extensive, as posterior processing can be done by interpolation using the mathematical functions that represent the curves. Mathematical, and semi-empirical models are usually the simplest and easiest to use, despite needing a great quantity of parameters to generate precise curves. As a matter of fact, changing individual parameters begets a change in curves, since each represents a single assessed variable.

The mathematical models are usually represented in quasi-static states, meaning that a tire is considered as a single unit with mass and inertia. The different layers that compose a tire are not dealt

with. The Physical Models can be of three types: finite elements, stationary models, and transient models. These models are adequate for some important effects happening on a tire, such as heating or inflation pressure. Also, they can present a visual representation of the tire and simulate transient conditions, important for a more accurate representation of the tire (Schramm et al., 2014).

3.3.2   Dugoff Model

One of the first purely mathematical models to be introduced into the automotive industry was the Dugoff Model (Dugoff et al., 1969), that can compute both longitudinal and lateral forces under pure or combined slip conditions.

This model is characterized by its simplicity and low computation time, only requiring a couple of mathematical functions to work. However, it cannot describe the dynamic characteristics of tire forces. Nevertheless, it can be especially useful when a high degree of complexity is not needed (Dugoff et al., 1969). The Dugoff Model is made of a set of equations, one for the longitudinal force and the other for the lateral dynamics (Dugoff et al., 1969)

$$F_x = c_s \frac{s}{1+s} \cdot f(\lambda) \tag{3.25}$$

$$F_y = c_\propto \frac{\tan(\propto)}{1+s} \cdot f(\lambda) \tag{3.26}$$

These equations a non-linear relationship between the slip quantities, the directional stiffness, and a function of the Dugoff factor, λ. This factor combines the values of the vertical load, the stiffnesses and the slip quantities, and, finally, the maximum friction coefficient into one value (Dugoff et al., 1969)

$$\lambda = \frac{\mu_{max} F_Z (1+s)}{2\sqrt{(c_s s)^2 + (c_\propto \tan(\propto))^2}} \tag{3.27}$$

$$f(\lambda) = \begin{cases} (2-\lambda) \; if \; \lambda < 1 \\ 1 \qquad\quad if \; \lambda \geq 1 \end{cases} \tag{3.28}$$
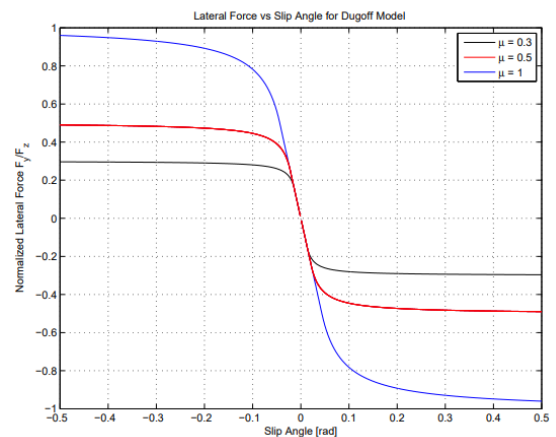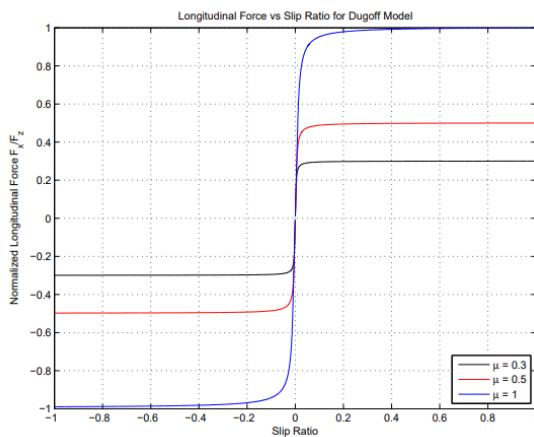
Figure 3.*18* (left) shows the variation of the longitudinal force with the slip ratio. The Dugoff model can clearly represent the initial linear change of the force (Bhoraskar & Sakthivel, 2017). However, instead of reaching a maximum value (the value that separates the region of adhesion from the sliding one) and then entering a non-linear state of decay, the longitudinal force keeps increasing its value with the increment of the slip ratio. But this is a bad representation of reality. The linear state of change of the longitudinal force, represented by an almost-fully linear increase, ends at a maximum value. After that, the longitudinal force starts to decrease non-linearly, reaching a final value, when the slip ratio equals one, lower than the peak value. The same happens for the lateral force. The Dugoff Model does not possess the ability to showcase these dynamics (Bian, 2014; Bhoraskar & Sakthivel, 2017).
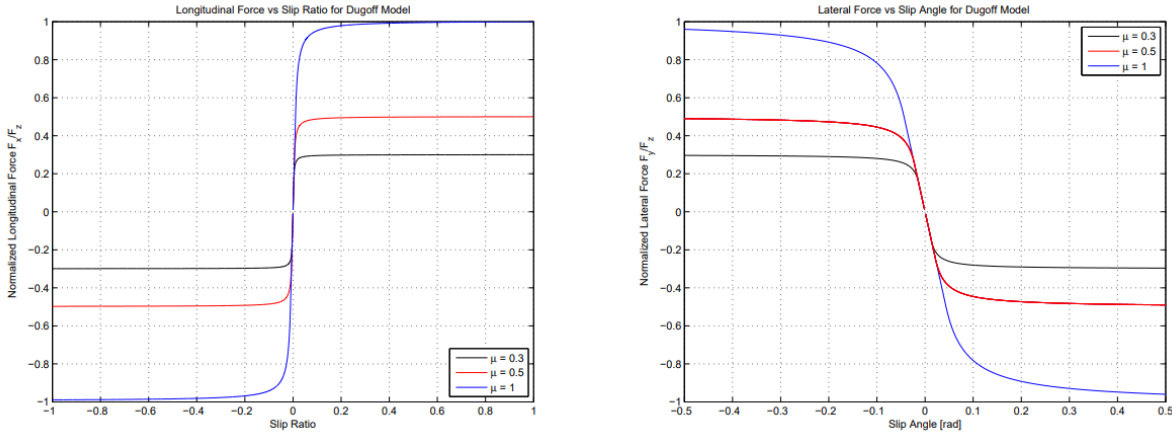
Figure 3.18 – Longitudinal and lateral forces using the Dugoff model. From (Shekhar, 2017).

Furthermore, the Dugoff model is fit for expressing the change trend of friction forces. Nonetheless, its precision decreases for large slip ratios or slip angles. Also, it does not reflect the truth about the friction coefficient decreasing when the value of the slip ratio is large (Bian, 2014).

3.3.3 Modified Dugoff

Although being an easy model to implement, the Dugoff model lacks some of the precision and quality when compared with other models, such as the Magic Formula, especially when calculating forces for larger values of slip. The Dugoff Model shows a continuously increasing trend with the increment of the slip ratio, or the slip angle, and its curves have no peak point. It does not reflect some principles. Therefore, a solution was created, in order to create a more robust Dugoff model and is presented at (Bian, 2014).

Overall, a magnifying factor, G_s or G_α, is multiplied into the original tire forces equations, so that the decrease in force with the increment of slip/slip angle in the nonlinear region could be respected (Bian,

2014). This simple factor adds a peak point to the curves, which represents the dynamic characteristics that were missing in the original model. This model is represented as (Bian, 2014)

$$F_x = c_s \frac{s}{1+s} f(\lambda) G_s \tag{3.29}$$

$$G_s = (1.15 - 0.75\mu_{max})s^2 - (1,63 - 075\mu_{max})s + 1.27 \tag{3.30}$$

These equations represent the longitudinal force and the respective magnifying factor, G_s. For the lateral dynamics, the exact same thing happens (Bian, 2014)

$$F_y = c_\propto \frac{\tan(\propto)}{1+s} f(\lambda) G_\propto \tag{3.31}$$

$$G_\alpha = (\mu_{max} - 1.6) \tan(\propto) + 1.155 \tag{3.32}$$

Finally, it must be said that λ and $f(\lambda)$ are given by Eqs. (3.27; 3.28), respectively.

This model becomes closer to the MF model and has a peak point near the one obtained from the MF as seen in Figure 3.19. Nevertheless, the values obtained are consistent for the linear region, but the peak is reached later than expected and the nonlinear region showcases values that are larger than those expected. Still, the dynamic behaviour is not fully compromised (only by the slightly larger values after the peak). This model continues the premise of being simple, easy to implement and resolve, requiring less computation time than more complex models.
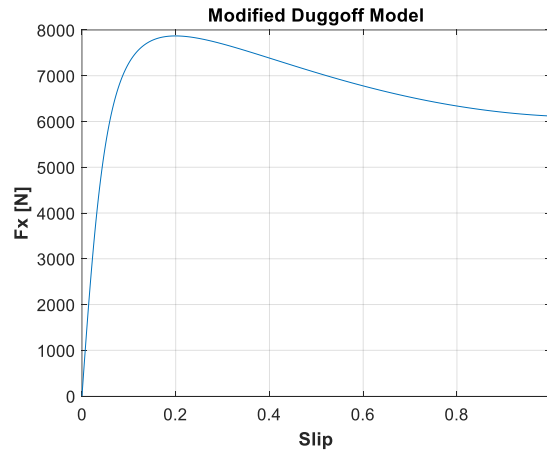
Figure 3.19 - Longitudinal Force computed with the Modified Dugoff model as function of the slip for a vertical load of 8kN.

3.3.4   Magic Formula

The Magic Formula is probably the most important tire model and was developed in the mid 1980's as a partnership between Delft University of Technology and Volvo. This model was presented in (Bakker et al., 1987; Bakker et al., 1989), and has suffered some evolutions found in (Pacejka, 2002)

The Magic Formula is a mathematical model, with a physical viewpoint (semi-empirical model) (Schramm et al., 2014). It describes the contact between tire and road trough mathematical formulae in quasi-static conditions (Pacejka, 2002). Unlike the Dugoff and Modified Dugoff models (Bhoraskar & Sakthivel, 2017), it requires the experimental measurement of some model parameters to build the mathematical curves that represent characteristics like the lateral and longitudinal forces (Pacejka, 2002). The measurements are stored as parameters that make up a mathematical function, known as Magic Formula. The tests are made in specific conditions with a vehicle cruising at a constant speed. This disables, from the get-go, the ability to predict the change of friction and the lag of the generation of frictional forces. It must be said that in reality these forces do not instantaneously reach a steady-state, but rather they exhibit a transient behaviour (Uil, 2007).

The relationships between forces and torques, and slip quantities, like the slip ratio and the slip angle, are determined in a quasi-static state of rolling or during handling situations, like cornering. This opens the possibility to represent those relations as curves of trigonometric functions, like the sine or the arctangent. Thus, the Magic Formula can describe force and torque variations at the contact patch as a function of pure or combined slip with high precision. The formula has a generic form that can describe each characteristic, only needing to change some of its parameters. However, as time went on, Pacejka developed new and more robust formulae, directly from the general statement, that can depict more detailed occurrences (Pacejka, 2002).

The general form of the Magic Formula is given by (Pacejka, 2002)

$$y(x) = D\sin(C\arctan{(Bx - E(Bx - \arctan{(Bx)}))}) \tag{3.33}$$

Table 3.1, presents the meaning of each variable represented in Eq. (3.33). These "big" parameters are built by several other parameters, that must be obtained experimentally, like stiffness coefficients or the friction between tire and the road.

Table 3.1 - Meaning of each parameter of the general Magic Formula.

Parameter	Meaning
B	Stiffness factor
C	Shape factor
D	Peak value of the curve
E	Curvature factor
BCD	Slope at the origin
S_H	Horizontal shift
S_V	Vertical shift

x	Variable (slip or slip angle)

The general function can describe several characteristics from the steady-state behaviour with high fidelity and precision. It facilitates a physical interpretation and evaluation of the different relations, while maintaining an easy access to important data. Also, the Magic Formula, unlike the Dugoff Model, can capture a tire's non-linear behaviour, in extreme slip conditions.

The general Magic Formula always gives a curve that passes through the origin, depicted in Figure 3.20, representing either the longitudinal force, the lateral force, or the different torques, as functions of the slip quantities, with the vertical load and camber angle included as parameters (Pacejka, 2002).
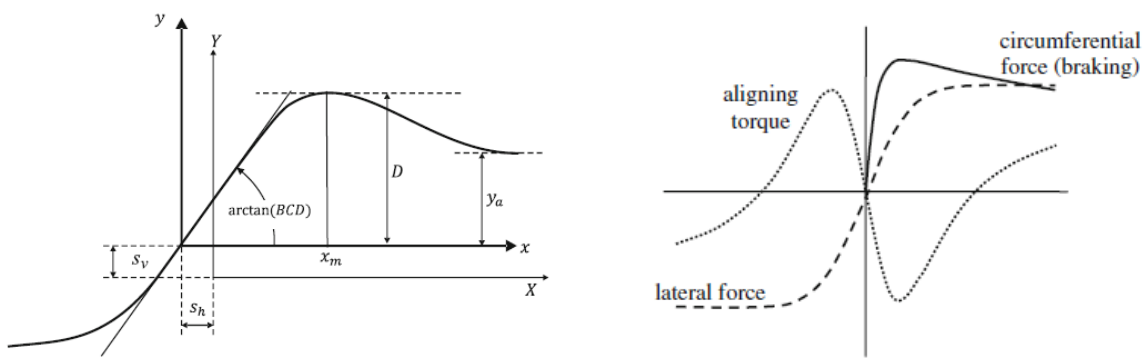
Figure 3.20 - General curves given by the Magic Formula. Adapted from (Schramm, Hiller, & Bardini, 2014) and (Pacejka, 2002).

Therefore, the general function, given by Eq. (3.33), always creates a curve that passes through the origin. This means that, when the slip, or slip angle, are equal to zero, there are no forces being created between the tire and the road. Well, sometimes this is not entirely true. Some of the tire's construction principles, such as ply-steer (pseudo-side slip) and conicity (pseudo-camber) effects, may cause the forces not to pass through the origin (these relate to a non-symmetrical construction of the tire). This implies the creation of a new function, where two different shifts may be added (Pacejka, 2002)

$$Y(X) = y(x) + S_V \tag{3.34}$$

$$x = X + S_H \tag{3.35}$$

Sometimes, the original function is not sharp enough, which gives rise to a new term. For extreme cases, one might use (Pacejka, 2002)

$$y = D \sin(C \arctan[Bx - E(Bx - \arctan(Bx) + H \arctan(Bx)^7]) \tag{3.36}$$

Lastly, the parameters, presented in Table 3.1, are calculated through the experimentally measured parameters. These can range from friction coefficients to damping and stiffness of the tire and are always

measured experimentally on a test rig at constant speed (steady-state), for a specific tire. Further into this work, these parameters will be discussed. A procedure to estimate them is presented in (A. Ortiz, 2006).

3.3.5   Physical Stationary Model: HSRI

The Highway Safety Research Institute (HSRI) developed its own model, which was directly derived from the Dugoff Model. It is presented extensively in (Schramm et al., 2014), and has been extended in (Uffelmann, 1980) for variable tire load and in (Wiegner, 1974), where the aligning torque was introduced.

This stationary physical model requires, as a first step, the equations of motion of the contact patch to be determined relative to the camber angle and the composite velocity (angular and translational) of the wheel centre point. This, then, allows the calculation of important variables, such as the slip angle and the longitudinal slip (Schramm et al., 2014).

With both the slip angle and longitudinal slip, the HSRI model is able to determine the dynamic tire forces. The longitudinal and lateral forces are evaluated by approximating the deformations taking place in the contact patch into a simple geometrical problem.

The deformations can be represented as a geometrical form, as provided by Figure 3.21, which encapsules two different regions: the adhesion region, at the front end of the contact patch, and the sliding region at the back end, created when the adhesion limit is reached. Both regions, although different in shape, can be depicted by a singular geometrical form, a trapezoid.
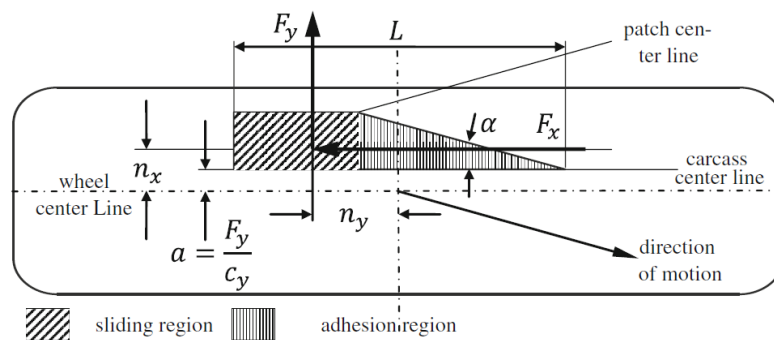
Figure 3.21 - Geometrical representation of the HSRI model at the contact patch. From (Schramm, Hiller, & Bardini, 2014).

The trapezoidal surface, representation of the contact patch, stems from the parallel shift of the tire's belt from the wheel centre line in the contact patch and through the partitioning into the sliding and adhesion regions (Schramm et al., 2014). The deflection of the tire gives way to the adhesion region, due to the slip angle, and to the sliding region, due to the parallel shift. If a constant pressure is assumed to

be over the entire patch, then the dynamic forces (longitudinal and lateral) can be considered as acting on the centre of gravity of the trapezoidal surface.

The first step to determine the equations of motion is to compute the sliding velocity, given by (Schramm et al., 2014)

$$V_G = V_P\sqrt{s^2 + \tan^2(\alpha)} \tag{3.37}$$

where V_P is the velocity at the contact point, as seen in section 3.2. Also, an adhesion coefficient can be calculated considering an adhesion factor, k_r, (Schramm et al., 2014)

$$\mu = \mu_0\left(1 - k_r\tanh\left(\frac{F_y}{C_\alpha}V_G\right)^2\right) \tag{3.38}$$

Much like the Dugoff model, a dimensionless value is used to know whether there is only adhesion at the contact patch or adhesion paired with sliding. Each case then presents a unique way to determine the dynamic tire forces. One presents that value as

$$S_R = \frac{\sqrt{(c_s s)^2 + (c_\alpha\tan(\alpha))^2}}{\mu F_Z(1 - s)} \tag{3.39}$$

If $S_R \leq 0.5$, then there is no sliding, but only adhesion in the contact patch. The dynamic forces are then given by (Schramm et al., 2014)

$$F_x = c_s s\left(\frac{1}{1 - s}\right) \tag{3.40}$$

$$F_y = c_\alpha\tan(\alpha) \tag{3.41}$$

If $S_R > 0.5$, sliding and adhesion are present in the contact patch. The dynamic forces must be computed as (Schramm et al., 2014)

$$F_x = \frac{c_s s(S_R - 0.25)}{S_R^2(1 - s)} \tag{3.42}$$

$$F_y = -\frac{c_\alpha\tan(\alpha)(S_R - 0.25)}{S_R^2(1 - s)} \tag{3.43}$$

3.3.6   Transient Models

The previous models are considered to be stationary models, hence they can simply describe steady-state manoeuvres, such as pure cornering or steady-state braking. In reality, during braking or turning, tire forces do not develop instantaneously, but require a certain rolling distance to be generated, due to the flexible structure of the tire (Guiggiani, 2014; Blundell & Harty, 2004; Schramm et al., 2014). This is usually called "lag" and can affect tremendously the performance of car, which is of particular interest for certain applications, such as security systems that control braking and slip (e.g., ABS). A transient

model is a physical model, usually complex, that tries to represent the previous characteristics, but especially the transient behaviour of friction forces.

The first of the transient models is known as SWIFT. This model was created as an extension to the Magic Formula. It uses the Magic Formula, while also using a rigid ring model that represents the tire. The tire belt is assumed to act like a rigid body, with inertia. (Pacejka, 2002; MF-TYRE & MF-SWIFT 6.1: USER MANUAL 2008, 2008). While the Magic Formula can be used for uneven roads, it only supports surfaces with low frequencies. The SWIFT model changes that and can simulate a tire rolling on highly uneven roads (up to 120 Hz).

This model, rendered in Figure 3.22, uses a single point contact to compute the slip, which is the same as the Magic Formula. The belt is a rigid ring connect flexibly to the rim, which possesses stiffness in all directions. The contact patch stiffness is modelled with a differential function with a time constant that corresponds to the adhesion area. The vibration modes of the tire are described by the sidewalls, which are elastically suspended rings. To simulate the tire moving over uneven roads, a three-dimensional obstacle enveloping model is used (Besselink, 2004; MF-TYRE & MF-SWIFT 6.1: USER MANUAL 2008, 2008; Schramm et al., 2014). Some work was also done to adapt this model to cope with variable inflation pressures, in (Schmeitz, Besselink, Hoogh, & Nijmeijer, 2005).
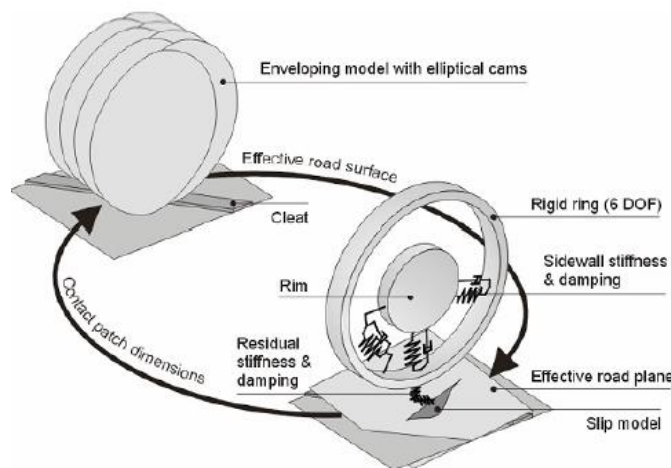
Figure 3.22 - Representation of the tire as in the SWIFT model. Adapted from (MF-TYRE & MF-SWIFT 6.1: USER MANUAL 2008, 2008).

A second transient model is the LuGre model (Canudas-de-Wit et al., 1995; Canudas-de-Wit et al., 2002), which derives from the Dahl friction model (Dahl, 1968). This model describes a dynamic force phenomenon created by two surfaces sliding on each other. The frictional surfaces are assumed to consist of bristles, which have motions described by differential equations (Uil, 2007; Tan et al., 2007). This model is somewhat friction based. Friction can be described by Coulomb or the viscous effect. However,

these models create a "static map" between velocity of the surfaces and the frictional force, which makes it impossible to describe Dahl effect (Dahl, 1968), the hysteretic behaviour for nonstationary vehicles.

The bristles, depicted in (Figure 3.23), represent the microscopic asperities of both surfaces and are said to be elastic. When a tangential force is applied to them, the bristles will deflect much like springs (Tan, Wang, & Zhang , 2007).
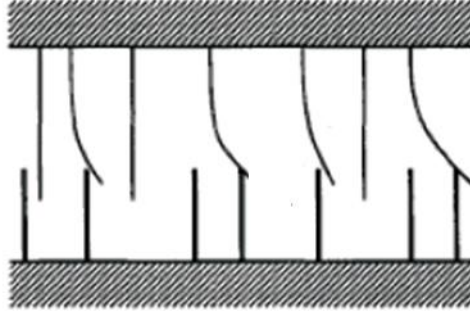
Figure 3.23 - The bristles between surfaces.

This deflection creates a friction force and, if it is too big, then some of bristles will slip. The average behaviour of those bristles paves the way to the LuGre dynamic model. This model assumes that the road-tire contact is realised through bristles attached to the belt, which are massless and elastic elements. In short, Canudas-de-Wit et al. (2002) represent the deflection of the bristles as

$$\frac{dz}{dt} = v_r - \frac{|v_r|}{g(v_r)} z \tag{3.44}$$

where v_r is the relative velocity between the two surfaces. The Stribeck curve is described by $g(v_r)$, which relates the relative velocity with the friction force as (Canudas-de-Wit et al., 2002)

$$g(v_r) = F_C + (F_S - F_C)e^{-(v_r/v_s)^\delta} \tag{3.45}$$

in which F_C represents the Coulomb friction force, while F_S is the striction force and v_s the Stribeck velocity. δ is the Stribeck exponent. The friction force from the deflection of the bristles can be written as

$$F = \sigma_0 z + \sigma_1 \frac{dz}{dt} + \sigma_2 v_r \tag{3.46}$$

where σ_0 is rubber longitudinal stiffness and σ_1 the damping. $\sigma_2 v_r$ is accounting for the viscous effect. The tangential forces can be obtained by multiplying the friction force with a normal force (Canudas-de-Wit et al., 2002; Tan et al., 2007)

$$F = \left(\sigma_0 z + \sigma_1 \frac{dz}{dt} + \sigma_2 v_r\right) F_z \tag{3.47}$$

It must be said that Tan et al. (2007) investigated a method to estimate this model's parameters, such as the friction coefficients.

4. MULTIBODY DYNAMICS

Any vehicle can be considered a multibody system. Thus, the vehicle can be studied as a multibody system, which creates the necessity of fully understanding the dynamics behind any multibody system. This chapter will serve as an introduction to the multibody dynamics analysis, which will integral to the definition and study of the vehicle.

4.1 Basic Concepts and Fundamentals

A multibody system can be described has a collection of mechanical components that describe rotational or translational motions. These components, which can be rigid or flexible, are connected via kinematic joints and, sometimes, force elements, such as spring-damper actuators. The joints impose restrictions on the relative movement of the bodies. The bodies can be of two different types:

- Rigid: The deformations do not affect the motion of the body. Its movement is described by 6 coordinates associated with 6 degrees of freedom. In most applications, the bodies are usually rigid.
- Flexible: These have an elastic structure, which 6 rigid degrees of freedom plus the number of generalized coordinates needed to describe the deformations.

Degrees of freedom (DoF) are the minimum number of generalized coordinates necessary to describe a system's configuration. A singular body can have 6 DoF in a 3-dimensional space: 3 translational plus 3 rotational around each axis, as seen in Figure 4.1.
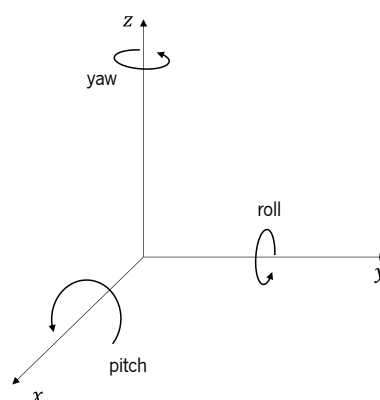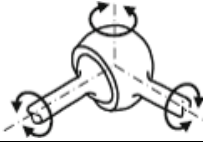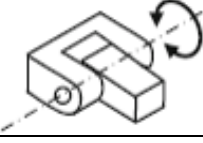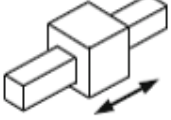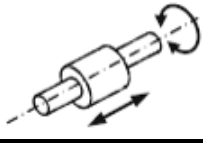
Figure 4.1 - Three-dimensional coordinate system.

If a kinematic joint were to be introduced, the number of DoF would necessarily decrease according to the number of restrictions imposed by the joint. DoF can be calculated as

$$n_{DoF} = 6n_b - m \tag{4.1}$$

where n_b represents the number of mobile bodies and m denotes the number of restrictions imposed by all joints. A multibody mechanism can have a multitude of DoF. If the number of DoF is positive, then that system is solvable. If it was zero, that system would not possess any motion. Lastly, if Eq. (4.1) returns a negative number, it means that the system is over-restricted. Each restriction creates restriction equations, which will be talked about later. Table 4.1 presents several types of kinematic joints used in this work and their characteristics.

Table 4.1 - Some kinematic joints and their characteristics (Flores P. , 2015).

Types of Joints		
Spherical		3 DoF: rotation around each axis 3 Constraints: translation of each axis (3 forces)
Revolute		1 DoF: rotation around one axis 5 Constraints: Translation of each axis (3 forces); rotation around the other 2 axles (2 torques)
Translational		1 DoF: translation of one axis 5 Constraints: 2 forces and 3 torques
Cylindrical		2 DoF: translation and rotation around one axis 4 Constraints: 2 forces and 2 torques

To solve a dynamic multibody system, it is necessary to generate its equations of motion that reveal, when solved, the behaviour of said system. The procedure should always start with the development of mathematical models that characterize the system. Afterwards, computational methods are used to simulate and analyse the motions of the system. Two types of formulations are used to represent a system: Point-coordinate, Joint-coordinate and Body-coordinate (Flores P. , 2015; Nikravesh P. E., 1988).

In the scope of this work, the body coordinates formulation is used. To obtain the equations of motion, a systematic approach is made to get equations based on the Newton-Euler equations (Flores P. , 2015; Marques et al., 2017). The bodies are represented by positions and velocities. This results in a big number of coordinates, which makes it inconvenient to solve by "hand". Nevertheless, the resultant equations are simple and versatile enough to be easily solved by computational methods.

Finally, the dynamics of a multibody mechanism can be analysed through two different approaches. In a forward dynamic analysis, the external forces acting on the bodies are always known, and the

resultant motions are obtained as a solution of the equations of motion. Conversely, in an inverse dynamic analysis, the motion of the body is already known, and the objective is to determine the necessary forces to produce that specific motion (Flores P. , 2015).

4.2   Global and Local Coordinates

To characterize the configuration and motion of a system, a coordinate system must be adopted. The global system of coordinates is represented as xyz. This is usually the reference frame, also known as absolute, from where all components will be defined. Additionally, a local system of coordinates, $\xi\eta\zeta$, is used to define local properties of points that belong to a body and has its origin on the centre of mass of a certain body. This system moves according to the motion of the body, its location and rotation being variable over time.

A body, i, moving in a 3-dimensional space, can be located by three independent variables, described by (Flores P. , 2015)

$$\mathbf{r}_i = \{x_i\ y_i\ z_i\}^T \tag{4.2}$$

A free rigid body, i, can be described by the definition of an arbitrary point located on the body and by the rotation of the body around that point. This creates endless ways of defining the spatial position of a body. The generalized coordinates (xyz), that describe the positions of all the elements of a multibody system, can be describe relative to themselves or a common referential. As Figure 4.2 suggests, vector $\mathbf{r}$ defines the location of the origin of the local reference frame, $\xi\eta\zeta$, in relation to the global frame, xyz. This vector represents the translational coordinates of the body. To fully represent the body, it is necessary another set of coordinates that express said body's orientation relative to the global frame (Flores P. , 2015).
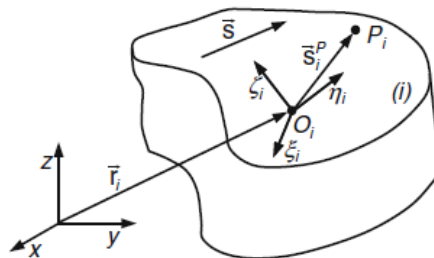
Figure 4.2 - Location of a body in a 3-dimensional space. Adapted from (Flores P. , 2015).

A point, P_i, located on body i, can be defined from the origin of the local frame of reference by a vector $\mathbf{s}_i^P$. Its direct location relative to the global frame is expressed as (Flores P. , 2015)

$$\mathbf{r}_i^P = \mathbf{r}_i + \mathbf{s}_i^P \tag{4.3}$$

The same point can be described by $\mathbf{s}_i'^P$ relative to the local coordinate system. This vector gives the location of the point in the local frame of reference, $\xi\eta\zeta$, written in local coordinates, which is constant for rigid bodies. To apply Eq. (4.3), this vector needs to be transformed from local to global coordinates with the following expression

$$\mathbf{s}_i^P = \mathbf{A}_i \mathbf{s}_i'^P \tag{4.4}$$

in which, $\mathbf{A}_i$ is the transformation matrix, which describes the orientation of the local coordinates frame relative to the global system. This is a 3x3 matrix, express in terms of cosines, that yields

$$\mathbf{A}_i = \begin{bmatrix} a_{11} & a_{12} & a_{13} \\ a_{21} & a_{22} & a_{23} \\ a_{31} & a_{32} & a_{34} \end{bmatrix} \tag{4.5}$$

Each column of the previous matrix represents a unit vector, projected onto xyz, that represent the local coordinate system, $\xi\eta\zeta$. So

$$\mathbf{u}_\xi = \begin{Bmatrix} a_{11} \\ a_{21} \\ a_{31} \end{Bmatrix}, \mathbf{u}_\eta = \begin{Bmatrix} a_{12} \\ a_{22} \\ a_{32} \end{Bmatrix}, \mathbf{u}_\zeta = \begin{Bmatrix} a_{13} \\ a_{23} \\ a_{33} \end{Bmatrix} \tag{4.6}$$

4.3   Rotational Coordinates and Angular Velocity

The orientation of a rigid body is defined by three rotational coordinates, which results in the previously presented transformation matrix, given by Eq. (4.6). The elements inside the matrix are expressed by several coordinates, namely the Bryant Angles, the Euler Angles or, even, the Euler Parameters. Also, as seen before, those nine elements are directional cosines that define the orientation of $\xi\eta\zeta$. Euler angles are three angles used to describe the orientation of a rigid body. Each represents a rotation that displaces a singular axis towards another axis of reference. Any rotation is obtainable by using three elementary rotations. Similarly, the Bryant angles are purely the xyz convention of the Euler angles (Flores P. , 2015). The two previous methods can represent the orientation of a system. However, this work will mainly focus on the Euler parameters, which will be presented next. To better understand Euler angles and Bryant angles refer to (Flores P. , 2015).

A problem that arises from the use of three different angles is the existence of singularities, that make the first and third rotation coincide (Flores P. , 2015). By using 4 rotational coordinates, this singularity is avoided. These are known as Euler parameters. Euler's theorem states that a rotation on a three-dimensional space can be always described by the rotation of a certain axis around a certain angle, as depicted by Figure 4.3.
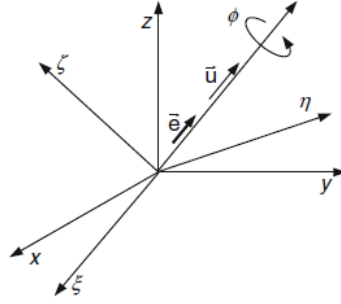
Figure 4.3 - Graphical representation of the Euler parameters. Adapted from (Flores P. , 2015).

The orientation of a fixed body's axes, at any given point in time, can be obtained through an imaginary rotation of those axes from an orientation coincident with the global axes (Flores P. , 2015). Therefore, there is only one axis, **u**, that makes xyz, through a rotation of an angle Φ, parallel to $\xi\eta\zeta$. This axis is called orientational axis of rotation. The rotational coordinates are given by (Flores P. , 2015; Nikravesh P. E., 1988)

$$e_0 = \cos\left(\frac{\Phi}{2}\right) \tag{4.7}$$

$$e = \{e_1\ e_2\ e_3\}^T = \mathbf{u}\sin\left(\frac{\Phi}{2}\right) \tag{4.8}$$

The previous variables e_0, e_1, e_2, e_3 are called the Euler parameters and in (Flores P. , 2015) is stated that

$$e_0^2 + e_1^2 + e_2^2 + e_3^2 = 1 \tag{4.9}$$

The Euler parameters are usually expressed as

$$\mathbf{p} = \begin{Bmatrix} e_0 \\ e_1 \\ e_2 \\ e_3 \end{Bmatrix} \tag{4.10}$$

The transformation matrix in terms of the Euler parameters can be written as

$$\mathbf{A} = 2\begin{bmatrix} e_0^2 + e_1^2 - \dfrac{1}{2} & e_1e_2 - e_0e_3 & e_1e_3 - e_0e_2 \\ e_1e_2 - e_0e_3 & e_0^2 + e_2^2 - \dfrac{1}{2} & e_2e_3 - e_0e_1 \\ e_1e_3 - e_0e_2 & e_2e_3 - e_0e_1 & e_0^2 + e_3^2 - \dfrac{1}{2} \end{bmatrix} \tag{4.11}$$

To know more about this topic, check the Appendix A.

Let us now imagine a body with only rotational motions. Its local coordinate system, $\xi\eta\zeta$, is rotating and its origin coincides with global system's origin as in Figure 4.4.
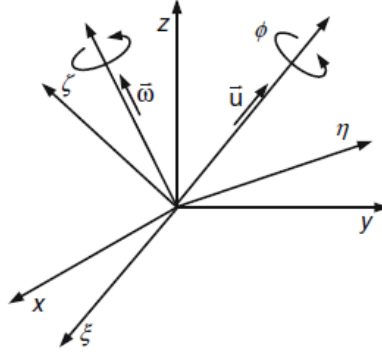
Figure 4.4 - Rotating $\xi\eta\zeta$ coordinate system.

A vector $\boldsymbol{\omega}$, known as angular velocity, describes the rotational axis and the rotation magnitude of the local frame. The angular velocity can be projected onto the local frame as $\boldsymbol{\omega}'$. (Flores P. , 2015) states that the transformation matrix and the angular velocity have the following relation

$$\dot{\mathbf{A}} = \tilde{\boldsymbol{\omega}}\mathbf{A} \tag{4.12}$$

The global position of a point, P, fixed in the local system is given by Eq. (4.4). Its derivative with respect to time is

$$\dot{\mathbf{s}}^P = \dot{\mathbf{A}}\mathbf{s}'^P \tag{4.13}$$

Applying Eq. (4.12) into Eq. (4.13) yields

$$\dot{\mathbf{s}}^P = \tilde{\boldsymbol{\omega}}\mathbf{A}\mathbf{s}'^P = \tilde{\boldsymbol{\omega}}\mathbf{s}^P \tag{4.14}$$

It is possible to obtain the velocity of any point, P, by finding the derivative of equation Eq. (4.3). The velocity of point P yields

$$\dot{\mathbf{r}}^P = \dot{\mathbf{r}} + \dot{\mathbf{s}}^P = \dot{\mathbf{r}} + \tilde{\boldsymbol{\omega}}\mathbf{s}^P \tag{4.15}$$

4.4   Equations of Motion for Constrained Multibody Systems

The dynamic response of a constrained multibody system can only be analysed by formulating the equations of motion that govern the behaviour of that system (Marques et al., 2017). The equations of motion of a system determine the acceleration of its components, so it is possible to calculate the positions and velocities in the next timestep trough an integration process.

As it has been seen, a constrained multibody system can be described by several generalized coordinates, which create a set of algebraic kinematic scleronomic constraints (Marques et al., 2017)

$$\boldsymbol{\Phi} \equiv \boldsymbol{\Phi}(\mathbf{q}) = 0 \tag{4.16}$$

Eq. (4.16) encompasses the set of holonomic and non-holonomic restrictions, where $\mathbf{q}$ is the position vector. With this, the velocity and acceleration of the components are evaluated by using the velocity and acceleration constraint equation, that read as follows (Flores P. , 2015; Marques et al., 2017)

$$\dot{\boldsymbol{\Phi}} \equiv \mathbf{D}\mathbf{v} = 0 \tag{4.17}$$

$$\ddot{\boldsymbol{\Phi}} \equiv \mathbf{D}\dot{\mathbf{v}} + \dot{\mathbf{D}}\mathbf{v} = 0 \tag{4.18}$$

It can be also said that

$$\mathbf{D}\dot{\mathbf{v}} = \boldsymbol{\gamma} \tag{4.19}$$

The Newton-Euler equations of motion for a multibody system of constrained bodies are, then, given by (Marques, Flores, & P. Souto, 2017)

$$\mathbf{M}\dot{\mathbf{v}} = \mathbf{g} + \mathbf{g}^{(c)} \tag{4.20}$$

where $\mathbf{g}^{(c)}$ is the vector of reaction forces, while $\mathbf{g}$ represents the vector of generalized forces. It is known that the Lagrangian multipliers are related to the joints' reaction forces (Flores P. , 2015). The vector of reaction forces can be expressed in terms of the constraints Jacobian matrix, $\mathbf{D}$, and the Lagrangian multipliers, $\boldsymbol{\lambda}$ (Flores P. , 2015)

$$\mathbf{M}\dot{\mathbf{v}} - \mathbf{D}^T\boldsymbol{\lambda} = \mathbf{g} \tag{4.21}$$

A unique solution is obtained when considering the constraint equations at acceleration level and the differential equations of motion together with a set of initial conditions (Flores P. , 2015)

$$\begin{bmatrix} \mathbf{M} & -\mathbf{D}^T \\ \mathbf{D} & 0 \end{bmatrix} \begin{Bmatrix} \dot{\mathbf{v}} \\ \boldsymbol{\lambda} \end{Bmatrix} = \begin{Bmatrix} \mathbf{g} \\ \boldsymbol{\gamma} \end{Bmatrix} \tag{4.22}$$

Eq. (4.22) poses a linear system of equations that can be solved using any suitable method. If solved analytically with respect to the accelerations vector, the dynamic equations of motion become

$$\dot{\mathbf{v}} = \mathbf{M}^{-1}(\mathbf{g} + \mathbf{D}^T\boldsymbol{\lambda}) \tag{4.23}$$

To solve Eq. (4.22), it is necessary to assume that inverse of the mass matrix, $\mathbf{M}$, exists. Also, a unique solution to the equation is guaranteed when the mass matrix is positive definite, and the Jacobian has maximum rank (Marques et al., 2017). By introducing Eq. (4.23) into Eq. (4.21)

$$\boldsymbol{\lambda} = [\mathbf{D}\mathbf{M}^{-1}\mathbf{D}^T]^{-1}(\boldsymbol{\gamma} - \mathbf{D}\mathbf{M}^{-1}\mathbf{g}) \tag{4.24}$$

Substituting Eq. (4.24) into Eq. (4.23)

$$\dot{\mathbf{v}} = \mathbf{M}^{-1}\mathbf{g} + \mathbf{M}^{-1}\mathbf{D}^T[\mathbf{D}\mathbf{M}^{-1}\mathbf{D}^T]^{-1}(\boldsymbol{\gamma} - \mathbf{D}\mathbf{M}^{-1}\mathbf{g}) \tag{4.25}$$

This last equation can be solved for $\dot{\mathbf{v}}$. The velocities and positions may be obtained through numerical integration, with the Lagrange multipliers method. This procedure must be done until the end of the analysis (Marques et al., 2017)

The equations of motion for constrained bodies can be solved using the algorithm presented in Figure 4.5, which represents the computation procedure for a kinematic multibody dynamics analysis (Flores P. , 2015)

- The initial positions and velocities are given, at $t = 0$.

- The mass matrix, $\mathbf{M}$, the Jacobian matrix, $\mathbf{D}$, and the constraint equations, $\mathbf{\Phi}$ are constructed. Also, vector $\mathbf{\gamma}$ and the generalized forces $\mathbf{g}$ are calculated

- Eq. (4.22) is solved relative to $\dot{\mathbf{v}}$ and the Lagrange multipliers, $\mathbf{\lambda}$, are also attained

- An auxiliary vector, $\dot{\mathbf{y}}_t$, for the generalized velocities and accelerations at $t = t$ is built

- The auxiliary vector is then integrated at $t + \Delta t$ to obtain the positions and velocities at that timestep

- If the final time is reached, then the analysis stops. If not, simulate for the new timestep until the end is reached
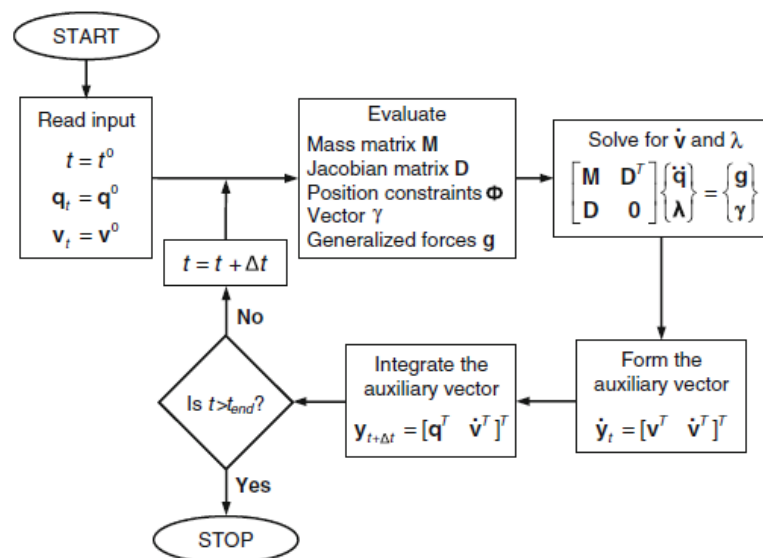
Figure 4.5 - Algorithm to solve the constrained equations of motion. Adapted from (Flores P. , 2015).

Although the standard Lagrange multipliers method may seem simple enough, one can find several numerical difficulties when using this method to solve the dynamic equations of motion (Marques et al., 2017):

- The mass matrix can be singular, instead of invertible, as is assumed most of the time. This happens when more than six coordinates are necessary to define the pose of a rigid body.

- A body, within the system, may present an extremely small inertia

- Redundant constraints may have been imposed on the system

- Changing topologies and units

Nevertheless, it is important to note that the system of the equations of motion does not use the position and velocity equations associated with the kinematics constraints (Marques et al., 2017). After the numerical solution of the system, both constraints at the position and velocity levels are not satisfied, so that the original constraint equations start to be violated due to the long integration process and inaccurate initial conditions. Thus, these errors in the position and velocity equations must be kept under control or, if possible, eliminated. This is possible through some methods, such as the Baumgarte Stabilization Method, the Coordinate Partitioning Method, the Penalty Methods and, finally, the Direct Correct Formulations, which have physical meaning. More about these methods can be found in (Marques et al., 2017).

Regarding this work, the formulation used to solve the equations of motion and to handle the constraints problem was the augmented Lagrangian method, which is an evolution of the penalty method (Marques et al., 2017). It was chosen because of the way it penalizes the constraints violations and handles singular configurations.

As for the penalty method, it can be stated that it is an alternative way to solve the dynamic equations of motion. These equations are modelled as a linear second-order differential equation, that reads as follows (Marques et al., 2017)

$$m_c\ddot{\mathbf{\Phi}} + d_c\dot{\mathbf{\Phi}} + k_c\mathbf{\Phi} = 0 \tag{4.26}$$

Introducing the acceleration constraint Eq. (4.18) into Eq. (4.26), yields

$$m_c(\mathbf{D}\dot{\mathbf{v}} + \dot{\mathbf{D}}\mathbf{v}) + d_c\dot{\mathbf{\Phi}} + k_c\mathbf{\Phi} = 0 \tag{4.27}$$

Pre-multiplying by the transpose of the Jacobian matrix, $\mathbf{D}$, results in

$$m_c\mathbf{D}^{\mathbf{T}}\mathbf{D}\dot{\mathbf{v}} = -\mathbf{D}^{\mathbf{T}}(m_c\mathrm{D}\dot{\mathbf{v}} + d_c\dot{\mathbf{\Phi}} + k_c\mathbf{\Phi}) \tag{4.28}$$

Now, considering the Newton-Euler equations of motion for an unconstrained system (Marques et al., 2017)

$$\mathbf{M}\dot{\mathbf{v}} = \mathbf{g} \tag{4.29}$$

And adding it to Eq. (4.28), one obtains

$$\mathbf{M}\dot{\mathbf{v}} + m_c\mathbf{D}^{\mathbf{T}}\mathbf{D}\dot{\mathbf{v}} = \mathbf{g} - \mathbf{D}^{\mathbf{T}}(-m_c\boldsymbol{\gamma} + d_c\dot{\mathbf{\Phi}} + k_c\mathbf{\Phi}) \tag{4.30}$$

where

$$\alpha = m_c; \ d_c = 2\mu\omega m_c; \ k_c = \omega^2 m_c \tag{4.31}$$

Typical values for α, ω, and μ are 10^7, 10 and 1, respectively (Marques et al., 2017).

Eq. (4.30) can be solved for $\dot{\mathbf{v}}$. With this method, multibody systems with redundant constraints or kinematic singular configurations can be solved. However, it cannot handle the problem of indeterminate Lagrange multipliers (Marques et al., 2017).

This work uses the augmented Lagrangian formulation, which penalizes the constraint violation much like the Baumgarte stabilization method. This ends up being an iterative procedure, involving the solution of a smaller set of equations, which can handle redundant constraints and singular configurations.

The evaluation of the systems' accelerations is given by (Marques et al., 2017)

$$\mathbf{M}\dot{\mathbf{v}}_i = \mathbf{g} \ (i = 0) \tag{4.32}$$

with i being the ith iteration. Thus, the iterative process continues with

$$(\mathbf{M} + \alpha\mathbf{D}^{\mathbf{T}}\mathbf{D})\dot{\mathbf{v}}_{i+1} = \mathbf{M}\dot{\mathbf{v}}_i - \alpha\mathbf{D}^{\mathbf{T}}(-\boldsymbol{\gamma} + 2\mu\omega m_c\dot{\boldsymbol{\Phi}} + \omega^2 m_c\boldsymbol{\Phi}) \tag{4.33}$$

Until

$$\|\dot{\mathbf{v}}_{i+1} - \dot{\mathbf{v}}_i\| \leq \varepsilon \tag{4.34}$$

where ε is a specified tolerance.

This method involves the solution of a system of equations with a dimension equal to the number of coordinates of the multibody system. The penalty terms associated with the velocity constraints are the same as the ones used in the penalty method. The augmented Lagrangian method presents itself as an effective, efficient, and robust method, especially when performing forward dynamic simulations, such as the one created for this work.

5. VEHICLE MODELLING

In this chapter, all theory presented previously will be put to the test to satisfy the primary objective of this dissertation, create a vehicle dynamics analysis method for multibody systems. Firstly, a tire force model will be chosen and validated. This will be the kernel of the dynamics analysis since the contact forces between tire and road will be identified and analysed. Then, the multibody dynamics methodology used will be explained. This was done through a MATLAB program developed by Flores P. (2012), that will be briefly described.

Finally, the contact estimation model created as part of this work will be presented and thoroughly clarified, culminating in two different methods: one for flat roads and the other for roads with obstacles. The tire force model will, in fact, be integrated into the aforementioned algorithm to create a cohesive and extensive contact model.

5.1 Tire Model Validation

As previously discussed, there are several different models to simulate the contact between a vehicle's tire and the road, which can be categorized as mathematical or physical.

It is known that without the mathematical there would be no physical models. Physical models also derive from mathematical formulations, making them quite more powerful and precise. These models can precisely simulate conditions like the temperature of a tire throughout the time it is rolling, the resulting inflation, and subsequent deformation. Additionally, they are capable of scrutinizing individually the different layers that make up a tire, while also evaluating the response to short road asperities or non-rigid roads, much like mud. Most importantly, they can predict the transient behaviour of friction forces. An example of this, would be a finite elements model or the known SWIFT model.

However, in the end, they always require more processing power and are related to higher acquisition costs, which makes them harder to implement in such works as this one. Also, in this work, it is not necessary to go that deeply into the study of a tire since the main focus is to gather information about the behaviour of the suspension system when facing different roads with obstacles. Also, the transient generation of friction forces can be neglected, and the forces will be generated as if the car was cruising at a constant velocity. This can be considered as a minimal effect that will not significantly affect the study of the multibody system, since the behaviour of the suspension system will not be significantly altered due to the existence or not of dynamic forces. It is expected that parameters such as slip or slip angle

will fluctuate, around small values, very slowly over time, therefore there is no need to use a transient slip (they can change, but the change will be uniform, not sudden).

It is then comprehensible that one should opt to choose a much simpler mathematical model, or, at the very least, a semi-empirical one. Nevertheless, it is important to state that in no way a test rig is available, which is necessary to measure a few variables for some semi-empirical models. For example, the TMeasy model (Rill G. , 2019) requires the input of some experimentally measured variables to create the definitive curves, such as the longitudinal force for a specific vertical load.

Two other models that satisfy the requisites previously imposed are the Dugoff model (or the Modified Dugoff model) and Pacejka's Magic Formula. As it is known, the Magic Formula is a semi-empirical tire model, that needs the input of several experimentally measured parameters, acquired through testing a tire on a test rig. Nonetheless, the so-called Magic Formula Parameters are widely available (across a number of studies, papers and research) for an extensive list of tires, and are also easily adapted to any real circumstance, making this model one to take into account. As for the Dugoff, and subsequently its modified version, albeit with its frailties, it presents itself as an easy-to-use, purely mathematical model, that does not need experimental values to work. The choice, then, lies in the differences between both models.

As mentioned above, the Dugoff model is substantially improved when applied a modifying factor (Bian, 2014; Bhoraskar & Sakthivel, 2017). Opposite to the original, the modified Dugoff model prescribes, for example, the location of a peak value for the longitudinal force, immediately before the beginning of the sliding zone. Additionally, the modified version represents quite well the gradual reduction of longitudinal force in the same area until the total loss of adhesion is attained, when the value of slip reaches its peak at 1.

The Magic Formula (MF) is a staple in the world of tire models. Not only it is easy to implement but also it provides highly reliable results. For both pure slip and combined slip situations, this model captures, almost perfectly, the non-linear behaviour of the tire. Moreover, it can describe in detail the forces and torques generated in the contact patch. In addition, it is possible to introduce some tire manufacture aspects that significantly alter the shape and look of the curves that represent the forces.

For a correct choice, both models were tested for their ability to compute both longitudinal and lateral forces with a variable vertical load. The results of the calculus of the longitudinal force are shown in Figure 5.1.
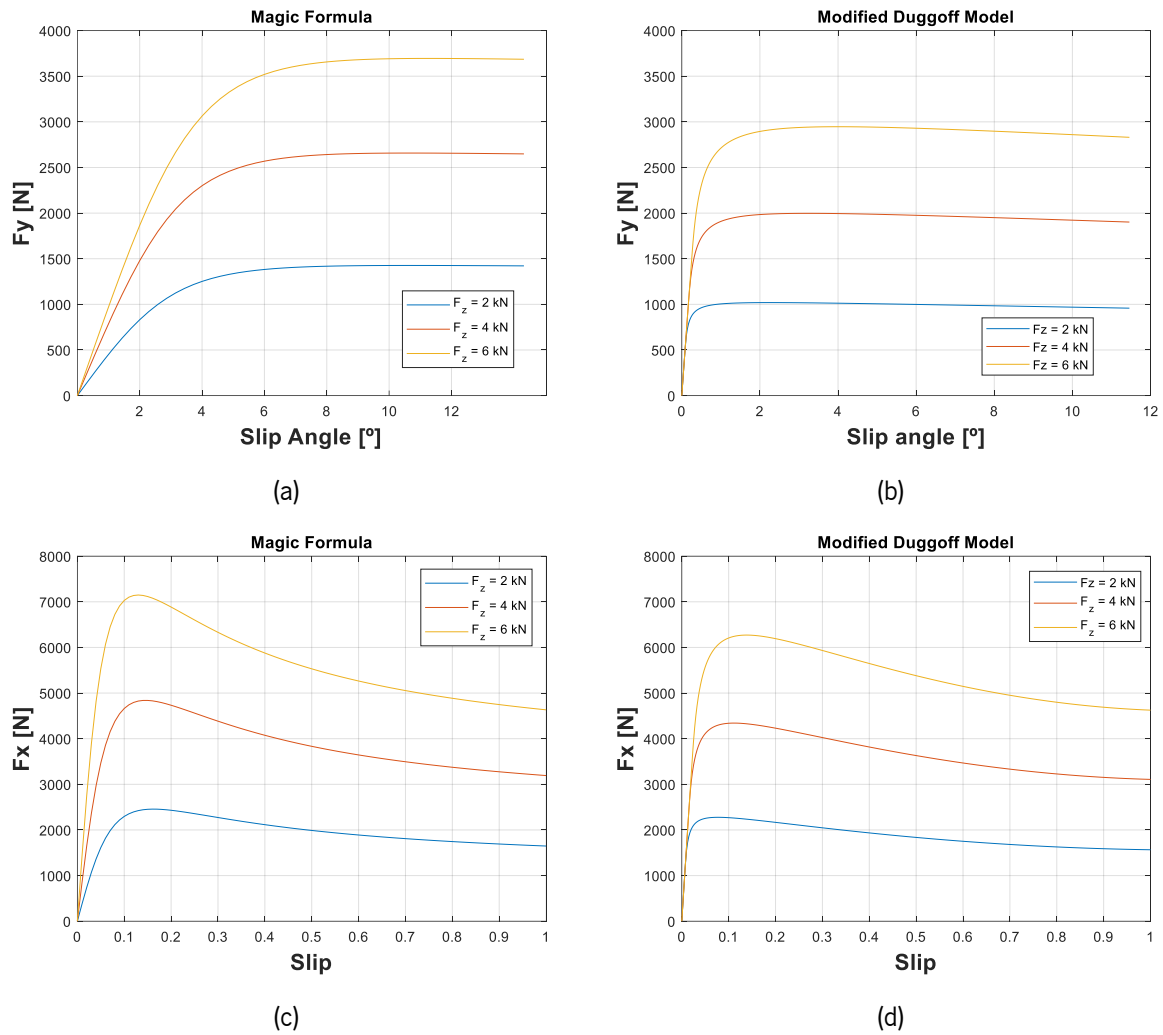
Figure 5.1 - Comparison between the MF (left) and the Modified Dugoff Model (right).

Although the obtained curves are similar, a closer look will show that in the Dugoff model the longitudinal force's peak is attained later, with a much smaller magnitude (the MF provides almost 1 kN more for the largest vertical force 6 kN). Also, for bigger vertical forces, the gradient of the linear zone of the longitudinal force increases, moving the force's peak to smaller slip values, which corresponds to what was given by the brush model. It can be said that Magic Formula provides a more adequate and closer-to-reality representation of the contact forces.

In addition, the Magic Formula provides several equations and formulae to estimate the different torques generated by the tire's contact forces in the contact patch. These formulae can be extremely explicit to the point of, if desired, considering residual effects, such as the camber effect on the lateral force (that makes it not be, in any given point, zero). Oppositely, the modified Dugoff model does not confer such alternatives.

Finally, the Dugoff uses the same relationship for both pure and combined slip situations. This could potentially create unreliable results since the Dugoff factor can be perceived as nothing more than a

simple ratio between the longitudinal slip and the slip angle (lateral slip). On the other hand, Pacejka's Magic Formula separates both cases, creating a different cluster of equations to represent the combined slip scenario. In fact, this set of formulae are always dependent on the results obtained in pure slip situations. One can state that the Magic Formula approaches this scenario in the same way as the Dugoff model, by creating a ratio (of factor) between slip quantities and multiplying it by the pure slip values, that is.

It is then comprehensible that choice of model to use falls on the Magic Formula. In addition to all aforementioned reasons, this model is also extremely easy to use and implement and does not require a lot of computation and processing power. Its complexity, in comparison with the Dugoff models, relies solely on its set of equations.

The Magic Formula's basic model has already been presented and discussed in section 3.3. It is, nevertheless, necessary to clarify the fact that the mentioned model is the Formula's simplest form. Hans B. Pacejka, in his book (Pacejka, 2002), presents an extensive collection of equations, which allow a thorough calculation of the forces and torques actuating on a tire. Since this is a dynamic study, when it comes to the simultaneous occurrence of both longitudinal and lateral forces, the formulae for combined slip situations were used in conjunction with the ones for pure slip conditions. These equations can be found in Appendix B. All Magic Formula parameters used, represented as different letters, are also represented in Annex A.

The next table shows the different friction coefficients considered for this study.

Table 5.1 - Coefficient of friction values.

Terrain	μ_x
Dry asphalt	0.7 - 0.9
Wet asphalt	0.6
Snow	0.3
Ice	0.1

5.1.1 Vertical Force

The vertical load is uniformly calculated by most authors. A most prominent example would be Pacejka's equation (Pacejka, 2002)

$$F_Z = \left(\delta_{Z0} \frac{F_{Z0}}{r_0} \right) \cdot \delta_Z \qquad (5.1)$$

This formula multiplies a tire's deflection with a stiffness value, defined by $\delta_{Z0} \cdot \frac{F_{Z0}}{r_0}$, giving a value for the normal load. It should be noted that this computation only considers the static aspect of the vertical force, only dependent on the stiffness of the tire. However, a tire does not solely possess stiffness, but also damping properties, which creates a dynamic member on the equation.

In the TMeasy model (Rill G. , 2019), the authors present a vertical force model, such as follows

$$F_Z = a_1 \delta_Z + a_2 \delta_Z{}^2 + c\dot{\delta}_Z \tag{5.2}$$

$$a_1 = \sqrt{2C_1{}^2 - C_2} \tag{5.3}$$

$$a_2 = \frac{C_2{}^2 - C_1{}^2}{4F_{Z0}} \tag{5.4}$$

This model contemplates two effects: the static, described by a nonlinear function of the tire deflection, and the dynamic, created by the wheel's damping. Both these terms allow for a detailed characterization of the vertical force at any given point. Nevertheless, it is important to state that the value for a tire's damping is usually very low, at least for passenger cars, having no significant expression when compared with the damping offered by a car's suspension. In fact, the damping provided by the suspension is 10^4 times bigger than the one yielded by the tire (Rill & Castro, 2020). Nevertheless, Rill's model, Eq. (5.2), was chosen to evaluate the vertical force in this work, always taking into consideration the tire's own damping value.

5.2   Multibody Dynamics Methodology

The scope of this work is defined by the study of a multibody dynamic simulation of a car to examine its suspension system. In chapter 4, some concepts and formulations were present to better understand the dynamics of generalized multibody systems. Herewith, in this subchapter, the methodology used in this project to study multibody systems, more specifically vehicles, will be explained.

First and foremost, it is necessary to state that a MATLAB program, named MUBODYNA3D (Flores P. , 2012), was used. To put it briefly, this program performs forward dynamic analysis of general spatial mechanical systems, closely following the formulation presented in the textbook by P.E. Nikravesh (Nikravesh P. E., 1988).

In this section, the methodology used by MUBODYNA3D will be presented in a concise manner. Briefly, MUBODYNA3D is a MATLAB program, which consists of several scripts. These scripts are used to define several different aspects of the simulation and the multibody system. Finally, a case study will be demonstrated in chapter 6.

The first thing necessary to a multibody simulation is arguably the definition of the multibody system. As is known, a mechanical multibody system is constructed by mechanical components and kinematic joints (Flores P., 2015; Marques et al., 2017). Also, one can consider the existence of a third one, which would be the force elements. These are responsible for the application of forces over the system.

With the above information in mind, one can easily create a multibody system. Within the spectrum of the methodology in study, the user must create a model that establishes a multibody system. This model will be made of several scripts, each one presenting the following characteristics:

- Bodies

- Points

- Type 1 Vectors

- Type 2 Vectors

- Joints

- Forces

- Solver

- Properties

With all the scripts created, a multibody system is defined and, so, its behaviour can be, accordingly, simulated. Each point listed before will be thoroughly explained in Table 5.2.

Table 5.2 - Components that define a multibody system in MUBODYNA3D (Flores P. , 2012).

Element	Purpose
Bodies	This is where all bodies within a multibody system will be defined. Each body is specified by: • Mass • Inertia matrix • Initial position • Initial velocity
Points	Points, in each body, can be defined. Especially useful to interconnect bodies.
Type 1 Vectors	Vectors within each body can be created. A known example would be the rotation axis of a wheel.
Type 2 Vectors	Type 2 vectors are vectors created between points in different bodies. Especially important in order to designate some types of joints' axis of rotation. These specific vectors are calculated throughout the running duration of the simulation since its points may change position.
Joints	Where several types of joints between bodies can be created, such as cylindrical, or spherical. This script requires all the previous scripts to work.
Forces	In here, all force elements actuating on the bodies can be defined. Also, forces such as the weight and external forces, such as the tire/road contact, can be designated to each body.
Solver	Contains all the necessary computational element, such as the simulation duration and the method used to solve the equations of motion.
Properties	This file contains some general properties of the system in study, most likely physical parameters.

As was stated before, the definition of a multibody system's joints requires the use of several other characteristics, such as points, type 1, and type 2 vectors. Table 5.3 presents the necessary elements to establish some types of joints analysed in this project.

Table 5.3 - Necessary attributes to define some types of joints.

Joint	Points	Type 1 Vectors	Type 2 Vectors	DoF
Cylindrical	2	2	1	2
Spherical	2	-	-	3
Revolute	2	2	-	1

5.2.2 Pre-Processing Stage

The next step in the chain would be the pre-processing of general information, also known as initialization (it is separate script from the main MUBODYNA3D file). In a broad sense, in this stage some matrices, arrays and such are established. In other words, important information that would be used later in the process is processed and saved. Nevertheless, this is an especially relevant stage since it loads the model into the simulation by reading and processing its information and establishes the several components and associations between them.

Information such as the number of bodies, their characteristics, forces to be applied is all stored in the model that the user first created. In this stage, with the initialization script, all that information will be read, processed, and saved, in a specific order:

1. Bodies: All bodies are established. Their characteristics, such as Jacobian matrix, mass, transformation matrix and so on, are set up as matrices.
2. Points: All points are associated with their bodies.
3. Vectors (Type 1 and 2): Vectors of both types are built and associated with the specific bodies.
4. Joints: All the joints are established. All points and vectors (if necessary) are attributed to each existing joint. Then, the bodies are assigned to each created joint. Finally, the number of constraints posed by each joint is computed. For example, a spherical joint imposes 3 constraints on the body.

After the aforementioned steps have been concluded, the total number of kinematic constraints prevailing in the system is computed and the pre-processing stage for generic models is complete.

Nevertheless, for non-generic models (models that require, for example, external force models, created solely by the user), such as the tire/road contact, some more pre-processing steps were created specifically for this dissertation. As will be seen later, a road profile, as well as a tire profile, were created externally, within a different script, to represent the real tire and road that the vehicle will need to negotiate. So, in the pre-processing stage, a few more steps will be needed:

5. Definition of the tire's profile, for both left and right wheels. Both profiles are transformed into cubic splines, so that is possible to interpolate points that are in between the sample points that define the profile

6. The various types of road profiles are loaded and saved into the system. The road profile also receives a spline-like treatment.

While the tire profile is simply merged into a cubic spline, the road profile needs a deeper treatment. There are two types of roads: one with a fully flat surface and another with obstacles, like bumps or potholes. For a fully flat road, the treatment is completely straightforward: the only necessary thing is to compute its height and save as a constant value. For a road with obstacles the scenario is completely different.

Firstly, the uneven road will be rearranged as two different cubic splines: the first one correlating the length of the road with its height (x and z); the second one interpolating the width and the height of the road (y and z).

It is important to note that the coefficients of both splines are saved to be used later but are not computed through the MATLAB function known as spline (spline Documentation, s.d.). As the name indicates this function returns a vector of interpolated values, through a simple piecewise cubic Hermite interpolation. However, the function used to interpolate the mentioned profile is known as *pchip* (pchip Documentation, s.d.). Like the first function, this also performs a piecewise cubic Hermite interpolation. Although they perform the same type of interpolation, both these functions differ severely in the method employed to compute the slopes of the interpolant. This does result in distinctly different behaviours for the data with flat or undulating areas. Therefore, the values interpolated through the *pchip* function are determined by a shape-preserving piecewise cubic interpolation (pchip Documentation, s.d.). Figure 5.2 shows a bump modelled with both functions. Macroscopically they seem exactly the same, the differences are only noticeable when zoomed in.
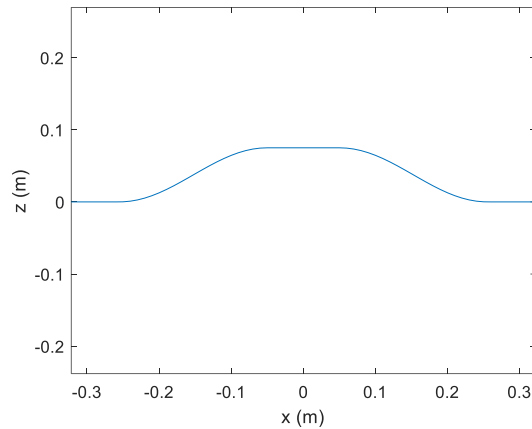
Figure 5.2 - Example of a road profile using both MATLAB functions.

Unlike the function spline, the function *pchip* avoids overshoots and can correctly connect plane regions withing the function Figure 5.3. This is especially important for the definition of a road. A totally flat road must be completely flat. The existence of unrealistic oscillatory overshoots makes the performance of the car to be entirely differently, particularly considering that instead of traversing a flat area, the car could be crossing an uneven ground, created by oscillations. The function *pchip* eliminates those unwanted overshoots and is, hence, used in this work.
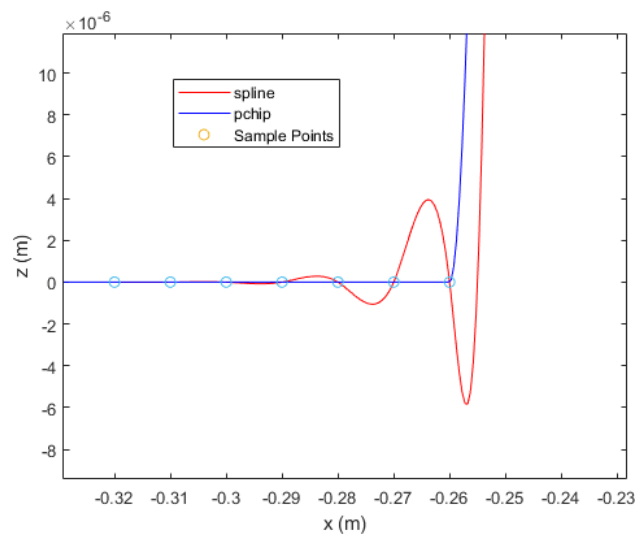
Figure 5.3 - Comparison between the road profile using a normal spline function and the *pchip* function.

5.2.3 Choosing the Integrator

The next step in the multibody dynamics' methodology is the choice of what integrator to use.

An integrator is an algorithm that approximates a trajectory in a system based on initial conditions and knowledge of its equations of motion. A system's trajectory can be constructed through the integration of its derivatives, such as the acceleration given by the equations of motion (Flores P. , 2015).

There are several types of integrators, most commonly using a Taylor expansion to get the dynamics of a system. These can range from the simplest, yet poorly accurate, Euler's Method integrators, that invoke 1st order expansions, to the Runge-Kutta integrators, either being of the 2nd or 4th. The largest the order expansion, the most accurate the integrator is, but at the same time the longer it takes to operate. There is always a trade-off between an integrator's performance and how long it takes to obtain results (A. Keller, 2018).

Although all the above-mentioned integrators are plausible choices, and can be used in the MUBODYNA3D program, MATLAB offers ODE solvers with variable timestep (Choose an ODE Solver, s.d.). ODE, also known as ordinary differential equation, contains one or several derivatives of a time dependent variable, so that its order is equal to the highest-order derivative of said dependent variable that appears in the equation.

The ODE solvers are particularly appealing for initial value problems, such as the one studied in this work (see chapter 6). Starting at an initial state, a solution for the ODE is attained iteratively, by using initial conditions and knowing the period over which the answer is required. In the end, the solver returns the solution at each timestep, as well as a vector of timesteps (Choose an ODE Solver, s.d.).

MATLAB provides several different types of ODE solvers, with different requirements and accuracy. It is, firstly, important to state that from now on, the integrators used in this work will be of the ODE type. Table 5.4 presents three relevant types of solvers provided by MATLAB. Other types can be found in (Choose an ODE Solver, s.d.).

Table 5.4 - Some types of nonstiff Ode solvers (Choose an ODE Solver, s.d.).

Solver	Problem type	Accuracy	When to use
Ode45		Medium	Standard. Always the first to try
Ode23	Nonstiff	Low	For problems with crude tolerances
Ode113		Low to High	For tight tolerances

One final concept arises from the analysis of Table 5.4. A stiff problem is a problem difficult to evaluate. It is a differential equation in which several numerical methods are unstable, unless the step size is extremely small (Choose an ODE Solver, s.d.). A nonstiff problem is the polar opposite. These are easily identifiable by checking the performance of each solver. So, if a nonstiff solver is extremely slow, or unable to solve the problem, then the problem might show stiffness. Generally, contact problems require stiff problems. However, since the tires are made of rubber, a soft material, and, in this case, will not suffer major impacts, the nonstiff algorithms are more appropriate to this study.

Another characteristic of this type of integrator is the variable timestep. This is showcased in Figure 5.4, where a 2 s simulation was performed and around 12000 timesteps obtained. The evolution of time with the timesteps is not always linear and uniform. At around $t = 1.10$ s, the time which had been evolving linearly hits a plateau and stays there for 2000 timesteps. Before this, for a second of simulation, only 3000 steps were needed. Now, for 0.10 s, almost the same amount of timesteps was needed to move forward. This guarantees that the best solution is always found. When a demanding situation happens, the solver utilizes smaller timesteps to deliver good results. Sometimes, if the solution is found not to be the best, then the solver traces back to a previous timestep and restarts the integration from there.

(a)   (b)
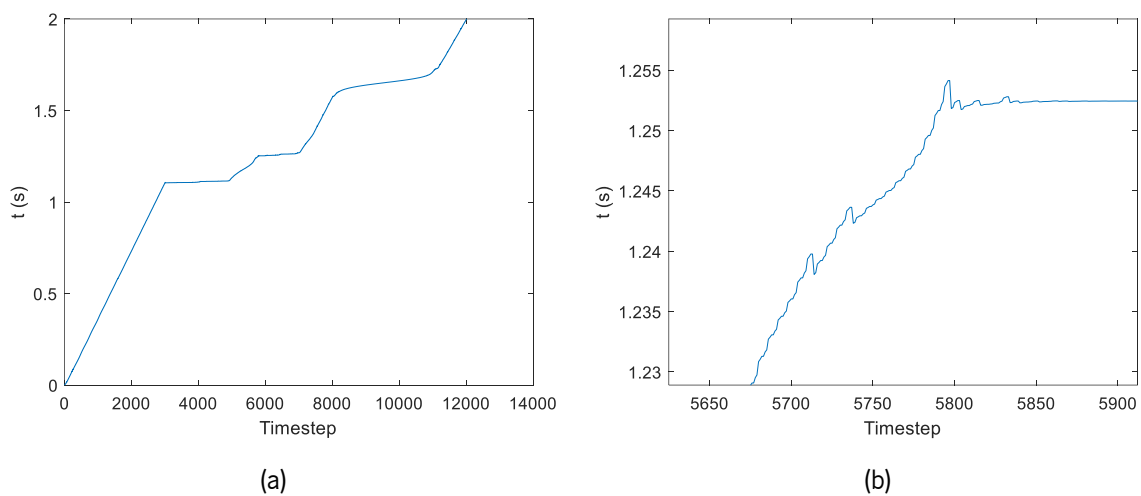
Figure 5.4 – (a) Example of the variable timestep for a 2s simulation, using the ode45; (b) Zoom in on (a).

5.2.4   Correction of Initial Positions and Velocities

After the integrator has been chosen, the program initializes a correction step. In this stage, the initial conditions will be corrected and there will be a check for redundant constraints, in order to accommodate all joints within the bodies and create a viable solution. This stage is processed in two steps:

- Coordinates (position) correction
- Velocities correction

The coordinate correction follows a simple algorithm. Firstly, the violation of constraints and Jacobian of the body are obtained and put into a matrix. If that matrix's determinant is smaller than a tolerance, then there is no need for a correction. If it is not, then, iteratively, the formulation presented in Appendix C is applied until the requirement is met. The velocity correction follows the exact same method.

A function to update the position of the bodies is called, during the resolution of the first algorithm. This function computes the rotational transformation matrix, $\mathbf{A}$, based on the knowledge of the Euler's

parameters. With the matrix, the position of the body, locally and globally, are obtained, with the corrections already made. This will be called for each iteration of the process. So, in summation, the corrections are made, the position is update, and the new coordinates are verified. If that verification checks the requirement, then the corrections are complete. If not, the cycle continues until a solution is found or until a flag is met, meaning the impossibility of correction of the initial conditions

5.2.5   Solving the equations of motion

After establishing the multibody model, defining the settings for the dynamic simulation and pre-processing data, the dynamic equations of motion must be solved for each timestep of the simulation using methods described in section 4.4 and, then, the obtained acceleration integrated through time with the algorithms previously discussed in section 5.2.3.

In this work, the augmented Lagrangian method was always used, because of the way it penalizes the constraints violations and, especially, handles singular matrix configurations.

A function with this method is employed to compute and solve the constrained equations of motion at each timestep. The positions and velocities are the input variables, which allows to evaluate all position and velocity constraints, assess the forces acting on the bodies of the system and, the, compute the accelerations at that instant. Since this is a penalty method and iterative process, the accelerations are calculated until a threshold value (tolerance) is met. With the accelerations, the solver can then integrate them and get the position of the bodies for the next time step. This happens for each time step until the final time is met.

In the end, a number of evaluations is computed, and the time of simulation obtain, finishing the simulation process.

5.2.6   Assessment of Forces

In this intermediate stage, all forces and torques affecting the bodies are calculated. Some forces can be defined through the user interface, such as the weight or spring-damper forces.

This last example would be formulated as

$$F = k(\delta - \delta_i) + c\dot{\delta} \tag{5.5}$$

where k is the spring stiffness, δ_i represents its undeformed length and c denotes the damping coefficient.

The spring's deformation, δ, as well as its derivative, $\dot{\delta}$, are easily obtained through a vector that joins two different bodies (type 2 vector). Associated torques can also be calculated through the location of the application point in each body.

Additionally, other types of forces can be defined, this time needing to be solely implemented by the user. In the case of this work, this would correspond to the contact road/tires force model, which formulation will be presented in the next section.

5.3 Tire/Road Contact Formulation

To properly study the influence of the tire-road forces on a vehicle's suspension system, it is necessary to compute them. As has been seen before, it is possible to calculate the values by modelling the contact between the tires and the road the vehicle.

In that regard, it was necessary to formulate and create a methodology to estimate the contact between vehicle and the road. For instance, this methodology is mainly responsible to calculate the vertical force that is acting on a vehicle's tires. That value is then inserted into a tire model, previously chosen as the Magic Formula, which makes possible the obtention of all the forces and torques that act on the tire, during the contact with the surface, as previously seen in Figure 3.1.

In short, the algorithm, which will be presented next, was built to detect the contact between a single tire and the road, hence the name Tire/Road Contact formulation. The algorithm illustrated in Figure 5.5 represents the logical steps to estimate the location of the contact point and, accordingly, the forces, on all three axes (vertical, longitudinal, and lateral). It should be emphasized that this formulation is only for a singular wheel, thus, the algorithm must be applied four times at each time step.

t → | Contact Estimation | → | Tire Force Model | → | Add forces to bodies | $t = t + \Delta t$ →
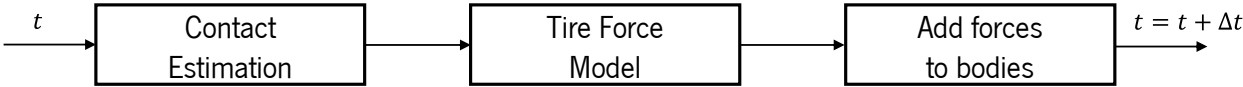
Figure 5.5 - Algorithm for solving the tire/road contact estimation at a given timestep.

5.3.1 Contact Estimation

The first step consists of the estimation of the location of the contact point, between the tire and the road. This is especially important to evaluate the amount of deflection a tire is undergoing, which, in turn, grants the calculation of the vertical load. Also, it allows the approximation of a point where all forces are being applied, so that all torques are then calculated correctly and the tire under an accurate vertical pressure distribution. Note that in this work, all forces will be applied at a contact point, not at the full area of the contact patch.

It is important to note that the multibody system, which is defined previously and loaded into the system during the pre-processing stage, is already available to be used during the contact estimation. Constructive parameters, such as the tire's radius or the Magic Formula parameters, can also be used in this stage.
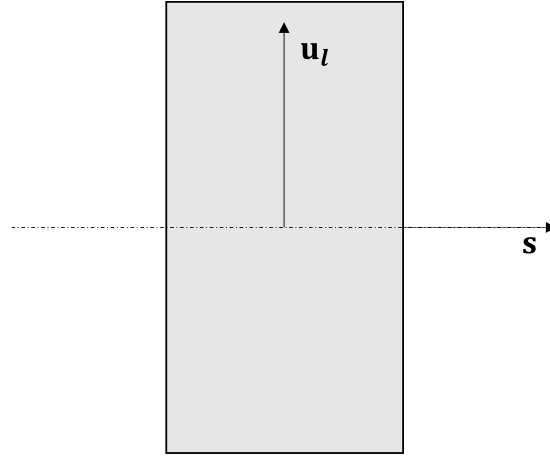
Figure 5.6 - Free-body diagram of the wheel, top-down view.

After the general variables are defined, it is necessary evaluate the tire's behaviour, as in the location of its centre of gravity, its linear and angular velocities and, finally, its axis of rotation. Almost all this information is given by the MUBODYNA3D program, after the model/body is created. The sole exception is the tire's rotation axis, which needs to be created in each wheel local coordinate system

$$
\mathbf{s}_p = \begin{bmatrix} 0 \\ 1 \\ 0 \end{bmatrix}
\tag{5.6}
$$

Since, in the beginning of the simulation, the wheel is aligned with the global reference frame, this vector represents the body's rotation around the y axis. Thus, the initial angular velocity of the wheel can be defined as

$$
\boldsymbol{\omega} = \begin{bmatrix} 0 \\ V_0/r_0 \\ 0 \end{bmatrix}
\tag{5.7}
$$

where V_0 is the wheel's initial velocity, and r_0 its nominal radius. Additionally, its initial forward (longitudinal) velocity in the global frame would simply be

$$
\dot{\mathbf{r}} = \begin{bmatrix} V_0 \\ 0 \\ 0 \end{bmatrix}
\tag{5.8}
$$

These vectors change during the simulation to accommodate of the equations of motion. Although both angular velocity of the wheel and rotation axis are already known, it is imperative to compute the component of angular velocity, around the axis of rotation represented in the global frame of reference, $\mathbf{s}$.

This vector derives from $\mathbf{s_p}$ and is given automatically by the program. This is done by calculating the scalar, or dot, product of both those variables, which yields

$$\omega_s = \mathbf{s\omega} \tag{5.9}$$

where $\mathbf{s}$ can be obtained through the rotation of the local vector

$$\mathbf{s} = \mathbf{A}_i\mathbf{s}_p \tag{5.10}$$

Knowing the position and velocity of the wheel, the next step is to determine the location of the contact point and compute the deflection of the tire at a certain moment in time. In this work, two types of roads were considered, i.e., fully flat and with obstacles (bumps or potholes). Each type of road must be analysed separately, since two different methods to find the contact point were developed, one for each type of road.

Fully flat road

This is the simplest case since the height of the road is uniform across its length and width. A simple algorithm created for this type of road is represented in Figure 5.7.The first step to solve this case is the establishment of a fixed local reference frame, with immutable ξ and ζ directions. Since the local frame of the body follows its orientation, the rotation of the tire would change the direction in which ξ and ζ were pointing, as shown in Figure 5.8.
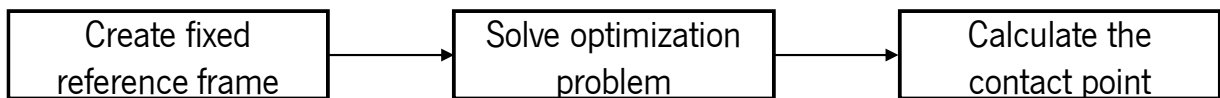
Figure 5.7 - Algorithm for the estimation of the contact point on a fully flat road.
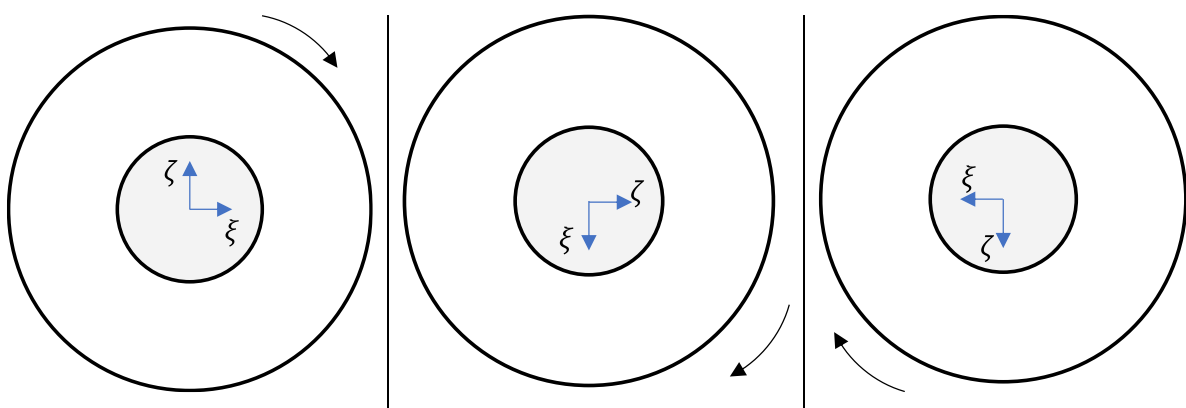
Figure 5.8 - Rotation of the wheel's local reference frame.

Let us suppose that the longitudinal axis was needed to define the direction of the longitudinal force. If the axis were always changing direction, then, at some stage, instead of being a longitudinal force, that force would become vertical or lateral. This issue creates unwanted problems, when performing several

calculations. Therefore, before setting the local reference frame, let us define the global normal direction with respect to the road

$$\mathbf{n} = \begin{bmatrix} 0 \\ 0 \\ 1 \end{bmatrix}$$

(5.11)

This vector is uniform throughout the length and width of the flat road as represented in Figure 5.9, since there are no changes in the gradient of the road surface (the surface is fully flat, with no inclines).
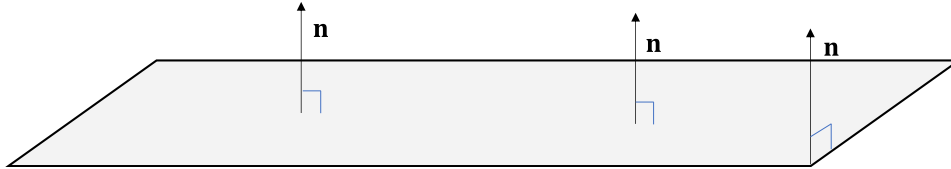
Figure 5.9 - Representation of the flat road with the normal vector, $\mathbf{n}$.

With the global normal vector and the rotation axis of the wheel, $\mathbf{s}$, one gets the other directions by

$$\mathbf{u}_l = \frac{\mathbf{s} \times \mathbf{n}}{\|\mathbf{s} \times \mathbf{n}\|}$$

(5.12)

$$\mathbf{u}_v = \frac{\mathbf{u}_l \times \mathbf{s}}{\|\mathbf{u}_l \times \mathbf{s}\|}$$

(5.13)

where $\mathbf{u}_l$ is the longitudinal direction, $\mathbf{s}$ the lateral direction and $\mathbf{u}_v$ the vertical direction of the tire. The vector product between two directions was divided by its norm, so that the result is presented as a unit vector. This is nothing more than anchoring the local frame of reference of the tire, $\xi\eta\zeta$, which has its origin at the centre of gravity.

Finally, the transformation matrix associated to this reference frame yields

$$\mathbf{A} = \begin{bmatrix} \mathbf{u}_l & \mathbf{s} & \mathbf{u}_v \end{bmatrix}$$

(5.14)

Without the existence of any gradients, the variation of the tire's deflection will be very small. Thus, the identification of the contact point can be done by directly intersecting the tire's profile with the road's profile. Have in mind that the tire needs to start with a deflection close to its real static value and, since the position of the bodies is defined by the user, adjustments may have to be done to accommodate for that fact (see section 6.1). The static deflection can be gathered by using the static member of the vertical force model, so that

$$0 = -F_z + a_1\delta_z + a_2\delta_z{}^2$$

(5.15)

The value for the static vertical force, for a singular wheel, equals to the weight of the vehicle divided by four wheels.

As mentioned in the pre-processing stage of the multibody dynamics methodology chapter, the profile designed for a specific tire (given as a cluster of points) was interpolated into a spline. Since the flat road

can be simply characterized by its constant height the position of the tire profile will define the location of the contact point. Thus, an optimization procedure is sued to find the point of the wheel profile with the lowest height. Bearing that in mind, a MATLAB function called *fmincon* is employed, which uses a gradient-based method to find the minimum value of an objective function inside a prescribed domain (fmincon Documentation, s.d.).

As observed in Figure 5.10, one local coordinate frame needs to be established $(u, f(u))$, in which the two-dimension wheel profile is given. The profile is given as a set of points defined by their lateral wheel coordinate, u, and the corresponding ordinate, $f(u)$, which are then interpolated using piecewise polynomials, i.e., splines. Recurring to the optimization function, one can find the u coordinate that corresponds to the minimum vertical coordinate within the tire's profile represented in the global reference frame (xyz), $z_{\min}$, as depicted in Figure 5.10.
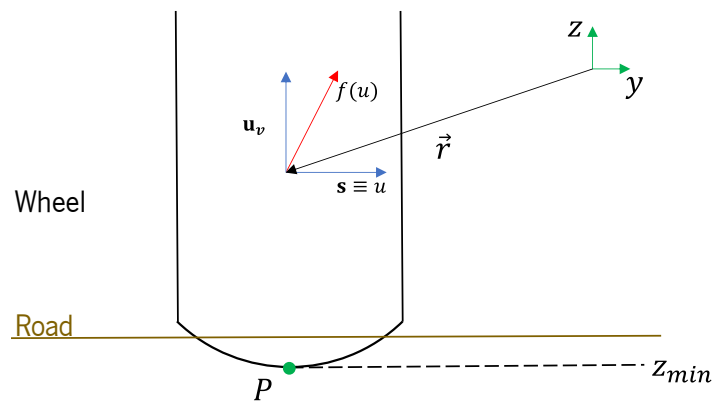
Figure 5.10 - Establishment of the local coordinates within the tire profile.

To get *fmincon* to work, a function to minimize, also known as objective function, needs to be declared. The problem can be put as: which is the value of u that corresponds to minimum value of the wheel's vertical coordinate in the global frame? That function will serve as the base in which *fmincon* will work. To run the algorithm, an initial approximation of the wheel's lateral parameter is given and, then, the following steps are repeated:

- Compute $f(u)$, evaluate the spline
- Calculate the contact point in the global reference frame, xyz
- Get the vertical coordinate out of that point
- *fmincon* iterates and finds z_{min} within the spline

The function *fmincon* iterates the value of u and runs the function, until a feasible solution is reached. A point on the wheel's profile in the global frame of reference is computed as (Flores P. , 2015)

$$\mathbf{r}^P = \mathbf{r} + \mathbf{s}^P \tag{5.16}$$

or, in expanded form as

$$\mathbf{r}^P = \mathbf{r} + \mathbf{A}\begin{bmatrix} 0 \\ u \\ f \end{bmatrix} \tag{5.17}$$

in which, $\mathbf{r}$ represents the centre of mass of the tire at that instance. The second member of the right-hand side of Eq. (5.17), also referred as $\mathbf{s}^P$ (see Chapter 4), represents the location of the point $(0; u; f)$ in global coordinates with respect to the local frame of reference $(\mathbf{u}_l \mathbf{s} \mathbf{u}_v)$. The value of $f(u)$ is obtained through the evaluation of the created spline using a MATLAB function called *ppval* (spline Documentation, s.d.).

The objective function ends with the computation of the vertical coordinate of the evaluated point

$$r^z = \mathbf{r}^P(3) \tag{5.18}$$

The objective of this stage is to find the u that corresponds to minimum value of r^z. The function *fmincon* will iterate the values of u, according to a previously defined interval, which is the domain of the spline's independent coordinate points. If the spline is defined with n points

$$u \in [x_{spline}(1), \dots, x_{spline}(n)] \tag{5.19}$$

The iteration will go on until a solution is found. The *fmincon* function will then return the u that solves the problem, $u_{\min}$, and the value of $z_{\min}$. To get the effective contact point in the global system it is necessary to run, just one more time, Eq. (5.17) and Eq. (5.18), with the value of u attained after the optimization procedure.

At last, the deflection of the tire is calculated as

$$\delta_z = z_{\text{road}} - z_{\min} \tag{5.20}$$

where $z_{\text{road}} = 0$ and $z_{\min} < 0$.

To obtain the tire tangential velocity, the velocity vector of the tire is projected onto the horizontal plane, so that

$$\mathbf{V}_T = \begin{bmatrix} \mathbf{V}(1) \\ \mathbf{V}(2) \\ 0 \end{bmatrix} \tag{5.21}$$

Road with obstacles

If the road possesses inclines or gradient variations, created by "large" obstacles, such as potholes, represented in Figure 5.11, or speed bumps/humps, another method to find the contact point needs to be employed. In this case, the method previously present does not work since the height of the round varies.
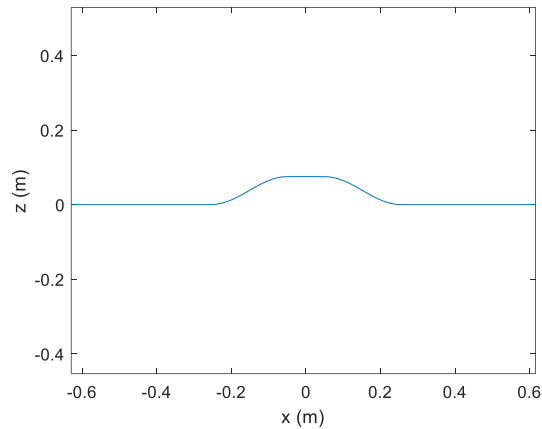
Figure 5.11 - Example of a road obstacle. In this case a bump.

Whilst in the first method, the contact point was always the one with the lowest vertical coordinate in the tire's profile, in the case of uneven roads, this formulation does not fully work. The tangent directions of the fully flat road, x and y, will be permanently constant, always perpendicular to the normal direction, which points upwards.

However, as depicted in Figure 5.12, that does not apply to a road with variable gradient. In fact, the changes in inclination promote a change in the direction in which the directional vectors of the road are pointing. Both tangential vectors, $\mathbf{t}_x$ and $\mathbf{t}_y$, define the longitudinal and lateral directions, respectively, in which the road is unfolding. These vectors are always perpendicular to the road's normal vector, $\mathbf{n}$.
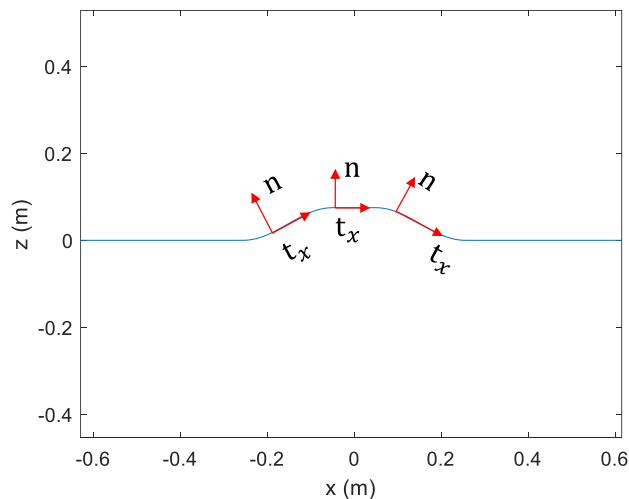
Figure 5.12 - Representation of the changes in gradient over a bump.

Figure 5.13 represents a wheel crossing an uphill road in the xz plane. To investigate the contact point, P in the xyz system, in such a case where the road has a variable gradient, an assumption must be made: The contact point, between the tire and the road, is a point which guarantees that a vector $\mathbf{d}$

is perpendicular to both tangential vectors, $\mathbf{t}_x$ and $\mathbf{t}_y$ (Rill G. , 2019). This formulation grants that, if calculated correctly, the contact point will correspond to the point where the tire deflection is maximum. This is always true for cases where there is only one contact point that meets the requirement. Later, it will be seen that this assumption will have to be slightly modified when multiple points meet the initial requirement.
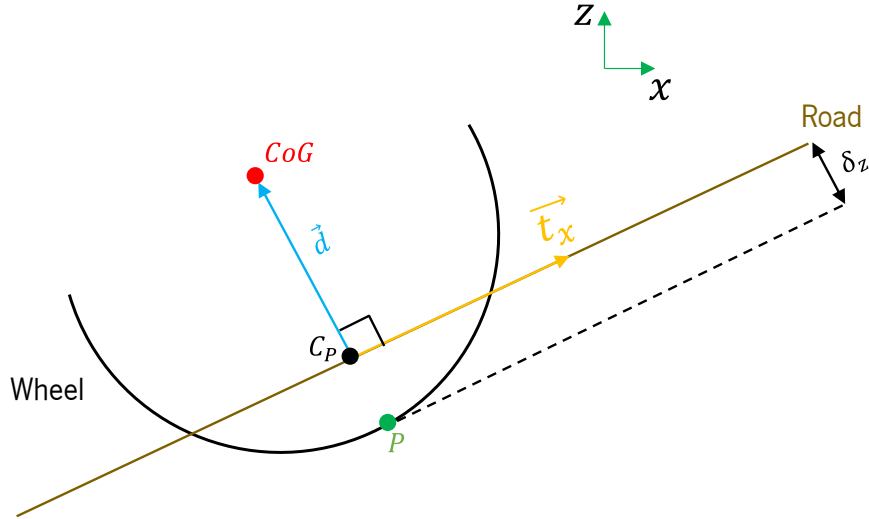
Figure 5.13 - Discretization of a wheel crossing an uphill road.

Let us define vector $\mathbf{d}$ as

$$\mathbf{d} = \mathbf{r} - \mathbf{r}^{C_P} \tag{5.22}$$

where $\mathbf{r}$ is the global location of the wheel's centre of gravity, and $\mathbf{r}^{C_P}$ represents the global location of the projection of the effective contact point, P, on the road.

It is known that the dot, or scalar, product is zero for perpendicular vectors. Therefore, the objective of this methodology is then finding the $\mathbf{r}^{C_P}$, that makes

$$\mathbf{d} \perp \mathbf{t}_x \wedge \mathbf{d} \perp \mathbf{t}_y \tag{5.23}$$

or, alternatively

$$\begin{cases} \mathbf{d} \cdot \mathbf{t}_x = 0 \\ \mathbf{d} \cdot \mathbf{t}_y = 0 \end{cases} \tag{5.24}$$

which is a system of nonlinear equations of the type $f(x) = 0$. MATLAB has an internal function called *fsolve* that is a nonlinear system solver (fsolve Documentation, s.d.). If $\mathbf{r}^{C_P}$ is the independent variable and the problem defined as $f(\mathbf{r}^{C_P}) = 0$, with the system of Eqs. (5.25) being the stop condition, then the *fsolve* function can find a solution iteratively, by manipulating the values of $\mathbf{r}^{C_P}$ and finding the one that meets the requirements. Remember Eq. (5.22), where $\mathbf{d}$ is said to be defined by $\mathbf{r}^{C_P}$, meaning this formulation holds. Figure 5.14 depicts the algorithm implemented for the second contact method.
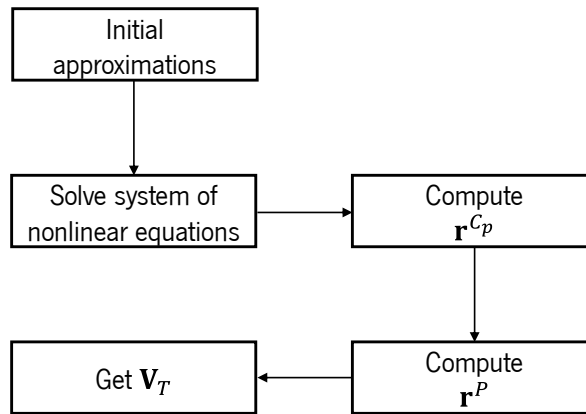
Figure 5.14 - Simple algorithm for the second contact method.

For *fsolve* to work, a function that computes the system of equations needs to be created. A suitable initial approximation of $\mathbf{r}^{C_P}$ must be provided to the function to stat the iteration procedure. That initial approximation would simply be the projection of the wheel's centre of gravity on the xy plane. In short:

- Initial approximation

- Iterate the value through a function

- Meet the requirement

This problem does not need to be solved in a three-dimensional space, because through interpolation the vertical coordinate of any point can be found. So, the initial approximation would be

$$x_i = \mathbf{r}(1) \tag{5.25}$$

$$y_i = \mathbf{r}(2) \tag{5.26}$$

A vector with both coordinates is created.

$$\mathbf{p} = \begin{bmatrix} x_i \\ y_i \end{bmatrix} \tag{5.27}$$

fsolve needs a function to work with, that establishes the stopping condition. This condition needs to have some sort of connection with the variable in analysis. The function used is of the type

$$f(\mathbf{p}, \mathbf{r}, \mathbf{x}_{pts}, \mathbf{y}_{pts}, \mathbf{spl}_x, \mathbf{spl}_y) \tag{5.28}$$

The last four variables, $\mathbf{x}_{pts}, \mathbf{y}_{pts}, \mathbf{spl}_x, \mathbf{spl}_y$, are the longitudinal and lateral coordinates of the road profile, and the splines created for each one during pre-processing. The first variable, $\mathbf{p}$, will be iterated by the MATLAB function until the final requirement is met. Nonetheless,

$$x_p = \mathbf{p}(1) \tag{5.29}$$

$$y_p = \mathbf{p}(2) \tag{5.30}$$

With both coordinates stored, there will be a search for them within the range of coordinates that define the road's profile, $\mathbf{x}_{pts}$ or $\mathbf{y}_{pts}$. The function *histc* counts the number of x_p or y_p values that are

within the specified range, which divided into bins, created between two different points (histc Documentation, s.d.).

As depicted in Figure 5.15, this function finds the bin, which contains x_p in the range of all points, or y_p if that were the case. By getting the endpoint, $x_{\text{bin}} / y_{\text{bin}}$, of the bin where x_p, or y_p, is located, it is possible to create a spline between those two points.
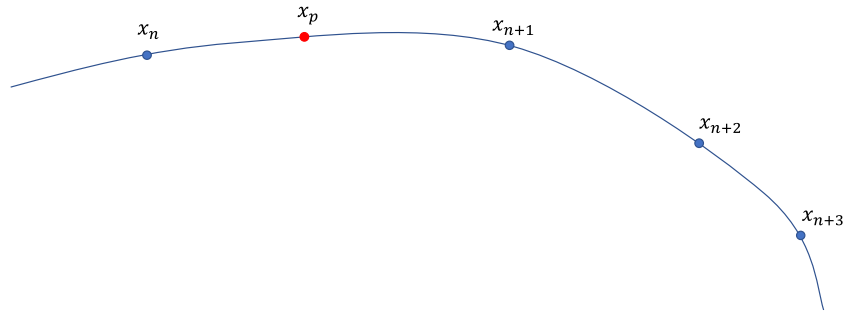
Figure 5.15 - Sample points connected by a spline. A bin is created between two blue points.

The road is divided into longitudinal, $\mathbf{spl}_x$, and lateral, $\mathbf{spl}_y$, splines that correlate the respective direction with the vertical coordinate of the road (section 5.2). Before finding the vertical coordinate that corresponds to the iterated point, **p,** smaller splines for each direction will first be created. Across the length and width of the road 's section, designated by *histc*, several one-dimensional splines will be defined. This allows to divide the interpolations into two different stages, one for x_p and another for y_p, saving computational time, instead of doing a two-dimensional interpolation. This provides a detailed and complex interpolation since the query point will be analysed across thousands of one-dimensional splines, on both lateral and longitudinal directions, such as depicted in Figure 5.16.
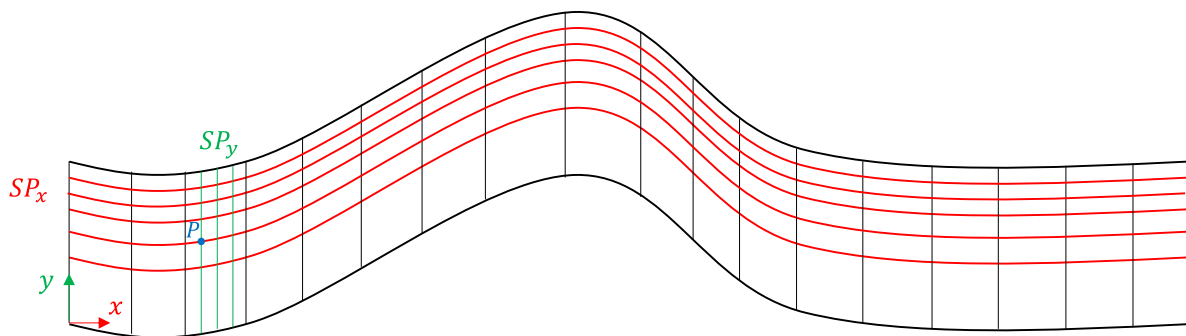
Figure 5.16 - Road profile divided into smaller splines.

For the longitudinal section provided by the application of x_p into the function *histc*, splines that run across the entire width of the road will be created

$$\mathbf{z}_{sy} = C_{x1}(x_p - x_{\text{bin}})^3 + C_{x2}(x_p - x_{\text{bin}})^2 + C_{x3}(x_p - x_{\text{bin}}) + C_{x4} \tag{5.31}$$

Eq. (5.31) provides the matrix with vertical values necessary to create the lateral splines. This is the inclination gradients along the longitudinal section in analysis, hence the use of x_p and x_{bin}.

The variables C_{x1}, C_{x2}, C_{x3}, C_{x4} are the road profile splines coefficients obtained during the pre-processing stage. This is done with a for loop, with the number of iterations equal to the size of the matrix that defines the road laterally, $\mathbf{y}_{pts}$. With $\mathbf{z}_{sy}$ and $\mathbf{y}_{pts}$, the MATLAB function *pchip* is used to create the one-dimensional lateral splines

$$SP_y = \text{pchip}(\mathbf{y}_{pts}, \mathbf{z}_{sy}) \tag{5.32}$$

After the lateral splines are created, it is time to interpolate the vertical coordinate of y_p. So,

$$z_{py} = C_{spy1}(y_p - y_{\text{bin}})^3 + C_{spy2}(y_p - y_{\text{bin}})^2 + C_{spy3}(y_p - y_{\text{bin}}) + C_{spy4} \tag{5.33}$$

Conversely, for the lateral section provided by the application of y_p into *histc*, splines that extend across entire length of the road will be created, as illustrated in Figure 5.16. Like in the lateral splines, the first step is to check the variation of the gradient across said lateral section. It is also done on a loop, with as many iterations as the size of the matrix that represents the road longitudinally, $\mathbf{x}_{pts}$

$$\mathbf{z}_{sx} = C_{y1}(y_p - y_{\text{bin}})^3 + C_{y2}(y_p - y_{\text{bin}})^2 + C_{y3}(y_p - y_{\text{bin}}) + C_{y4} \tag{5.34}$$

Then, the group of longitudinal splines can be created

$$SP_x = \text{pchip}(\mathbf{x}_{pts}, \mathbf{z}_{sx}) \tag{5.35}$$

and thus, the vertical coordinate of x_p yields

$$z_{px} = C_{spx1}(x_p - x_{\text{bin}})^3 + C_{spx2}(x_p - x_{\text{bin}})^2 + C_{spx3}(x_p - x_{\text{bin}}) + C_{spx4} \tag{5.36}$$

Usually, both interpolated vertical coordinates, given by Eq. (5.33) and Eq. (5.36), will be similar. To get the real value of $\mathbf{p}$'s vertical coordinate, a mean ponderation needs to be done, such that

$$z_p = \frac{z_{px} + z_{py}}{2} \tag{5.37}$$

Thus, the to-be-analysed contact point is given by

$$\mathbf{r}^{C_P} = \begin{bmatrix} x_p \\ y_p \\ z_p \end{bmatrix} \tag{5.38}$$

Also, $\mathbf{d}$, from now on known as distance vector, can be computed by Eq. (5.22). Hence, the tangential vectors to the road, exemplified in Figure 5.17, at the point in study need to be calculated.
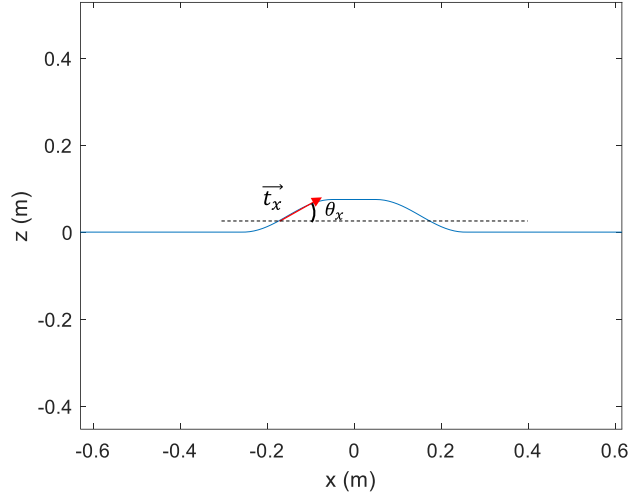
Figure 5.17 - Angle between the longitudinal tangential vector and the road.

The tangential vectors to the road, on both directions x and y, are the vectorial representation of the gradient of the road or, in other words, the graph's derivative. Obtaining the derivative of the point that is being study makes possible the computation of the tangential vectors at that specific location. The derivatives of the road's profile are of the type

$$\dot{z}_x = p_x = f(x) \tag{5.39}$$

$$\dot{z}_y = p_y = f(y) \tag{5.40}$$

Since the road's height (or variation) is now defined as two splines, or polynomials, its first derivatives, in each direction, can be obtained through derivation of the polynomials that define each spline. So, in the x direction, by derivation of Eq. (5.36) one gets

$$p_x = 3C_{spx1}(x_p - x_{\text{bin}})^2 + 2C_{spx2}(x_p - x_{\text{bin}})^1 + C_{spx3} \tag{5.41}$$

Similarly, by derivation of Eq. (5.33), in the y direction the gradient is

$$p_y = 3C_{spy1}(y_p - y_{\text{bin}})^2 + 2C_{spy2}(y_p - y_{\text{bin}})^1 + C_{spy3} \tag{5.42}$$

With the derivative calculated at the query point, the gradient as an angle can also be computed as

$$\theta_x = \arctan(p_x) \tag{5.43}$$

$$\theta_y = \arctan(p_y) \tag{5.44}$$

With these angles, the tangential vectors are presented as follows

$$\mathbf{t}_x = \begin{bmatrix} \cos(\theta_x) \\ 0 \\ \sin(\theta_x) \end{bmatrix} \tag{5.45}$$

$$\mathbf{t}_y = \begin{bmatrix} 0 \\ \cos(\theta_y) \\ \sin(\theta_y) \end{bmatrix} \tag{5.46}$$

The tangential vectors are ready to be introduced into the stop condition given by Eq. (5.24). The function *fsolve* iterates the values of the point, until the final requirement is met. However, the output will only be such that

$$\mathbf{r}^{C_{Pi}} = \begin{bmatrix} x_{\mathrm{pf}} \\ y_{\mathrm{pf}} \end{bmatrix} \tag{5.47}$$

where x_{pf} and y_{pf} are the final iterated values that meet the requirement.

To attain the vertical coordinate of the point given by the function, another step of interpolation will be necessary. In short, the same procedure, presented from Eq. (5.31) to Eq. (5.37), will be applied to $\mathbf{r}^{C_{Pi}}$, resulting in a final vertical coordinate, and so

$$\mathbf{r}^{C_P} = \begin{bmatrix} x_{\mathrm{pf}} \\ y_{\mathrm{pf}} \\ z_{\mathrm{pf}} \end{bmatrix} \tag{5.48}$$

Figure 5.13 shows that C_P is not the actual contact point on the tire, but rather a representation of that on the road's profile. It is an intersection with the surface. Therefore, the real contact point, in the xyz system (mind that C_P is also represented in global coordinates), needs to be computed. But firstly, the tire deflection on that point must be known

$$\delta_z = r_0 - \|\mathbf{d}\| \tag{5.49}$$

The real contact point is then given by

$$\mathbf{r}^P = \mathbf{r}^{C_P} - \left(\frac{\mathbf{r} - \mathbf{r}^{C_P}}{\|\mathbf{d}\|} \delta_z \right) \tag{5.50}$$

This method is always valid for a when a singular point meets the requirement imposed. However, as stated before, that is not always the case. In transition areas, where flat ground turns into an obstacle and vice-versa, another point can meet the requirement, as is observed in Figure 5.18: the vector distance, created by it, can be perpendicular to both road's tangential vectors.
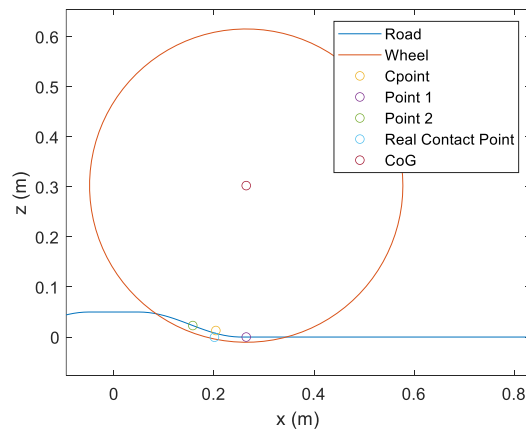
Figure 5.18 - Representation of a case where multiple contact points exist.

Also, in areas where the initial approximation is distant to the actual contact point, the function *fsolve* cannot calculate properly the wanted variables. This function solves the problem through derivation, with the direction in which the derivative is extending. With that it is possible to find the zeros of a function.
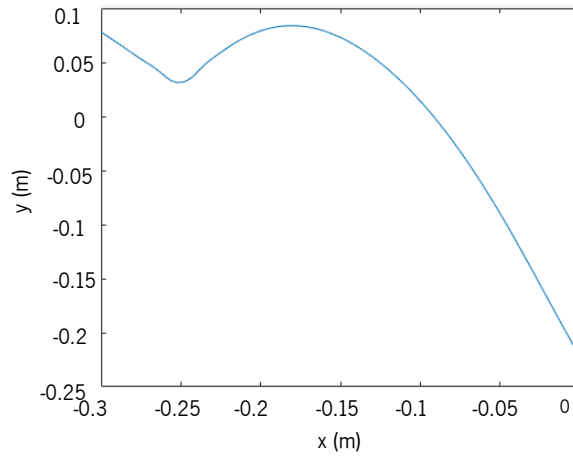
Figure 5.19 - Dubious case, where *fsolve* may not be able to find a valid solution.

Nevertheless, when a minimum peak, close but different than zero, is reached and there is sudden change in direction as seen in Figure 5.19, the function might consider that as the final solution, which in all cases is not true. Although these problematics seem nothing alike, and in fact they are, the solution to both problems is the same.

The first step to ensure the validity of the final point and to find new valid points is to change the initial approximation given to the function. The solution given by *fsolve* might be close to zero, but never with the accuracy and precision needed to solve this problem (its order of magnitude may be too high). If we consider the final requirement a vector, then

$$\mathbf{t}_G = \begin{bmatrix} \mathbf{d} \cdot \mathbf{t}_x \\ \mathbf{d} \cdot \mathbf{t}_y \end{bmatrix} \tag{5.51}$$

The solution of this problem is then achieved when the norm of vector $\mathbf{t}_G$ equals zero. Since a numerical approach is used, the cumulative errors do not allow to achieve the exact value of zero as a solution, there is always a slight deviation. Thus, a tolerance value might be considered to indicate whether the solution obtained is acceptable. After some numerical tests, it is suitable to define that a contact point is found when the following condition is verified

$$\|\mathbf{t}_G\| \leq 1 \times 10^{-5} \tag{5.52}$$

If a point does not meet this condition, another approximation will have to be checked. This clashes right out with the first problematic, the multiple contact points. To find multiple contact points, several initial approximations will have to be made, like those delineated in Figure 5.20.
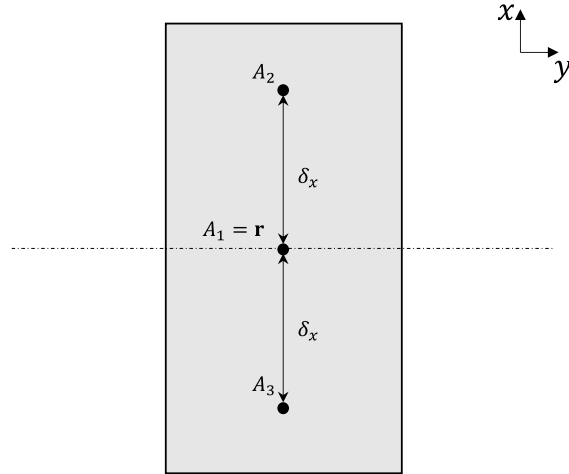
Figure 5.20 - Location of the different approximations in relation to centre of mass of the wheel, $\mathbf{r}$.

The first approximation will always consider the centre of gravity of the wheel. After several trials, it was found that the correct points were always located within

$$\delta_x = \pm\, 0.12 \text{ m} \tag{5.53}$$

from the centre of gravity. With that settled, three initial approximations are now considered.

$$\mathbf{r}^{A_1} = \mathbf{r} \tag{5.54}$$

$$\mathbf{r}^{A_2} = \mathbf{r}^{A_1} + \delta_x \tag{5.55}$$

$$\mathbf{r}^{A_3} = \mathbf{r}^{A_1} - \delta_x \tag{5.56}$$

These three approximations will be evaluated by *fsolve*, which in turn creates three solutions. These solutions will be valid if Eq. (5.52) is met. In the end, one may end up with zero, one, two, or three different solutions.

Many times, solutions from different initial approximations are exactly the same. Other times, these solutions might be so close to each other that they can be considered as the same point. An algorithm to sort which points can be considered the same and which points are different was also created. This can be easily analysed by subtracting one point's coordinates to another's, and calculating the norm of the resulting vector. In that way, if the points are close enough, it might be considered the same point, a tolerance of 10^{-5} m is utilized to verify this issue.

After this process, one gets the points of contact in the xy plane, the same as before. If only one point meets all requirements, then the previous procedure to find its vertical coordinate and to calculate the deflection and real contact point is simply applied. If several contact points exist, then a slightly different process will be used. Note it was said that three points could exist. In fact, this never happens in simulated scenarios, either one gets eliminated or merged with another into a singular point, which makes the next formulation only necessary for the maximum of two coexisting points. Each one of the two points will

receive the same treatment to find its vertical coordinate and deflection. If both points possess a positive value of tire deflection, then both points can be considered as a contact point, like in Figure 5.21.
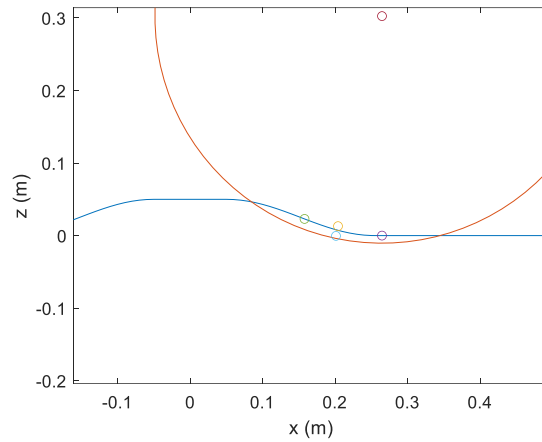
Figure 5.21 - The new contact point will be located between the other two.

However, only one contact point should be studied, the forces will only be applied at a specific point. So, one singular point must be extrapolated from both of those points, with the help of a simple ponderation. In this case

$$\mathbf{r}^{C_P} = \frac{\mathbf{r}^{C_{P1}}\delta_{z1} + \mathbf{r}^{C_{P2}}\delta_{z2}}{2} \tag{5.57}$$

$$\delta_z = \max(\delta_{z1}, \delta_{z2}) \tag{5.58}$$

The previous equations create a new contact point in between the two valid solutions, represented in Figure 5.21, although it will be closer to the one with the biggest deflection. Also, the deflection of the tire at that specific point will always be considered as the largest value. This way a uniform evolution of the contact point across the surface will be guaranteed, with no big jumps from a previous location to the present location. This creates a much better representation of the real contact point.

Abrupt changes in the location, for example at the end of an obstacle, will be avoided, as depicted in Figure 5.22. Sudden large deviations of the location of the contact point can cause large spikes of force to act far away from the previous contact point. In turn, this would create instability, through the extremely fast rise of vertical force in the tire, causing lift off the ground. Apart from the unrealistic evolution of the contact force, its sudden variation may also cause numerical problems, which slow down the integration algorithm. This is due to abrupt variations of the computed accelerations, which largely affects the efficiency of the simulation. In this way, the vertical force is ensured to evolve smoothly, to whichever values it needs to reach. On the other hand, if it is verified that one contact point is not in fact in contact

with the road, by having the deflection equal to zero or negative, the normal procedure, for a single point, is applied. In the end, Eq. (5.50) is again used to calculate the real location of the contact point, P.
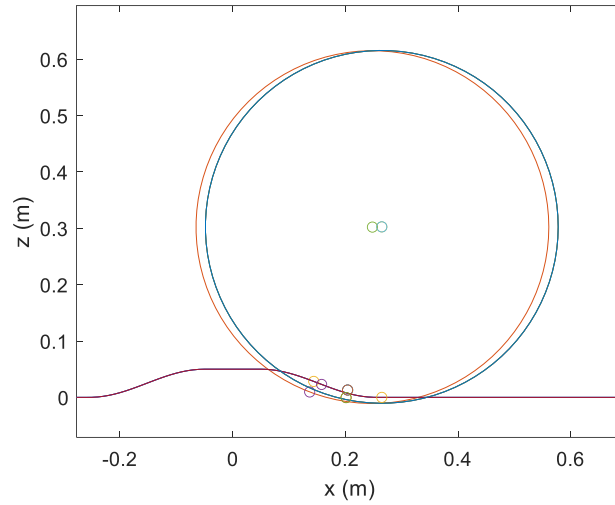
Figure 5.22 - Representation of the position of the wheel in two consecutive timesteps.

The next step would be the computation of the velocity vector, much like in the first method. However, this time the normal vector to the road will be need. This is easily obtained by using the tangential vectors at the contact point. By applying Eq. (5.41) through Eq. (5.46) to point P, it yields

$$\mathbf{n} = \mathbf{t}_x \times \mathbf{t}_y \tag{5.59}$$

The real velocity vector of the wheel will then be given by

$$\mathbf{V}_T = \mathbf{V} - \left[\left(\mathbf{V}^T \left(\frac{\mathbf{n}}{\|\mathbf{n}\|} \right) \right) \left(\frac{\mathbf{n}}{\|\mathbf{n}\|} \right) \right] \tag{5.60}$$

This marks the endpoint of the contact estimation. From now on, every method will be the same for the two contact estimation methods.

5.3.2 Vertical Force

In the previous section, it was shown how to calculate the tire deflection for each contact case, which can be used to calculate the value of the vertical force, at that specific contact point. The vertical force model chosen, given by Eq. (5.2) in section 5.1, will be used. The variables a_1 and a_2 are characteristics of the tire, and therefore already calculated. The last variable $\dot{\delta}_z$ is the variation of the deflection, also known as the deformation velocity. The computation of the deflection's derivate must then be done through the methods presented in the multibody dynamics formulation (chapter 4). Hence, the deflection will be considered as

$$\delta_z = z_{road} - z_{min} \tag{5.61}$$

which is the formulation used to calculate that value for flat roads, and it was said that it does not hold for non-flat roads. While this is completely truth, if one applies the first contact method to the second case, what ends up happening is the creation of a contact point at the lowest vertical coordinate of the tire's profile. Of course, with a changing gradient that lowest point will also change.

The contact point found would always be the projection of the centre of gravity on to the road. In fact, that sometimes is true and is the exact result given by the second method. In other cases that does not occur, and the second method is used. Nevertheless, if one considers that the point calculated by the first method does not have a big deviation from the one gotten by the second, then equation Eq. (5.61) can be used to get the deflection's derivative. Also, it is much easier to derivate that expression since it can be done through the tire's profile (represented through transformations and local systems). The second method only uses road's points, represented in the xyz system, which would be a greater challenge to derivate. Finally, it must be said that the dynamic side of the vertical force is practically negligible. As was stated before, the damping value of a tire is so low (especially in comparison with the suspension's damping) that is does not have any expression in the normal force that is acting at a specific point in time. In the end, this is just used as a mere example on how to calculate this value. The derivative is

$$\dot{\delta}_Z = \dot{z}_{road} - \dot{z}_{min} \tag{5.62}$$

In the flat road method, it was stated that

$$z_{min} = \mathbf{r}^P(3) \tag{5.63}$$

and so

$$\dot{\mathbf{r}}^P(3) = \dot{\mathbf{r}}(3) + \dot{\mathbf{s}}^P(3) \tag{5.64}$$

$$\dot{\mathbf{s}}^P = \begin{bmatrix} 0 & -\omega_z & \omega_y \\ \omega_z & 0 & -\omega_x \\ -\omega_y & \omega_x & 0 \end{bmatrix} \mathbf{A}_m \begin{bmatrix} u_{min} \\ 0 \\ f \end{bmatrix} \tag{5.65}$$

n which the first matrix represents the skew-symmetric matrix of the angular velocity of the body at a specific time step. The plane that is being analysed is different though, in here one is studying the case in the xz plane (z needs to be represented as perpendicular to the length of the contact patch), so that the deformation velocity can in fact be obtained. Then,

$$\dot{\mathbf{r}}(3) = \mathbf{V}(3) \tag{5.66}$$

Since $\dot{z}_{road}$ will be zero (the first method will always be used no matter what),

$$\dot{\delta}_Z = -\mathbf{V}(3) - \dot{\mathbf{s}}^P(3) \tag{5.67}$$

In the end, with Eq. (5.2), the normal force will finally be computed.

5.3.3   Slip Quantities

The next phase in the procedure is the calculation of slip related variables, such as the slip ratio, the slip angle, and the velocities in each different direction.

As is known the wheel does not spin in respect to its original radius. The rotation of the wheel, or the amount of linear distance that one rotation covers, is given by a dynamic radius. Let us recur to Eq. (3.1) and Eq. (3.11). Those will be used to calculate the dynamic radius of the wheel, r_{dyn}. The angular velocity of the wheel in respect to the dynamic radius is

$$\omega_r = \omega_s \times r_{dyn} \tag{5.68}$$

Knowing the linear velocity vector, $\mathbf{V}_T$, it is possible to assess the slip angle of a certain wheel. If the norm of such vector is zero, the slip angle is automatically assumed as zero. If in fact it exists, then the slip angle, α, represented in Figure 5.23, needs to be computed.
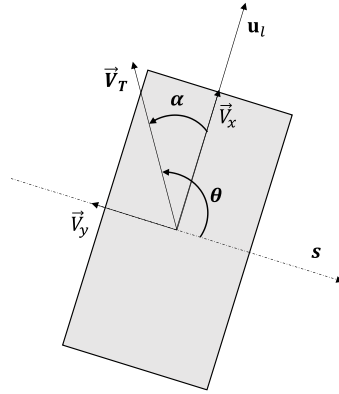
Figure 5.23 - Geometrical definition of the slip angle.

With simple geometry is possible to compute the slip angle at a certain point in time. The dot product between $\mathbf{V}_T$ and $\mathbf{s}$ is given by

$$\mathbf{V}_T\mathbf{s} = \|\mathbf{V}_T\|\|\mathbf{s}\|\cos\left(\theta\right) \tag{5.69}$$

and solving with respect to θ, it yields

$$\theta = \arccos\left(\frac{\mathbf{V}_T\mathbf{s}}{\|\mathbf{V}_T\|}\right) \tag{5.70}$$

The slip angle is simply calculated as

$$\alpha = \theta - 90° \tag{5.71}$$

The linear lateral and longitudinal velocities can now be calculated as

$$V_x = \|\mathbf{V}_T\|\cos(\alpha) \tag{5.72}$$

$$V_y = \|\mathbf{V}_T\|\sin(\alpha) \tag{5.73}$$

Finally, the longitudinal slip, s, will be determined. The longitudinal slip is only dependent on the longitudinal velocity, V_x, and the angular velocity of the wheel, ω_r. If $V_x = 0$ and $\omega_r = 0$

$$s = 0 \tag{5.74}$$

In this case there is no slip because the wheel is not moving. Assuming that V_x is different from zero, two different cases arise.

If $|V_x| > |\omega_r|$,

$$s = \frac{V_x - \omega_r}{V_x} \tag{5.75}$$

Here the wheel's longitudinal velocity is higher than the rotation velocity of the wheel, which means that this specific wheel is braking, and so the longitudinal force will be opposite to direction of movement.

Oppositely, if $|V_x| < |\omega_r|$

$$s = \frac{\omega_r - V_x}{\omega_r} \tag{5.76}$$

The wheel's longitudinal velocity is smaller than the rotation velocity, meaning that the wheel is being "driven", or in other words, an acceleration or positive torque is being applied to the wheel. The longitudinal force will have the same direction as the movement.

5.3.4   Tire Forces

With all the previous quantities at the algorithm's disposal, it is time to compute the remaining forces and torques acting at the contact point:

- Forces: F_x, F_y
- Torques: M_x, M_y, M_z

These values will be obtained through the direct application of the previously chosen tire model, which in this case is the Magic Formula (section 5.1). The forces for the pure slip conditions are always calculated. Then the slip quantities are assessed, and the pure conditions verified. If there is in fact a combined slip situation, only then the combined slip formulas are applied. All formulae can be consulted in Appendix B.

5.3.5   Addition of Forces and Torques

The second to last step of this formulation focusses on adding the calculated forces to the wheel (at the contact point), in order to get the equations of motion for this specific body. The equations of motion

will be solved through a previously chosen method (the augmented Lagrangian), resulting in the accelerations of the body. The solver will then integrate these to obtain the position at the next timestep.
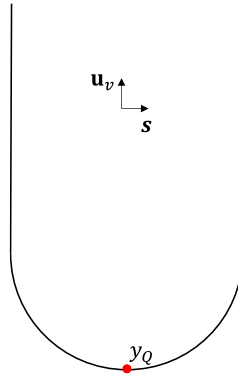
Figure 5.24 - Representation of the point of application of forces on the tire.

Firstly, the point of application of all these forces and torques needs to be calculated. The point known as P, which was thoroughly explained in section 5.3.1, is the representation of the contact point in the xyz system. The real point of application needs to be located at the tire's local coordinate system, $\xi\eta\zeta$ or the fixed $\mathbf{u}_l s \mathbf{u}_v$. The real point of application, depicted in Figure 5.24 is

$$\mathbf{r}^{y_Q} = \mathbf{r}^P - \mathbf{r} \tag{5.77}$$

To add the forces to the body, each force needs to be attributed to the direction in which is acting. Let us create matrices $\mathbf{f}_i$ and $\mathbf{m}_i$

$$\mathbf{f}_i = F_x \mathbf{d}_x + F_y \mathbf{d}_y + F_z \mathbf{d}_z \tag{5.78}$$

$$\mathbf{m}_i = M_x \mathbf{d}_x + M_y \mathbf{d}_y + M_z \mathbf{d}_z \tag{5.79}$$

where each $\mathbf{d}$ vector represents a direction, e.g., $\mathbf{d}_x$ is the vector that gives the longitudinal direction at a certain timestep and so on. For a completely flat surface, these vectors are given by

$$\mathbf{d}_z = \begin{bmatrix} 0 \\ 0 \\ 1 \end{bmatrix} \tag{5.80}$$

$$\mathbf{d}_y = \mathbf{s} \tag{5.81}$$

$$\mathbf{d}_x = \mathbf{d}_y \times \mathbf{d}_z \tag{5.82}$$

Conversely, for a road with obstacles

$$\mathbf{d}_z = \mathbf{n} \tag{5.83}$$

$$\mathbf{d}_y = \frac{\mathbf{s} - \left[\left(\mathbf{s}^T \left(\frac{\mathbf{n}}{\|\mathbf{n}\|} \right) \right) \left(\frac{\mathbf{n}}{\|\mathbf{n}\|} \right) \right]}{\left\| \mathbf{s} - \left[\left(\mathbf{s}^T \left(\frac{\mathbf{n}}{\|\mathbf{n}\|} \right) \right) \left(\frac{\mathbf{n}}{\|\mathbf{n}\|} \right) \right] \right\|} \tag{5.84}$$

$$\mathbf{d}_x = \frac{\mathbf{d}_y \times \mathbf{d}_z}{\|\mathbf{d}_y \times \mathbf{d}_z\|} \tag{5.85}$$

The torques generated by the forces at the contact point can also be given by

$$\mathbf{T} = \mathbf{r}^{yq} \times \mathbf{f}_i \tag{5.86}$$

And so, the end is reached, and all the tire/road contact forces and torques are evaluated and added to the wheel.

5.3.6 Torque Applied Over Time

A normal vehicle is always being affected by the action of the driver. Be it braking or accelerating, it is very unusual to find a car in a zero-slip situation. Of course, it is possible to happen and further in this work some simulations will be done where this situation occurs. However, it is necessary to introduce a "mechanism" that can simulate the actions of both accelerating and braking pedals. Both actions can be viewed as torques working around a wheel's axis.

The acceleration is given to the driven wheels by the driveshaft and differential, which carry the power from the engine. In this work, the vehicle studied will be considered as front wheel drive, which means that only the front wheels receive an acceleration torque. No accelerating torque will be applied to the back wheels. This torque will always have the direction the car is following at a specific moment in time. So, let us define τ_A. This variable represents the acceleration torque given by the engine. This value must be withdrawn from the nominal curves of the engine in study, which can be found in (Zal, s.d.). Nonetheless, this always represents the total value that the engine is giving to two wheels. For each wheel, it yields

$$\tau_{AW} = \frac{\tau_A}{2} \tag{5.87}$$

In this work, the accelerating torque will always be the same for each wheel, meaning it needs to be divided by two.

As for the braking torque, a braking bias of 50/50 % was considered. This suggests that the braking in the front is the same as in the back wheels or, in other words, all wheels will be under the same braking torque. To define this torque, it is necessary to know the initial and final velocities and the time interval in which the brakes will be acting. A deceleration is given by

$$d = \frac{V_f - V_i}{\Delta t} \tag{5.88}$$

The braking force is calculated as

$$F_B = m_c d \tag{5.89}$$

Remember that m_c represents the total mass of the car. For each wheel,

$$\tau_W = \frac{F_B}{4} r_0 \tag{5.90}$$

Both torques are then applied for a certain time frame (the braking torque obviously for Δt seconds). This works as a simple simulation of the actuation of a pedal for a certain amount of time.

5.3.7   Road Profile

In this work, to simulate a car negotiating a certain road, it is necessary to design that road's profile in all 3 directions, xyz. As has been stated, two types of surfaces were considered: the flat road and the one with obstacles, both demonstrated in Figure 5.25.
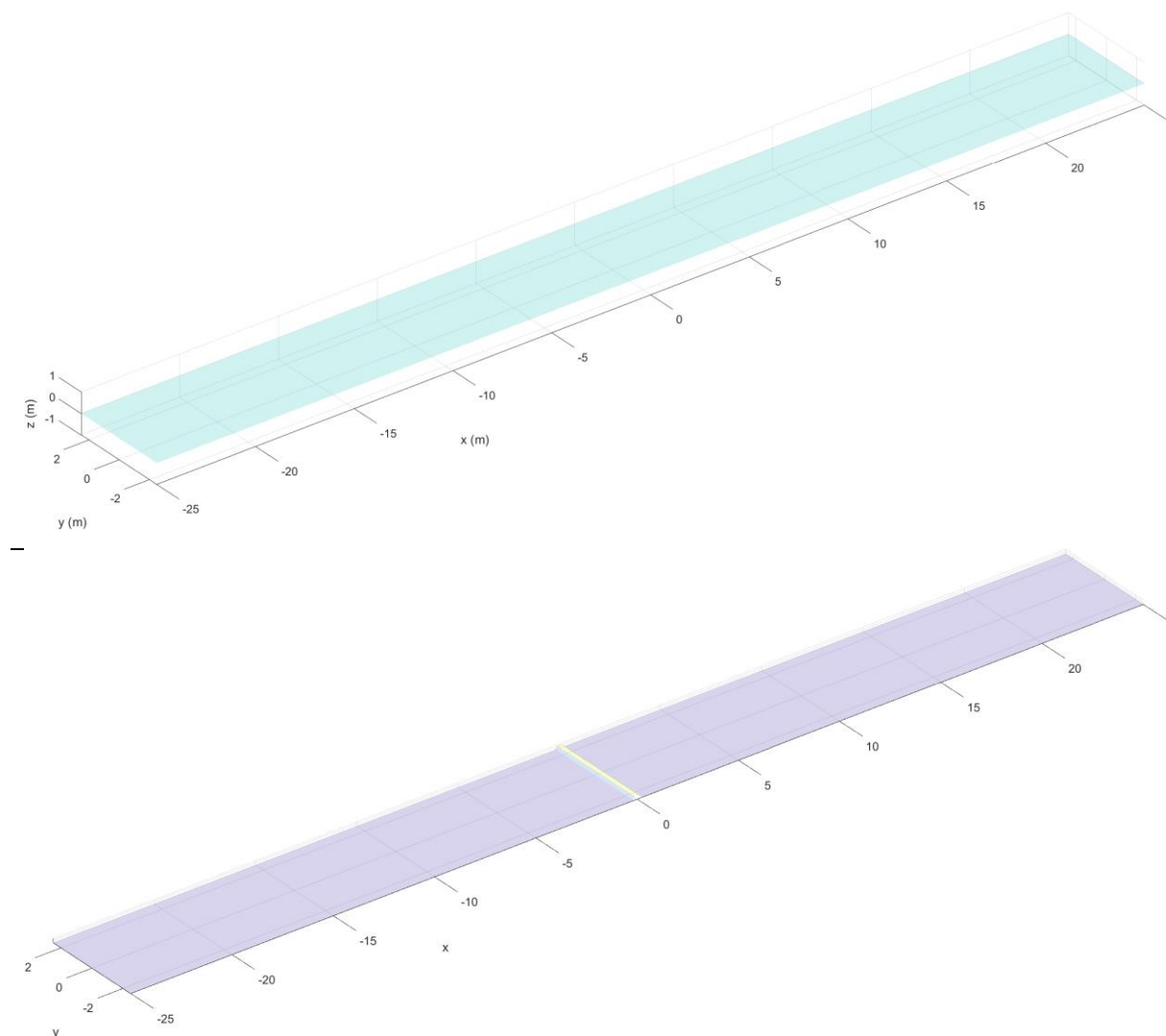
Figure 5.25 - The two types of roads. On top, the flat road. Below, an example of a road with a bump.

For a totally flat road, it is known that its height is invariable, at $z = 0$, and so length, width and height are defined as

$$x = \left[-\frac{L}{2}, \frac{L}{2}\right] \text{ (length)} \tag{5.91}$$

$$y = \left[-\frac{W}{2}, \frac{W}{2}\right] \text{ (width)} \tag{5.92}$$

Conversely, for a road with obstacles, while the flat area can also be defined by having the vertical coordinate equal to zero, the obstacle needs another approach. The obstacles can be of two types:

- Bumps: a protuberance on a level surface, represented in Figure 5.26
- Potholes: a hollow or depression in the ground, portrayed in Figure 5.27
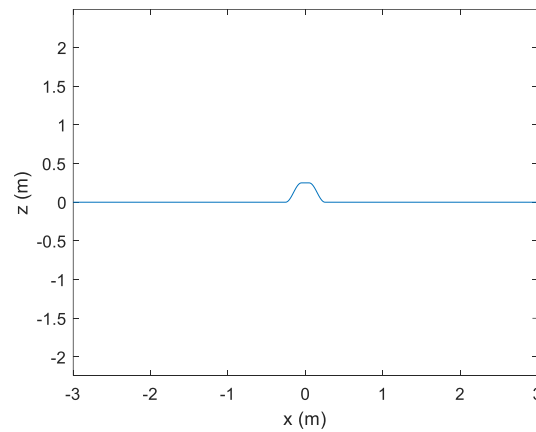
Figure 5.26 - Example of road with a bump.

The obstacles are defined by a mathematical expression, valid for both potholes and bumps. This formula was adapted from (Rill & Castro, 2020). For a bump

$$z_{\text{bump}} = \frac{1}{2}H\left[1 + \cos\left(2\pi\left(\frac{x + d/2}{L_b}\right)\right)\right] \tag{5.93}$$

For x that ranges from $-\frac{L_b}{2}$ to $\frac{L_b}{2}$, where L_b is the total length of the bump, the previous expression, Eq. (5.93), can be used to create a speed bump. H is the desired height of the bump and d the length of that flat area on the bump's top. This gives an accurate representation of a real speed bump.
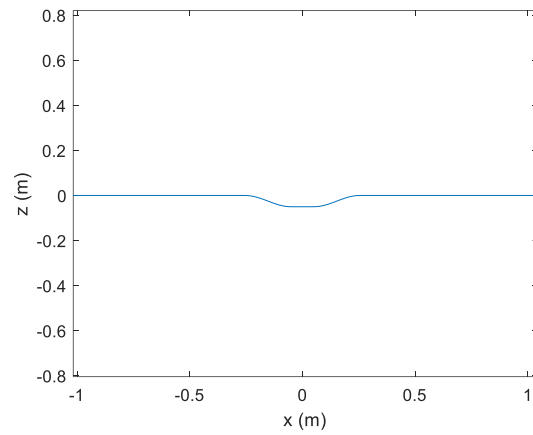
Figure 5.27 - Example of a road with a pothole.

For a pothole, the expression yields

$$z_{\text{pothole}} = -\frac{1}{2} H \left[1 + \cos\left(2\pi \left(\frac{x + d/2}{L_b} \right) \right) \right] \tag{5.94}$$

Eq. (5.94) is the symmetric of Eq. (5.93).

6. CASE STUDY

In this chapter, the methodologies presented are tested, to simulate a car negotiating a small road. Firstly, a proof of concept is done using an entirely flat road, with no obstacles. This is of extreme importance, especially to identify errors and bugs in the general code. Also, it helps the analysation of the tire model, also known as force model.

Secondly, roads with obstacles are simulated. These are particularly preponderant for the refinement of some of the solver's properties, such as its type and tolerances it uses to find the best solutions. This will permit the creation of a fast simulation, capable of delivering good results. Lastly, some simulations with different obstacles will be performed and their results evaluated.

6.1   Vehicle Model

This work is created within the scope of studying and analysing the performance of suspension systems for vehicles travelling roads with different surface conditions. It was necessary to define a vehicle model, with its important components, to study and compare results. An important work of reference to this study was (Ambrósio & Verissimo, 2009).

Figure 6.1 - Example of a small family car. Adapted from (Volante website, s.d.).

In (Ambrósio & Verissimo, 2009), a "small family car", such as the one in Figure 6.1, undergoes a multibody dynamic analysis. The exact same model will be used in this study, so all properties and components were withdrawn from that article. The car's properties, such as its mass important dimensions are discussed in Table 6.1.

Table 6.1 - Some properties of the vehicle studied (Ambrósio & Verissimo, 2009; Zal, s.d.).

Vehicle Properties	
Mass	1238.4 kg
Wheelbase	2.47 m
Width	1.41 m
Drive	Front Wheel Drive
Front Suspension	Independent – Macpherson strut
Rear Suspension	Semi-independent – Torsion bar

The multibody model of this vehicle, represented in Figure 6.2, considers mainly the suspension system of front and rear wheels, depicted in Figure 6.3. In fact, it is a quite simple model made of a chassis, four wheels and both suspension systems. No other components were modelled, as they are deemed unnecessary to study the behaviour of a car's suspensions. Systems like the engine or the drivetrain are purely unevaluated.
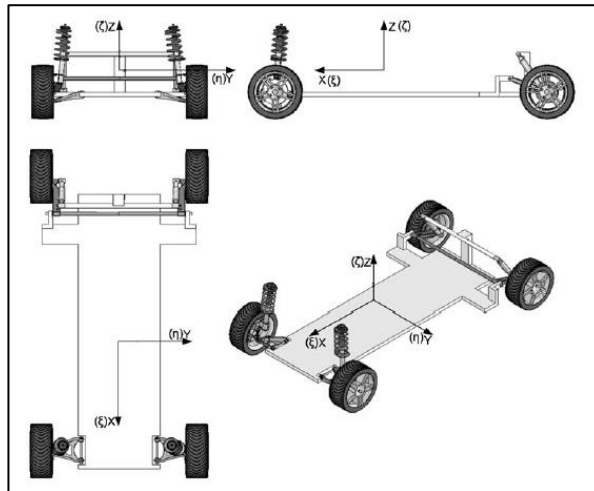
Figure 6.2 - Generic model used. Adapted from (Ambrósio & Verissimo, 2009).
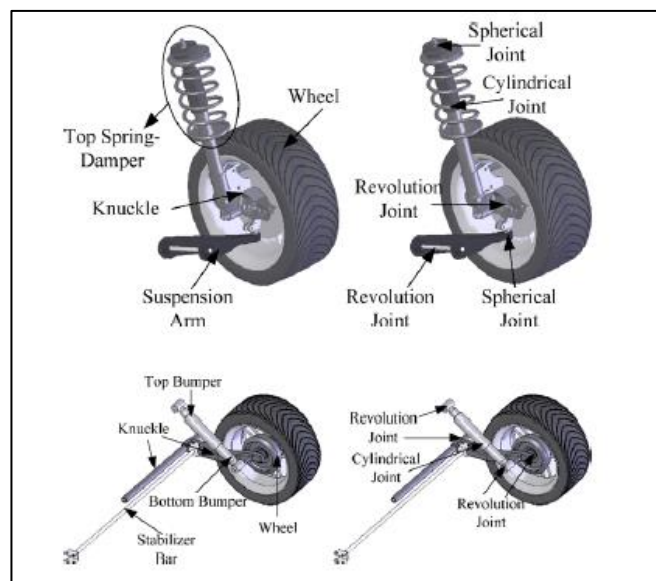
Figure 6.3 - Model of both suspensions systems. On top, the front suspension. Below, the rear suspension. Adapted from (Ambrósio & Verissimo, 2009).

The front suspension is also known as a Macpherson strut, which is a type of independent suspension (see section 2.2). Since it is independent, then a strut exists in each one of the front wheels. This type of suspension is characterized by the telescopic arm suspension arm, that is responsible for the control of the wheel's position. This arm allows a connection between the knuckle, or steering rod, and the vehicle's

chassis. The Macpherson suspension is compact, and very popular in small vehicle. The rear suspension is also known as a torsion bar, which is of the semi-independent kind of suspension. Nowadays, this system is not that common in modern cars, especially with the use of multi-link suspensions, but since this model possesses it, it will be studied.

Table 6.2 and Table 6.3 are used to define the vehicle as a multibody system. The reference systems, xyz and $\xi\eta\zeta$, have their origin placed in the same spot, the chassis' centre of mass. Each centre of mass is the origin for a component's local reference system, $\xi\eta\zeta$. Note that only components of the left-hand side of the vehicle are exemplified in the tables. All right-hand side components are symmetrically defined, in relation to the y axis. This is directly applied to the centre of mass, but for the Euler parameters the method does not rely on simple symmetric transformations. To obtain the Euler parameters of the right-hand side components, a formulation was used and is presented in Appendix A.

Table 6.2 - Description of the right-hand side of the model and some inertial properties (Ambrósio & Verissimo, 2009).

	Body	Description	Mass (kg)	Inertia (kg/m^2) $\xi\xi/\eta\eta/\zeta\zeta$
	1	Chassis	1090	1000/2130/2200
	2	Left Suspension arm	1.976	0.0022/0.0100/0.029
Front	3	Left Knuckle	8.897	0.158/0.155/0.048
	4	Left Top Spring-Damper	3.382	0.030/0.030/0.008
	5	Left Wheel	19.229	0.301/0.496/0.301
	10	Left Suspension arm	10.286	0.277/0.155/0.429
Rear	11	Left Bottom Damper	2.640	0.001/0.011/0.011
	12	Left Top Damper	2.174	0.001/0.016/0.016
	13	Left Wheel	25.638	0.324/0.522/0.324

As it is possible to conclude through the observation of Table 6.3 and Figure 6.2, the centre of mass of the chassis coincides with the origin of the vertical axis, z. In previous chapters, it was stated that the height of a certain road's profile starts at $z = 0$, for all simulations the road that vertical coordinate will always represent the flat area of the road. Thus, if both the previous coordinates coincide, that would mean that the chassis is intertwined with the flat surface, and the wheels for example would not be crossing the road, but something underneath it. This needs to be corrected, so that the wheels' lowest point can touch the road at $z = 0$. Additionally, the static deflection of the tires needs to be accommodated and guaranteed by positioning the vehicle at the correct location, so that in the beginning

of the simulation the deflection is somewhat stable. A correction to the centre of mass of each component was, hence, made and is depicted in Figure 6.4 and Figure 6.5.

Table 6.3 - Centre of mass and Euler parameters of the right-hand side bodies.

	Body	Centre of mass $(x/y/z)_0$	Euler parameters (e_0, e_1, e_2, e_3)
	1	0.0000/0.0000/0.0000	1/0.0000/0.0000/0.0000
	2	0.9815/-0.4791/-0.2538	1/0.0000/0.0000/0.0000
Front	3	1.0092/-0.6138/-0.1071	0.9981/-0.0443/-0.0436/-0.0019
	4	0.9470/-0.5080/0.2757	0.9981/-0.0443/-0.0436/-0.0019
	5	0.9879/-0.7042/-0.1974	1/0.0000/0.0000/0.0000
	10	-1.2587/-0.4906/-0.1161	0.9848/0.0000/-0.1736/0.0000
Rear	11	-1.3907/-0.5141/-0.1070	0.8829/0.0000/-0.4695/0.0000
	12	-1.2765/-0.5141/0.0624	0.8829/0.0000/-0.4695/0.0000
	13	-1.4821/-0.6937/-0.1974	1/0.0000/0.0000/0.0000
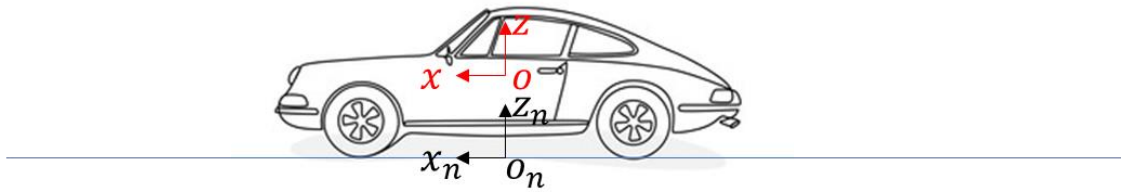
Figure 6.4 - Representation of the correction to the centre of mass.

The transformation needed is simply a vertical shift of the origin of the xyz system Figure 6.4. For any given point, k, in this multibody system

$$\mathbf{r}_{in}^k = \mathbf{r}_{i0}^k + \begin{bmatrix} 0 \\ 0 \\ z_c \end{bmatrix}$$

(6.1)

where

$$z_c = 0.1974 + r_0 - \delta_{z0}$$

(6.2)

The first member of Eq. (6.2) is simply the vertical coordinate of the wheel's centre of mass, which is the same for all four wheels.
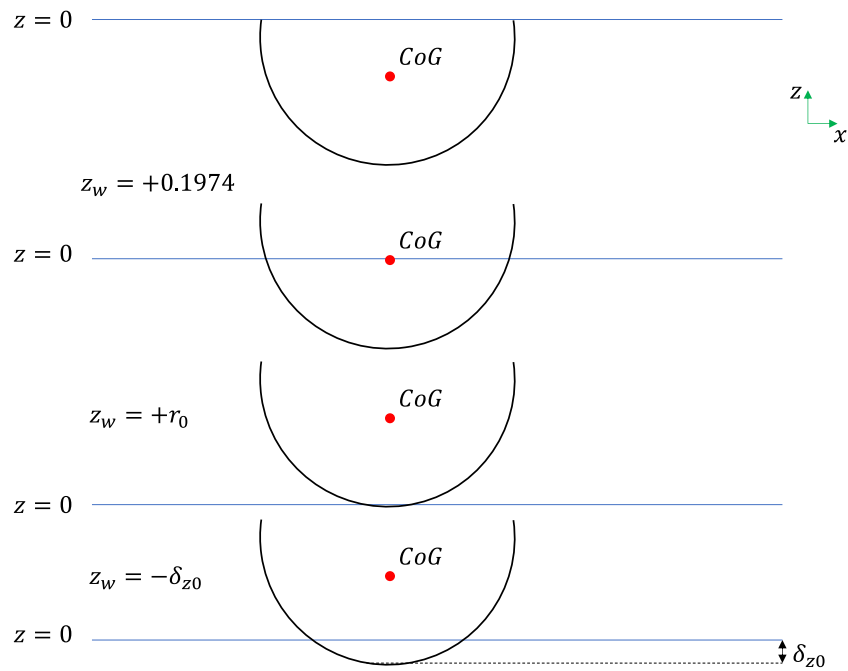
Figure 6.5 - Sequence of changes to the position of the wheel.

Figure 6.5 represents the sequence used to create the vertical shift. Instead of coinciding with the chassis, the origin of the xyz system now clashes with the road's base vertical coordinate, $z = 0$. This way the vehicle will stabilize towards the proper values of deflection when starting the simulation.
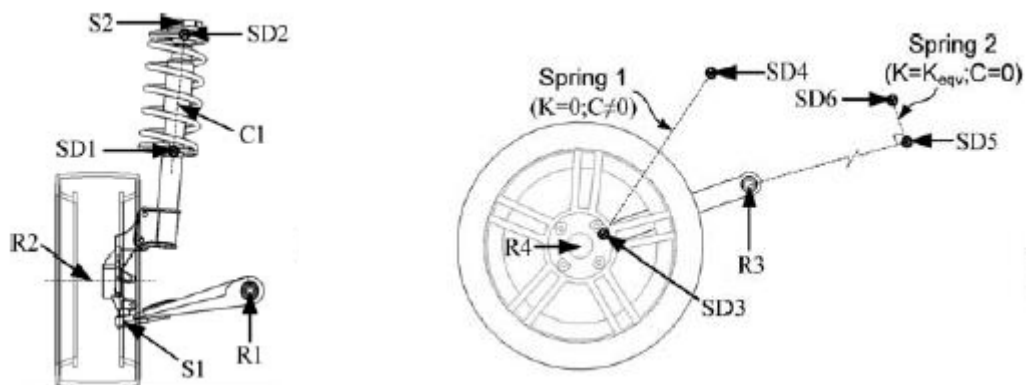
Figure 6.6 - Kinematic joints for the front suspension (left) and the rear suspension (right). Adapted from (Ambrósio & Verissimo, 2009).

Table 6.4 gives the location of all kinematic joints that connect the vehicle's left-hand side components. The right-hand side is symmetric relative to the η axis. Referring to Table 4.1, the total number of constraints can be calculated. For the left-hand side the total number of constraints is 44. Since the right-hand side is exactly equal to the left one, then the total number of constraints acting on the multibody system is 88. To this final number, another two constraints must be added, that are respectful to a fictious joint created to simulate the steering axle. This joint restrains the front wheels to the point where both

axles must always be parallel. The only constraint is the rotation around the vertical axis. So, in fact, the total number of constraints is 88.

Table 6.4 - Definition of the kinematic joints for the left-hand side of the vehicle (Ambrósio & Verissimo, 2009).

ID	Joint type	Body i	Body j	ξ_i^P $s_{\xi i}$	η_i^P $s_{\eta i}$	ζ_i^P $s_{\zeta i}$	ξ_j^P $s_{\xi j}$	η_j^P $s_{\eta j}$	ζ_j^P $s_{\zeta j}$
1	Sph	1	4	0.9363 –	–0.4870 –	0.3980 –	0.0000 –	0.0000 –	0.1233 –
3	Sph	2	3	0.0140 –	–0.1589 –	–0.0307 –	–0.0291 –	–0.0086 –	–0.1770 –
5	Rev	1	2	0.8628 0.2310	–0.3423 0.0000	–0.2200 0.0000	–0.1187 –0.2310	0.1368 0.0000	0.0000 0.0000
7	Rev	3	5	–0.0291 0.0000	–0.0323 –0.0348	–0.0913 0.0031	0.0000 0.0000	0.0502 0.0350	0.0000 0.0000
9	Rev	10	11	–0.1949 0.0000	0.0065 0.0600	0.0000 0.0000	–0.0913 0.0000	0.0300 0.0600	0.0000 0.0000
11	Rev	1	12	–1.2181 0.0000	–0.5441 –0.0600	0.1489 0.0000	0.1043 0.0000	–0.0300 –0.0600	0.0000 0.0000
13	Rev	1	10	–1.1466 0.0000	–0.5291 0.1065	–0.0753 0.0000	0.1193 0.0000	–0.0385 0.1065	0.0000 0.0000
15	Rev	10	13	–0.2377 0.0000	–0.2095 –0.0590	0.0000 0.0000	0.0000 0.0000	–0.0064 –0.0590	0.0000 0.0000
17	Cyl	3	4	–0.0286 0.0000	0.0711 0.0000	0.2799 –0.0780	0.0000 0.0000	0.0000 0.0000	–0.1147 –0.0780
19	Cyl	11	12	0.0412 –0.0675	0.0000 0.0000	0.0000 0.0000	–0.1632 –0.0675	0.0000 0.0000	0.0000 0.0000

With all the kinematic joints defined, by a point, P, and a vector $\mathbf{s}$, it is time to add the point-to-point forces, or the spring-damper actuators, as seen in Table 6.5. The front suspension, being a Macpherson strut, has a spring-damper as its main suspension provider. The back suspension relies more on the stiffness of its arm and damping of the pair bottom/top damper.

Table 6.5 - Force-elements data for the right-hand side of the vehicle (Ambrósio & Verissimo, 2009).

Bodies (i, j)	Coordinates on bodies (i/j)	Spring stiffness (N/m)	Damping (Ns/m)	Undeformed length L_0 (m)
(3, 4)	(–0.029, 0.071, 0.213) (0.000, 0.000, 0.094)	59190	7919	0.33
(11, 12)	(–0.091, 0.000, 0.000) (0.104, 0.000, 0.000)	–	15000	–
(1, 10)	(–0.275, –0.562, 0.455) (1.119, -0.071, 0)	14530	–	0.115

6.2   The Tire

According to (Ambrósio & Verissimo, 2009) and (Pacejka, 2002) it was possible to reconstitute a tire that respects both the Magic Formula parameters and the characteristics of the one used in (Ambrósio & Verissimo, 2009). The tire constructive characteristics can be found in Table 6.6, while its profile is depicted in Figure 6.7.

Table 6.6 - Constructive characteristics of the tire used.

Tire Characteristics	
Nominal Radius (m)	0.313
Width (m)	0.209
Radial Stiffness (kN/m)	200
Longitudinal Stiffness (kN/m)	500
Lateral Stiffness (kN/m)	150
Cornering Stiffness (kN/m)	30
Rolling Friction Coefficient	0.01
Radial Damping (Ns/m)	0.078
Camber (°)	-2.5

Finally, the static deflection for the tire must be calculated. Applying a vertical force equal to the weight of the vehicle to Eq. (5.16), the static, or initial, deflection of the tires can be computed. The value obtained was 0.0157 m for all wheels.

(a)

(b)
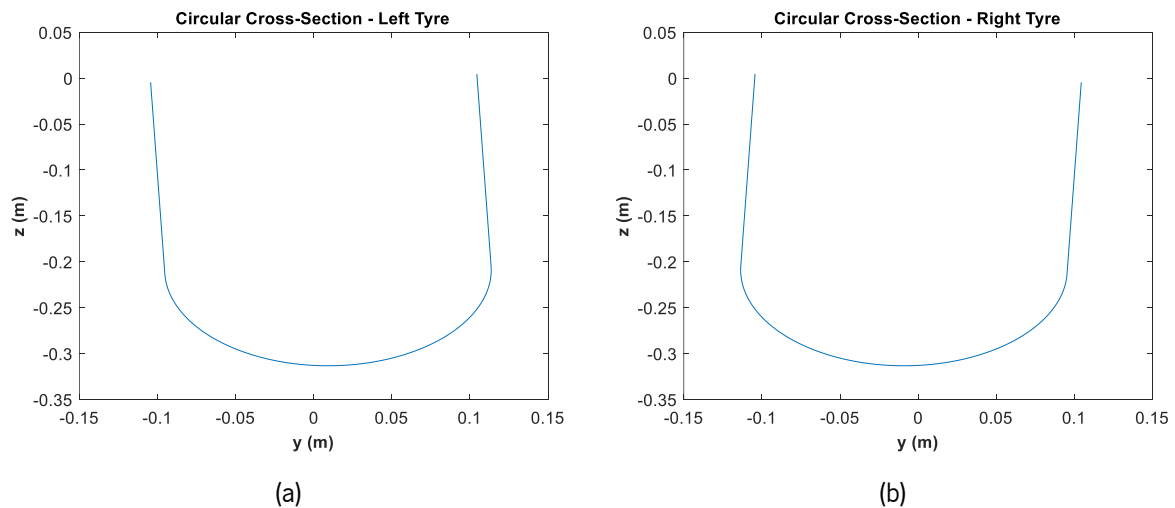
Figure 6.7 – (a) Cross-section of the left-hand side tire. (b) Cross section of the right-hand side tire

6.3   Flat Road Simulations

The validity of a model should always be proven by testing simpler cases. These cases help to verify the existence of problems within the simulator, without spending too much processing power and time.

The objective of this work is to study the suspension's parameter, especially how they react when going over an obstacle. But first, the model and the methodology created before must be tested in order to prove that the simulator generally works. This means that in this group of tests, the general multibody simulation algorithm will be tested alongside the assessment of the basic performance of the integrator and, finally, the elements regarding the tire force model.

The first batch of simulations were done with a purely flat road, like that depicted in Figure 6.8. Regarding this, only the first method of contact estimation was used, so that these are fast and not very demanding simulations. The position of the car across time will be verified, as well as the variation of the deflection of the wheels and the response of the longitudinal force to braking and accelerating torques.
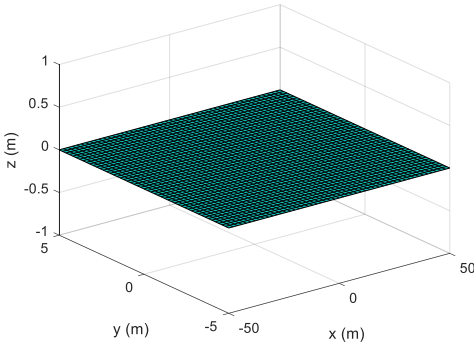
Figure 6.8 - Example of a flat road, with 100 m of length and 10 m of width.

All simulations, that will be presented next, used the solver ode45, with both relative and absolute tolerances equal to 10^{-5}. The solver will in fact be refined afterwards, with the help of roads with obstacles. To evaluate the previously mentioned variables, only one wheel will be used, the front left wheel. Since the car will have no steering input, it will only move forward, along the longitudinal axis, x, which creates a uniform response across all wheels, hence not needing to evaluate all wheels. In Table 6.7, some general simulation conditions will be presented.

Table 6.7 - Initial conditions for the simulation.

Initial Conditions	
Road Material	Dry asphalt
μ	0.9
V_0	16.667 m/s
ω_0	V_0/r_0 rad/s
L_{road}	100 m
W_{road}	10 m
t_f	5 s
x_i	-44.021 m
δ_{z0}	0.0157 m
Solver	Ode45

6.3.1 Simulation 1

The first simulations consisted in applying the initial conditions referenced in Table 6.7 and check the final result. This is particularly important to evaluate all the algorithms and check whether there are meaningful constraints violations happening.

The car starts with the initial velocity of 60 km/h. Each wheel is given the same rotation, that is the initial velocity divided by the wheel's radius. The wheels are in a free-rolling state, where the slip is close to null. Also, no steering inputs are added, which means that the car strictly follows a straight line. No external torques will be added, and in the initial state the car acts as if dropped to the ground, which makes it not start immediately with the expected deflection. It must be said that the car is kept "running" for 5 seconds, which indicates the end of the simulation. All posterior results of this particular simulation are given for a single wheel, precisely the front-left wheel. The following table shows some of the obtained results.

Table 6.8 - Some considerations at the end of the simulation.

Final state	
V_f	16.287 m/s
x_f	38.347 m
δ_{zf}	0.0185 m
Duration	$\approx$ 17 min
Number of evaluations	13993

The first thing to check is whether the wheel is moving or not. This is mainly made by analysing the variation of its centre of mass, more specifically the longitudinal coordinate, x. As can be seen in Figure 6.9, the x coordinate of the wheel's centre of mass is evolving linearly against time, which means that

the wheel is moving. The right-hand side of that figure shows the evaluate of the wheel's forward velocity trough time. It is diminishing so gradually to the point it can be considered constant over time, which was expected, since it is rolling freely on a surface. Nevertheless, the slight decrease is due to the loss of energy caused by dissipative effects.

(a) (b)
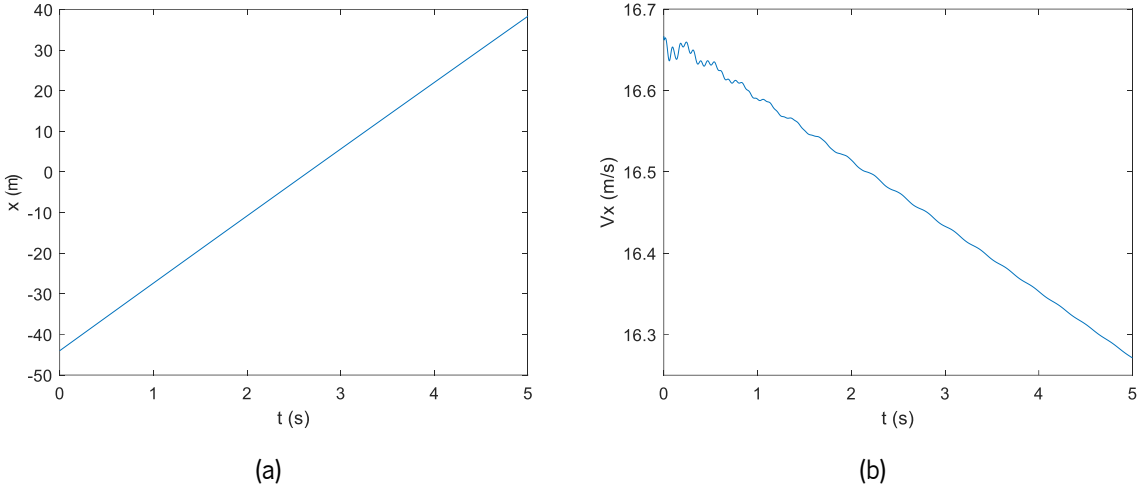
Figure 6.9 – (a) Variation of the position of the wheel with time; (b) Variation of the forward velocity.

Figure 6.10 shows the time history of both tire deflection and vertical for the front left wheel. The results for the rest of the wheels are similar. As can be seen, the wheel, after the initial state (where $t = 0$ s), suffers a big shift in vertical displacement. This is because wheel is being dropped, so there will always be a sort of rebounding behaviour, especially in the beginning where it is bigger. This creates an oscillatory, although small, evolution of these parameters. The wheel is in fact in a transient state, and, as time goes on, starts to tend to a steady state, where the two variables reach a uniform and constant value. However, for the deflection, its value does not correspond to that given by the static results, shown in Table 6.7. This is simply due to the car's centre of mass, represented by the chassis, being closer to the front wheels than to the rear ones (refer to Figure 6.2 and Table 6.3). The weight of the car is distributed more towards the front (the car has its engine at the front), so the force being applied to the front wheels is, consequently, higher and, therefore, they should present a bigger deflection. The rear of the car has the opposite behaviour, by which a smaller deflection is reached ($\delta_{zf} = 0.0130$ m).

(a)   (b)
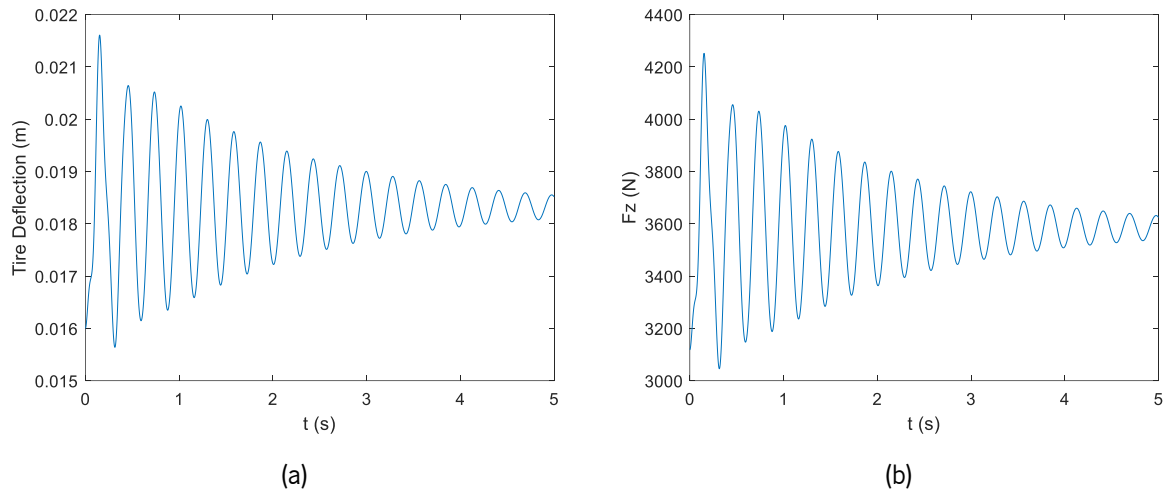
Figure 6.10 – (a) Variation of the tire deflection. (b) Vertical force for the left-hand side front wheel.

The final checkpoint is to see whether there are constraints at the position level being violated in the multibody system. Figure 6.11 represents exactly that and as is seen there are no meaningful violations of constraints acting on the system. That initial drop is due to the initial correction of positions made by the simulator, after that this value becomes zero, meaning that all joints and bodies are well positioned and connected, and that the simulator does not need to change the bodies' positions to obtain good results.
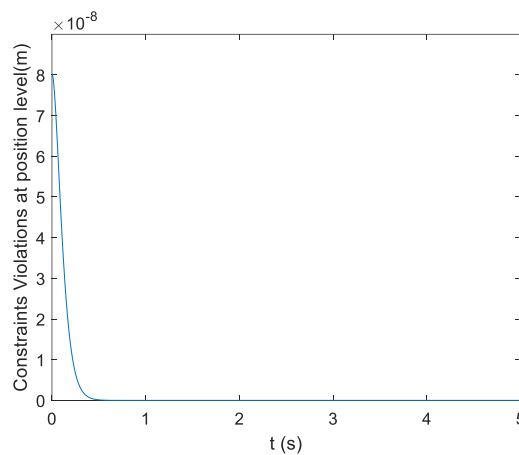
Figure 6.11 - Graphic of the constraints violation for the multibody system.

6.3.2   Simulation 2

Knowing that the simulation is working accordingly, the second flat ground simulation was made to see whether the "drivetrain" and braking system algorithms work. The same basis of simulation, as the previous one, was kept, but two different external torques were added. Some results are represented in Table 6.9.

106

Table 6.9 - Some measured variables for flat simulation 2.

Flat Simulation 2	
$V_{2.5s}$	18.000 m/s
V_f	11.600 m/s
x_f	32.69 m
δ_{zf}	0.0185 m
Duration	$\approx$ 17 min
Number of evaluations	14281

In this simulation two different torques were added. Firstly, an acceleration torque and then a braking torque. The acceleration torque was added for 2 s, while the other one lasted 2.5 s. So,

$$0.5 \leq t \leq 2.5 \text{ (s)} \rightarrow \tau_a = 0.5 \times 150 \text{ (Nm)} \tag{6.3}$$

$$t > 2.5 \text{ s} \rightarrow \tau_b = -270 \text{ Nm} \tag{6.4}$$

The acceleration torque was applied to the front wheels only, with a total magnitude of 150 Nm that is evenly distributed on both wheels. This value is purely theoretical. By analysing (Zal, s.d.) (the torque/speed curves), the engine cannot provide this kind of torque, it is too big. However, since this is just a test to check the algorithm, it can be considered, especially because the raise in velocity is much faster than if a lower value was applied. The braking torque is the same for every wheel.

Figure 6.12 is the representation of the variation of the longitudinal force against time. It can be concluded that the algorithm used is indeed working, the longitudinal force is increasing or decreasing depending on which torque is applied. But several points arise from this graph.
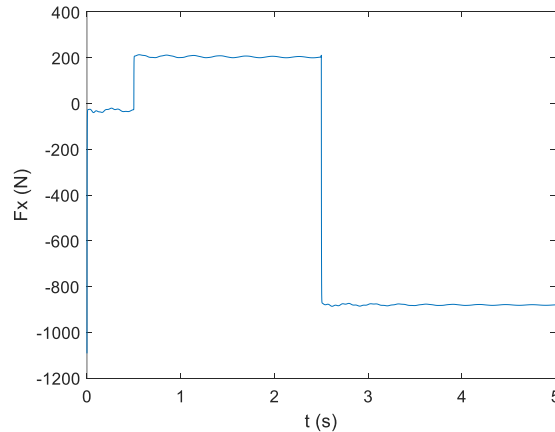
Figure 6.12 - Variation of the front-left wheel's longitudinal force.

First, the longitudinal force does not start at zero, when $t = 0$ s, but at around $F_x = -1050$ N. This happens because to calculate this force, the dynamic radius is used, r_{dyn}, that is different from the nominal radius. The initial rotation of wheel is given by its nominal radius, but the real velocity is given by

the dynamic radius. So, using the latter one, the velocity of rotation of the wheel will be different from the one given initially. The linear velocity and rotation velocity will then be different, creating a slip in the initial state of simulation. The new rotation velocity will be smaller than the one introduced as the body velocity. The last one uses the nominal radius, which is always bigger than the dynamic radius, and, in the end, will always be bigger than the new rotation velocity. The slip created will then form a negative longitudinal force, acting as a sort of brake for the wheels in the initial state. However, this lasts only a moment, since the simulation corrects itself almost instantaneously, converging when the rotation velocity and forward velocity of the wheel are almost identical (the slip becoming zero).

The second point would be located at $t = 0.5$ s, which marks the beginning of the application of the acceleration torque. From this point until $t = 2.5$ s, the longitudinal force is positive, and has a magnitude of around 200 N. This assures that the acceleration torque increases the rotation velocity of the car, as depicted in Figure 6.13, creating a positive slip, and therefore guaranteeing that the algorithm for this pedal is working.

As seen by Figure 6.13, while the rotation velocity increases, the linear velocity also increases almost proportionally. This, in fact, steadies the difference between the two, thus not creating a big slip value. It stays around 0.2%.

(a)   (b)
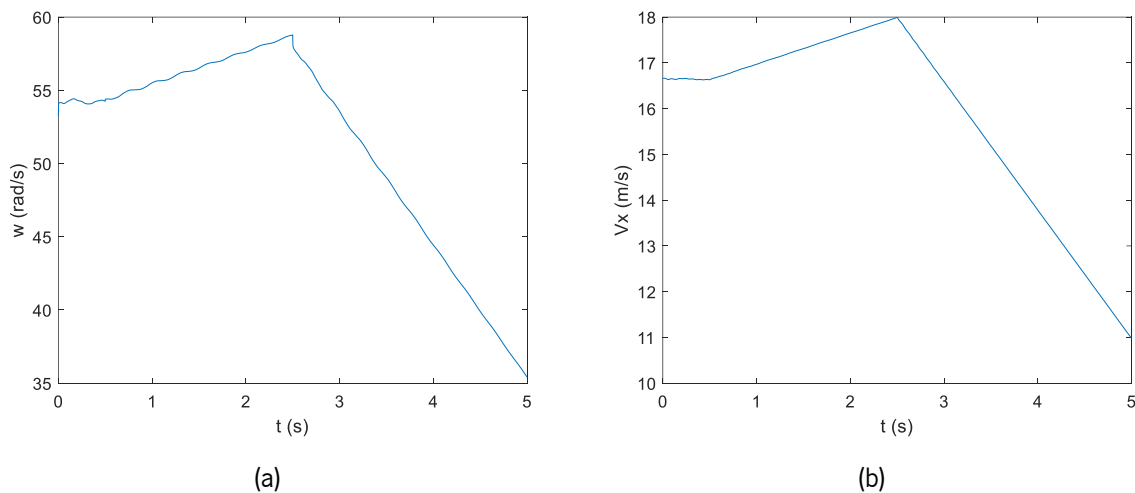
Figure 6.13 - Variation of both angular velocity (a) and linear velocity (b) of the studied wheel.

The third point is located at $t = 2.5$ s and represents the actuation of the braking pedal. Figure 6.12 and Figure 6.14 shows that everything is running smoothly, since the longitudinal force decreases substantial to negative values, which shows that a braking slip is happening on the tire. Finally, it can be concluded that a tire model used, the Magic Formula, is, indeed, a steady-state model. The variations in longitudinal force happen instantaneously at the exact time the torque is applied; no lag is verified.
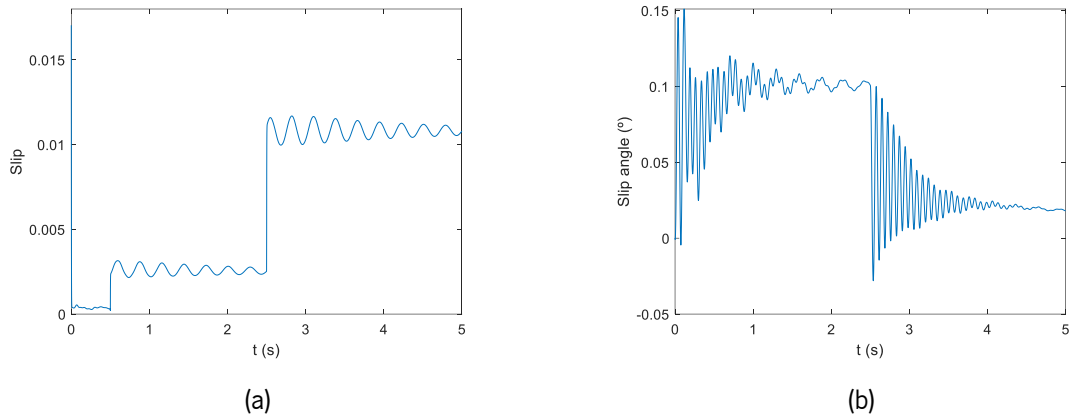
Figure 6.14 - Variation of the slip (a) and slip angle (b) for the front-left wheel.

Additionally, it was possible to evaluate the slip angle of the front-left wheel over time. As can be seen in Figure 6.14, there is always the slightest of slip angles. Much like the deflection, it first starts at a transient state that evolves into a final value, of $0.02°$. The car is supposed to be moving on a completely straight line, so it was expectable that this value would be zero. Nonetheless, the values obtained for this variable are extremely small, especially being an angle. An angle of $0.15°$ does not pose a significant expression to alter the straight-line motion of the wheel. Therefore, it is concluded that this value is purely a numerical error made by MATLAB. Figure 6.15 corroborates this, showing that the evolution of the lateral force, generated by the slip angle, is insignificant, possessing magnitudes of around 15 N in steady state.
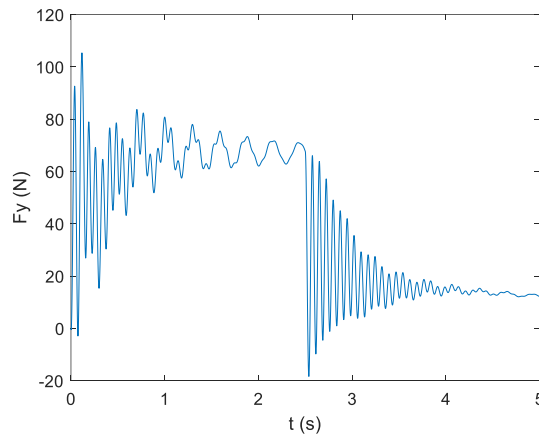
Figure 6.15 - Variation of the lateral force with time.

Finally, it is possible to conclude that the multibody system created is functional and that the behaviour is what was expected.

6.4   Refinement of the Solver

The previous simulations were done to prove some concepts innate to the algorithms created for this work. All of them were done using the same solver, the ode45, with a tolerance of 10^{-5}. The final time of computer processing was around 17 minutes, which is acceptable for a 5 s simulation. However, using the second method of contact estimation, created specifically for roads with obstacles, the simulation time for a flat road increased massively to 50 minutes, on a 2 s simulation. It is then possible to state that with an obstacle this processing time would increase even more. To guarantee a good processing time, while the accuracy of results, a refinement to the solver must be done.

In section 5.2, it was seen that there are several types of integrators, provided by MATLAB. These integrators can be used in detriment of the others, if any do not provide efficient results. Also, their tolerances, used to check and accept final results, can be changed, which can improve the efficiency of the simulation. Considering what was said before, a refinement to the solver was made, which consisted of always running the same simulation for a different integrator, using the same tolerances, and checking whether the results provided deviated from the mean values of all the simulations. In the end, with the optimal integrator chosen, the tolerances for that specific solver were evaluated and the one which guaranteed the most optimal results was chosen. The solver chosen for these tests where the nonstiff ones: ode45, ode23, and ode113. The stiff ones were also tested, but the results took too much time to be acquired (over 24 hours). This showed that this is not a stiff problem (Choose an ODE Solver, s.d.), not needing a very fine timestep to be evaluated.
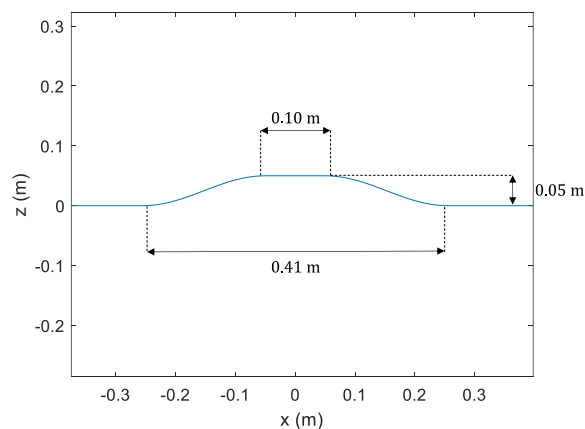
Figure 6.16 - Dimensions of the bump used for this simulation.

The surface chosen to test the solvers was a 50 m asphalt road, with a small speed bump in the middle, illustrated in Figure 6.16. The speed bump has the same width as the road. The car is supposed to be dropped off in a free-rolling state, such as in the flat ground simulations, without adding any

acceleration or braking torques. No steering input was made. The conditions for these tests can be seen on Table 6.10.

Table 6.10 - Initial conditions for the solver refinement simulations.

Initial conditions	
Road Material	Dry asphalt
μ	0.9
V_0	16.667 m/s
ω_0	$\dfrac{V_0}{r_0}$ rad/s
L_{road}	50 m
W_{road}	5 m
t_f	2 s
x_i	-21.012 m
δ_{z0}	0.0157 m

To evaluate the performance of each solver, some variables were chosen:

- Chassis' vertical coordinate over time, $z_{chassis}$
- Deflection of the front-left wheel (Maximum, Minimum and Mean), δ_z
- Vertical force on the front-left wheel
- Mechanical energy of the system, E_m
- Time of the simulation, Time

Table 6.11 shows the results obtained. As can be easily seen, ode113 is the faster, while ode45 the slower of the solvers. In fact, for this specific case, ode113 finishes the simulation around 30 minutes before the other two. Nevertheless, the results are consistent across the board. For variables such as the vertical coordinate of the chassis and the mechanical energy of the entire system, there is no variation in values, all solvers give the same results. The biggest differences are found in the tire deflection.

Table 6.11 - Results obtained for 3 solvers: ode45, ode23 and ode113.

Variable	Ode45	Ode23	Ode113
$\max(\delta_z)$ (m)	0.0676	0.0676	0.0676
$\min(\delta_z)$ (m)	6.9772×10^{-6}	1.1470×10^{-5}	6.0651×10^{-6}
$\text{avg}(\delta_z)$ (m)	0.0253	0.0246	0.0244
$\max(F_z)$ (N)	14362	14362	14362
$\min(F_z)$ (N)	1.3409	2.1827	1.2141
$\text{avg}(F_z)$ (N)	5109.4	4965.3	4905.9
$\max(z_{chassis})$ (m)	0.5167	0.5167	0.5167
$\min(z_{chassis})$ (m)	0.4841	0.4841	0.4841
$\text{avg}(z_{chassis})$ (m)	0.5002	0.5002	0.5002
$\max(E_m)$ (J)	1.8069×10^5	1.8069×10^5	1.8069×10^5
$\min(E_m)$ (J)	1.7703×10^5	1.7703×10^5	1.7703×10^5
Time (h)	3.41	3.34	2.95

Before discussing the detailed results, one must focus on why these simulations took much processing time than the flat ground ones. Since there is an obstacle on the course, the second contact method is used (see section 5.3), which is a more detailed and complex algorithm. It is then expectable to see an increase in time, especially because of the several interpolations made by the algorithm. Figure 6.17 shows the variation of time with each timestep for the three solvers. The solvers used, of the ode type, provide a variable timestep, which is adaptable to guarantee the best results. Every time there is a transition zone on the road, be it ascending or descending the bump, the gradient of the variation of time becomes almost flat, as showed in Figure 6.17. The transition zones take a significant toll on the simulator's performance.

(a) (b) (c)
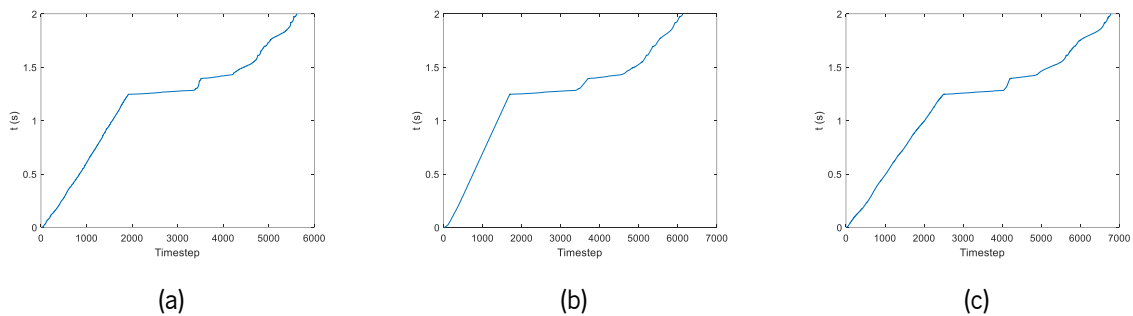
Figure 6.17 - Variation of simulated time with timestep. (a) Ode113. (b) Ode23. (c) Ode45.

The maximum tire deflection, obtained during the crossing of the bump, is the same for all three solvers, 0.0676 m. But the average and minimum values are slightly different. The minimum value presents an extreme case. Since it is so small across the board, it means that the wheel was lifted off the ground, as depicted in Figure 6.18. Any of the values obtained, are small enough to represent a wheel

lifting off. If the values given by ode45 are considered as the default values (this solver is known as the more accurate out of the three), then it is possible to conclude that the other solvers do not present big deviations in any category. The minimum value of deflection can be in fact be excluded because all of them represent a lift off.
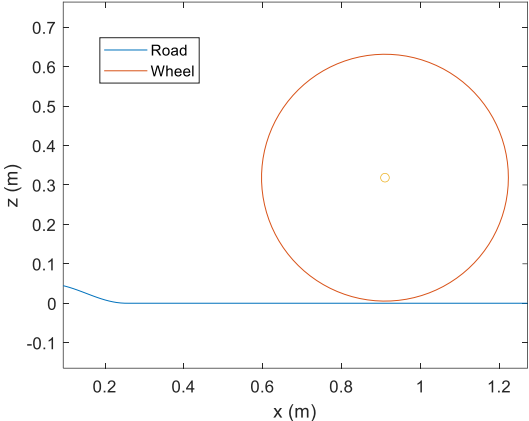
Figure 6.18 – Unrealistic behaviour found. The wheel loses contact with the road.

The average deflection value, however, is where the biggest differences can be found. Nevertheless, these values are only separated by 0.001 m, or to better comprehend, 1 mm. This difference is never big enough to create big disparities in the computation of the vertical force. Accordingly, the deviation between the average vertical force across solvers is about 200 N, which is just 4% of the vertical force average value. This does not have a big expression in any results and, so, the solver to be chosen must be the one with the best efficiency and processing time. The solver chosen to carry out the next simulations was the ode113, because it not only provides similar results, but is also 15% faster than any of the other two solvers, as seen in Figure 6.19.
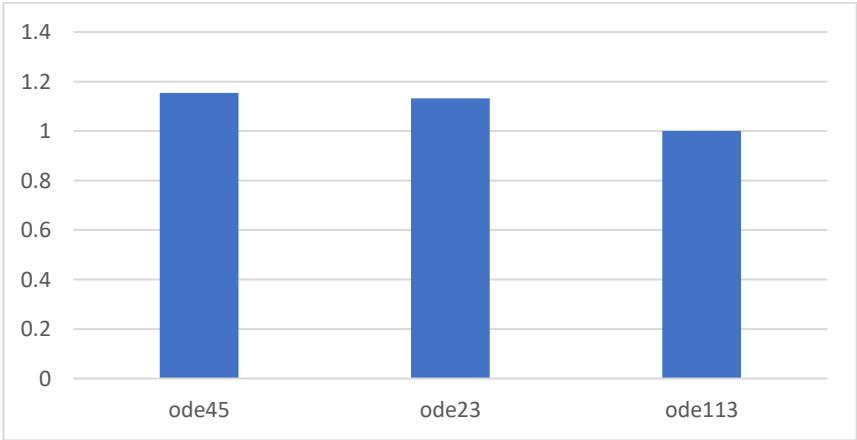
Figure 6.19 - Relative processing time of each solver.

The next step in this process is the refinement of the ode113 tolerances. Tolerances used by the solver can be the difference between a fast simulation or an extremely time-consuming one. The tolerances are based on the relative and absolute errors (Choose an ODE Solver, s.d.). In order to know what the best tolerance is to use a cluster of values was chosen to be tested, that being: $10^{-2}, 10^{-3}, 10^{-4}, 10^{-5}, 10^{-6}, 10^{-7}$. The output evaluated was exactly the same as the one used before in Table 6.11. Also, the road characteristics were kept. The next table shows the results for each simulation.

Table 6.12 - Results obtained for the different tolerances.

Variable	10^{-2}	10^{-3}	10^{-4}	10^{-5}	10^{-6}	10^{-7}
$\max(\delta_z)$ (m)	0.0676	0.0676	0.0676	0.0676	0.0676	0.0676
$\min(\delta_z)$ (m)	3.1159×10^{-5}	4.2547×10^{-5}	1.6345×10^{-6}	6.0651×10^{-6}	4.6865×10^{-6}	4.5012×10^{-8}
$\text{avg}(\delta_z)$ (m)	0.0237	0.0241	0.0240	0.0244	0.0234	0.0233
$\max(F_z)$ (N)	14361	14362	14362	14362	14362	14362
$\min(F_z)$ (N)	5.9233	8.1175	0.3287	1.2141	0.9567	0.0181
$\text{avg}(F_z)$ (N)	4734.9	4835.6	4819.5	4905.9	4720.9	4700.9
$\max(z_{chassis})$ (m)	0.5167	0.5167	0.5167	0.5167	0.5167	0.5167
$\min(z_{chassis})$ (m)	0.4841	0.4841	0.4841	0.4841	0.4841	0.4841
$\text{avg}(z_{chassis})$ (m)	0.5002	0.5002	0.5002	0.5002	0.5002	0.5002
$\max(E_m)$ (J)	1.8069×10^5	1.8069×10^5	1.8069×10^5	1.8069×10^5	1.8069×10^5	1.8069×10^5
$\min(E_m)$ (J)	1.7703×10^5	1.7703×10^5	1.7703×10^5	1.7703×10^5	1.7703×10^5	1.7703×10^5
Time (h)	0.93	1.64	2.00	2.97	4.44	7.06

Like in the previous refinement, there is no variance in both mechanical energy and chassis' vertical coordinate. All in all, one can conclude that these are more dependent on the contact estimation methods, which is invariable across the board. That said, those two variables mainly depend on the position of the car, which is always the same for each simulation, and the velocity gains and losses, which is also the same for each simulation.

Nevertheless, the other variables must be evaluated in order to choose the appropriate tolerance to use. Table 6.12 shows that for smaller tolerances, the less the error and, consequently, values closer to zero will be more precise, but the bigger the processing time. This is shown by the minimum value of the tire's deflection, apart from the cases 10^{-6} and 10^{-5}, which is probably due to some numerical errors made by the simulator. However, each value is small enough, like in the previous example, to well represent the lift of the wheel. One's attention must now turn to the average deflection along the road. Taking the 10^{-7} as the default result, there is in fact a decrease in deflection, with the decrease in tolerance. However, the difference between values is never more than 0.0011m, or 1.1 mm. Although this difference seems minimal, the biggest change is shown in the computation of the vertical force. The

maximum value is always the same across all tolerances, but the average value gets smaller, with the tightening of the tolerance. Also, the minimum values seem to get closer to zero, which is the ideal value, without touching the ground, there can be no vertical force acting upon the tire.

With everything said, one can consider the 10^{-2} as a good tolerance to use, because of its average deflection, which is close to the 10^{-7} case, and its diminutive processing time. However, its minimum vertical force is not low enough, especially in comparison with the value obtained by 10^{-4}. 10^{-7} should in fact be the tolerance to use, because it provides the best results out of the bunch. Nevertheless, it also takes much more time than any of the others to finish the simulation, at about 7 hours, which makes it totally inviable. Considering all of this, the choice must fall under the 10^{-4} category. First, this tolerance has better results than the next one, 10^{-5}. The deviation of the average deflection with the extreme case, 10^{-7}, stands at 0.0007 m, only 3% of the total value. Also, 10^{-4} is the second best when it comes to the minimum value of normal force, only behind the 10^{-7}. The difference in average normal force is of 119 N, or 2.5% of the most precise value (4700.9 N), which is acceptable. Finally, it can be said that the 10^{-4} case offers the best precision/processing time relation. While it has minimal deviation from the best values, this tolerance is 50% faster than 10^{-5}, and 3.5 times less time-consuming than the 10^{-7} case, sitting at around 2 hours, as can be seen in Figure 6.20.

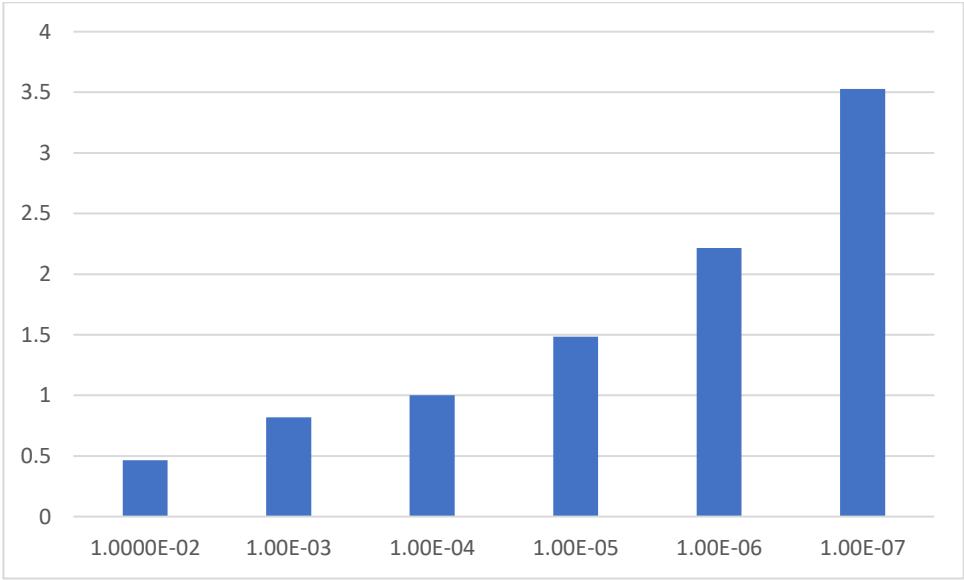**Figure 6.20** - Relative processing time across simulations with different tolerances.

In summation, the tolerance chosen to carry the simulation of the next scenarios is 10^{-4}. A case could be made for 10^{-3} or even 10^{-2}. The results do not differ that much. However, since these tolerances are relatively small, the solver could be prone to bigger numerical errors that could affect other parts of the

simulation, such as the calculation of the slip angle. A tolerance of 10^{-4} grants good computational time, precise results and, at last, the minimization of random numerical errors.

6.5   Simulation

With the refinement made in the previous section, it is necessary to simulate and analyse a car going over a road with obstacles. As previously explained, the car cannot traverse an obstacle without lifting its wheels off the ground. This unrealistic behaviour and its implications will be further explained in this section.

Some simulations will be presented, using the multibody system defined previously. The first simulation will use the bump represented in Figure 6.16 and the road used for the refinement as shown in Table 6.10. The results will be presented and explained, with a focus on the abnormal behaviour of the vehicle. Then, another road will be tested, this time with a bigger but flatter bump. Some suspensions parameters will be changed to evaluated whether this response is directly tied to the suspension system.

6.5.1   Simulation 1

The first simulation to study the suspension parameters uses the exact same characteristics used when refining the simulation. The only difference is that it already considers the refined solver: ode113, using a 10^{-4} tolerance. The variance of time with each timestep is represented in Figure 6.17.

The objective of this simulation is to analyse the behaviour of the vehicle, especially when it passes a small speed bump. The vehicle is let go at free-rolling state, like in Figure 6.21, and it reaches the bump in the middle of the road. Until it reaches the bump, the vehicle performs as expected.

Figure 6.21 - Top: Initial position of the car. Bottom: Final position of the vehicle.

As the wheel ascends the bump, the longitudinal force's module starts to increase. This is caused by the generation of a slip. This slip is due to the decrease of the wheel's angular velocity. Since a positive gradient exists, the ground will have a reaction on the wheel in all three directions. The lateral direction is uniform, making this reaction zero. But the longitudinal direction, x, is not. This creates a negative longitudinal reaction on the wheel that causes its rotation to diminish. In other words, the wheel loses rotation, as if it were braking. The angular velocity decreases more than the linear velocity, which in turn

increases the slip value, correspondent to a braking situation. The longitudinal contact force will then be negative, as shown in Figure 6.22. As for the descending part of the bump, the exact opposite happens. At $t = 1.30$ s, it is possible to observe the inception of a positive longitudinal force, which is caused again by the reaction of the soil, that is facing forward. In this case, since the car is descending a negative gradient, the wheel gains rotation, therefore creating a "driving" longitudinal force. It must be said that before the longitudinal hits its peaks, there are symmetrical peaks happening. This is mainly due to numerical errors of the integrator and the multibody dynamics algorithm.

	(a)	(b)
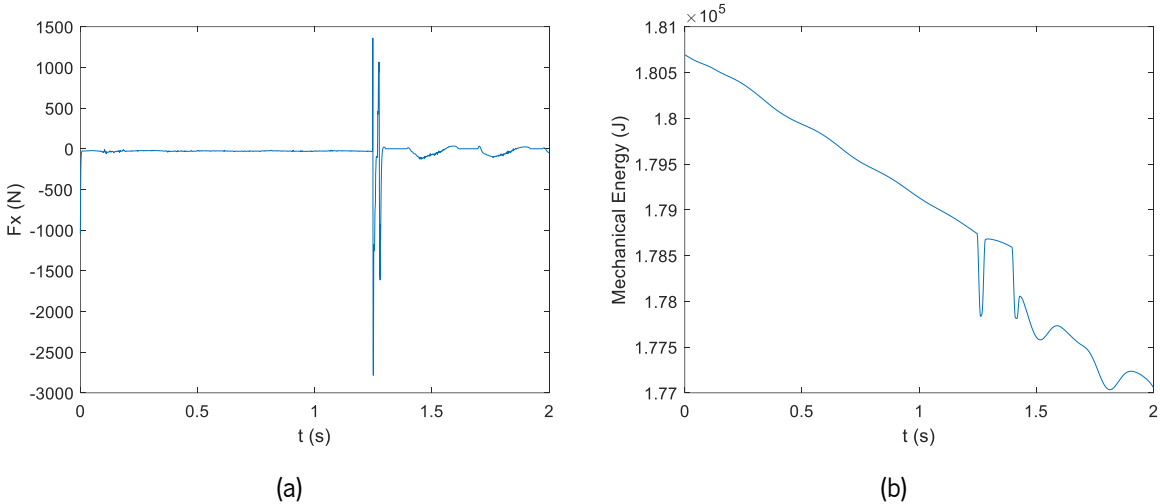
Figure 6.22 – (a) The variation of the front-left wheel's longitudinal force; (b) The variation of mechanical system of the vehicle.

Also, the mechanical energy of the system suffers a sudden drop, as seen on the right side of Figure 6.22, when entering the bump. If the velocity decreases, the kinetic energy will also decrease, but since the wheel is ascending the potential energy increases, making up for the loss in kinetic energy. In fact, this drop in mechanical energy is primarily due to the action of the suspension system. The spring at the front suspension will be compressed, while the wheel hits the bump. While this causes the wheel to brake, the spring is in fact storing that energy, so it is seen as a loss of mechanical energy. After the wheel surpasses the bump, the spring leaves the compression state and releases back the energy it had stored, causing a sudden increase in mechanical energy to its normal state. All in all, no mechanical energy is lost in the bump, other than due to the free rolling state of the car and some small damping effects of the suspension. It must be said that later, at $t = 1.40$ s, the same drop is seen. This is simply the effect of the rear suspension because the rear wheels start to ascend the bump.

At around $t = 1.20$ s, when the front wheels start to touch the bump, the behaviour, in terms of deflection, changes slightly. As can be seen in Figure 6.23, when entering the bump, the deflection of any tire starts to increase, which is expectable. This increase in deflection causes an enlargement of the

vertical force, since the two are directly proportional. As the wheel faces the bump, the deflection continues to increase, reaching a maximum. This maximum value is reached when the wheel is on top of the bump. After that, the bump descends, and so does the wheel. This causes the deflection to decrease the same amount it had increased before.

(a)   (b)
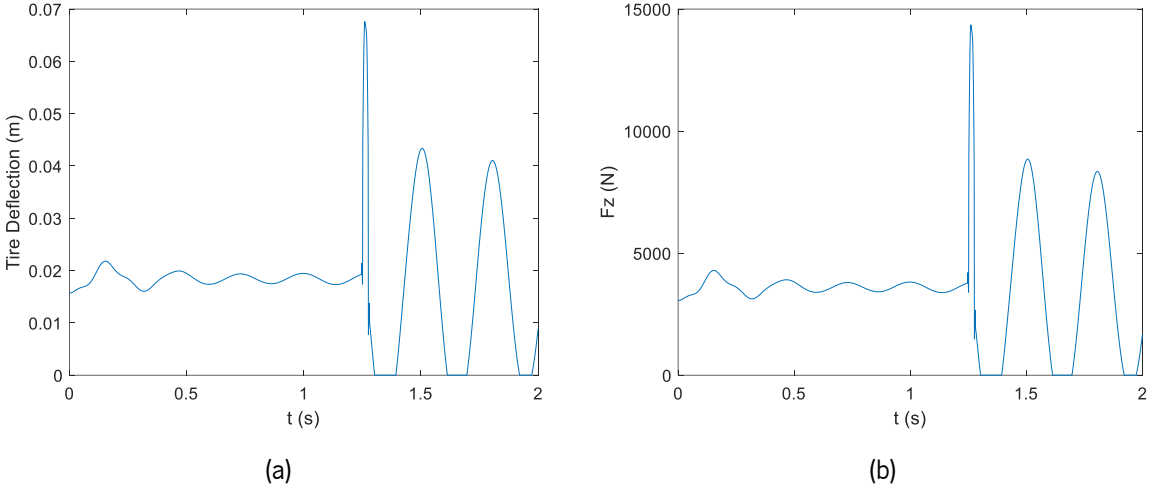
Figure 6.23 – (a) The variation of the vertical load for the front-left wheel; (b) The deflection for that wheel is represented across time.

The abnormality to notice is the maximum value of the normal force, which stands at 14362 N. As seen in (Garcia-Pozuelo et al., 2015), where similar simulations are performed, for a bump such as the one found in Figure 6.16, the vertical force is expected to reach a maximum of 10000 N. The value attained in this work is almost 50% bigger than that one. This may be caused by bad contact estimation.

The second thing to notice is that the decrease keeps happening as the car moves forward, causing the deflection to reach the value of the zero, right after it leaves the bump, which means that the wheel lost its contact with the road, as depicted ever-so-slightly in Figure 6.24.

Figure 6.24 - After the bump, the front wheels (blue) start to lift off the ground.

As can be seen in Figure 6.25, where the reaction forces of the suspension system on the tire are represented, at the same timestep, the reaction is non-existent. Until then the suspension system was working smoothly and correctly, balancing the contact vertical force by applying a symmetric force on the tire, with a symmetric direction. At $t = 1.25$ s, a maximum (in module) is reached. After this, the

reaction force reaches the value of zero, due to the loss of contact, and starts acting again when the contact with the road is regained.
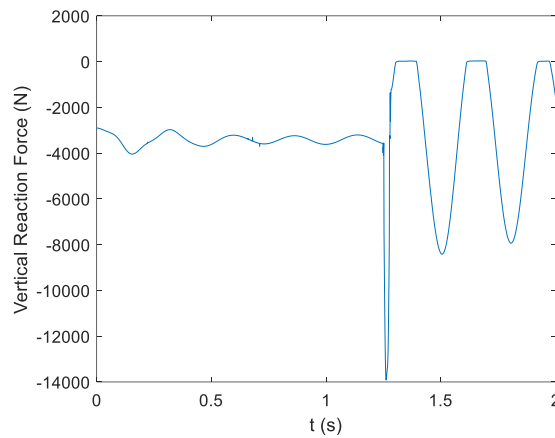
Figure 6.25 - Vertical reaction force of the suspension system on the wheel.

However, this regain of contact represents the wheel landing on the ground again, causing some serious instabilities, in the form of rebounds. These, on an initial state, cause the deflection to go up, followed by losses of contact. The suspension seems to be able to compensate the increases in vertical force, as seen in Figure 6.25, but does not avoid the losses of contact. Looking at the mechanical energy, it starts to suffer large decreases. In fact, this is where the damper starts to truly act. Since the wheel reaches an instability point, the damper will dissipate energy to try to stabilize the wheel and eliminate the big oscillations. Nonetheless, the suspension system cannot contradict the oscillations and, therefore, the behaviour persists, and the wheel is rebounding across the road. This effect can be characterized by a transient state. After a while, the wheel reaches an equilibrium point and its initial state. This unrealistic situation, which happens at and after the bump, does not allow the results to be precise and so something needs to be corrected.

6.5.2   Simulation 2

As seen in the previous simulation attempt, the wheel loses contact with the road sometime after the bump. This ends up happening for every single wheel of the car. For such a small bump and going at a speed of 60 km/h, this is an unexpected behaviour, which should not be happening. To try correcting this, another simulation was made, this time with a different bump. The road is the same as in Table 6.10 and initial conditions of problem stand as well. The bump, reproduced in Figure 6.26, is also positioned in the middle of the road.
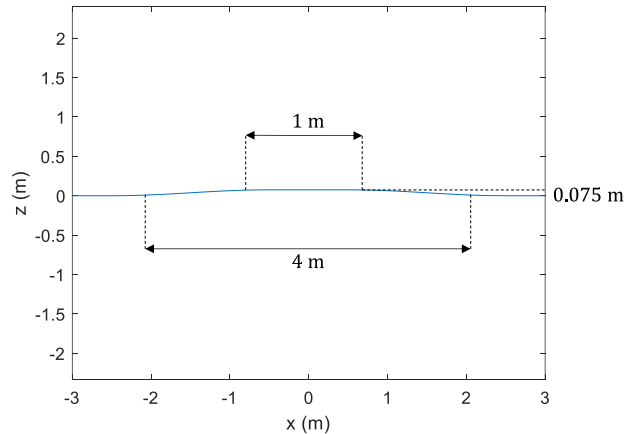
Figure 6.26 - Dimensions of the new bump modeled for simulation 2.

This bump, although larger in length and with a slightly bigger height, represents a much more gradual gain of vertical coordinate, which means that ascent will be smoother and more uniform. This is way it is expected that wheels will not show a sudden, almost instantaneous, increase in vertical force. As seen in Figure 6.27, the car performs as before, although this time the loss of contact happens on top of the bump, right after the ascending phase. Before, the wheel lifted off the ground just a small amount, as in Figure 6.24, because only two wheels could be at the bump at the same time. This type, as the front-left wheel, studied in this case (all others behave similarly), starts to lose contact, the rear wheels hit the bump, and so the entirety the car naturally ascends. This causes the front wheels to "jump" even higher than before.
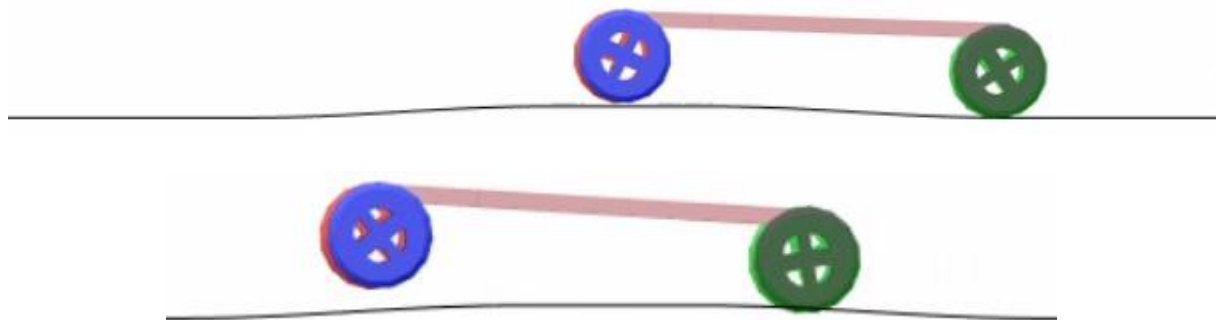
Figure 6.27 - Representation of the front tires (blue/red) losing contact with the road and performing a "wheelie".

Figure 6.28 shows the variation of both tire deflection and position of the front left wheel with time. The first peak, from around 1.10 s to 1.15 s, represents, again, the normal behaviour of the tire as it hits the bump and starts to ascend. While on the first simulation, the raise in the value of deflection was almost instantaneous, here it builds up more slowly. This is simply due to the geometry and length of the

new bump. As it reaches the flat zone of the bump's top, the deflection is maximum. However, instead of decreasing and stabilizing, the deflection, from 1.15 s to 1.25 s, decreases all the way to zero. This proves, as seen in Figure 6.27, that in this case the front wheels lose contact in the flat area, right after the initial ascent. Additionally, unlike the first simulation, it is shown that the wheel stays with no contact for a much higher period. Instead of moving up only 0.075 m (the height of the bump), the centre of mass climbs all the way up to a vertical coordinate of $z = 0.48$ m, an increase of almost 0.20 m from the initial position, and almost three times as high as the bump's height.

(a)   (b)
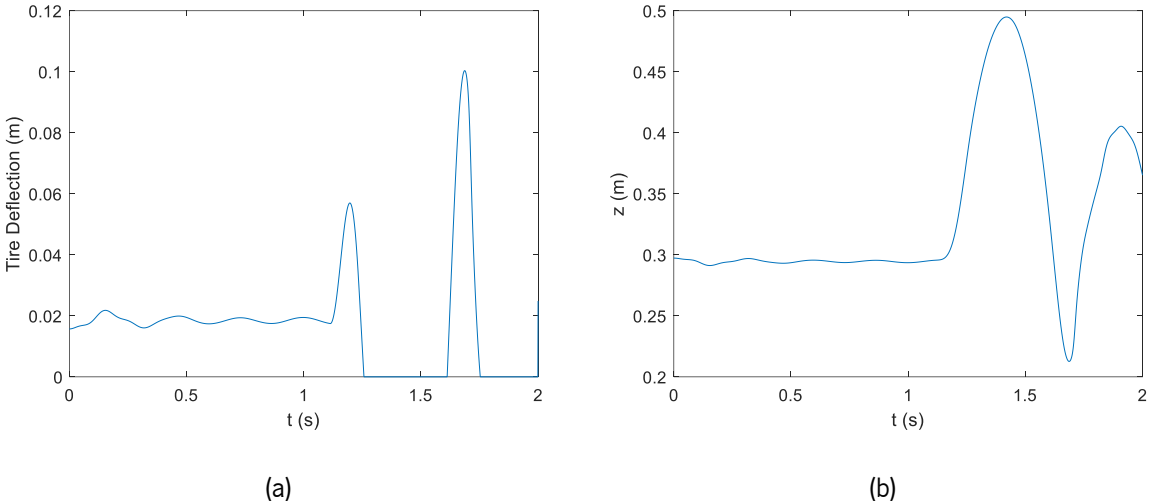
Figure 6.28 – (a) Variation of the front-left tire deflection. (b) Position of the wheel's centre of mass over time.

The bigger period of time while on air, and the larger height, explains what happens after. At $t = 1.55$ s, the wheel lands again and so the deflection starts to increase, this time massively, reaching a worrying value of $\delta_z = 0.10$ m. This maximum peak can only be explained by the instability created by the impact of the wheel on the ground. Since it reaches unusual heights while on air, the impact will be much stronger and so the wheel will deform massively. As seen in Figure 6.29, the mechanical energy of the system, after the landing of the wheel, drops massively and continues to do so until the end. This is, again, caused by the dissipation of energy promoted by the suspension's dampers to stabilize the car. The wheel cannot be stabilized and continues to oscillate and lose contact until the end of the simulation. The rear wheels also promote this effect, but the front wheels never reach those heights again, although they continue to lose contact. The suspension can always contradict the vertical contact force and it is possible to conclude that the lift off is not caused by the implementation of the multibody system.

(a)   (b)
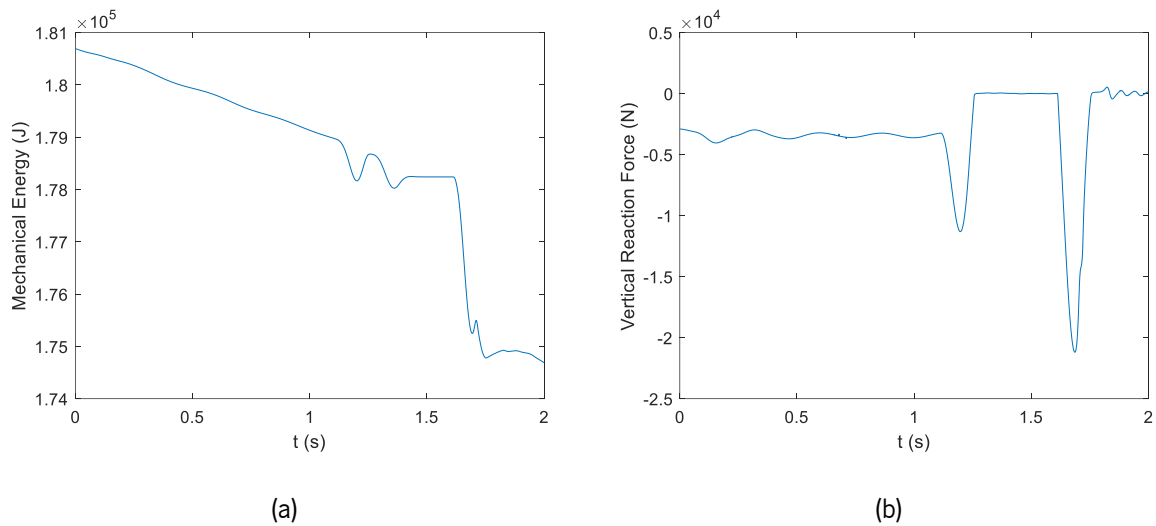
Figure 6.29 – (a) Variation of the mechanical energy of the system. (b) Vertical reaction force on the wheel (b).

6.5.3   Simulation 3

A third and last simulation was made. This simulation shares all the characteristics of the previous one, using the same road with the same bump. The initial conditions are also the same. Nevertheless, this last simulation was made to analyse the behaviour of the car if the suspension's parameters were changed to the ones represented in Table 6.13. This was mainly made to correct the wheel's lifting off the ground.

The parameters used to define the vehicle's suspension were directly taken from (Ambrósio & Verissimo, 2009). An inspection to other works, such as (Jugulkar, 2016) and (Dehbari & Marzbanrad, 2018) where similar suspension systems are studied, showed that these values are in accordance with what is used, so they should not pose any problems to the simulation. Nevertheless, a limit-test was made, and these parameters were changed, to overexaggerated values of damping and spring stiffness. The values used in the current simulation, present in Table 6.13, correspond to 10 times as much as the ones previously defined. The undeformed length of the springs was left untouched.

Table 6.13 - New suspension parameters used.

Suspension	Spring stiffness (N/m)	Damping (Ns/m)	Undeformed length L_0(m)
Macpherson Strut	591900	79190	0.33
Rear Damper	–	150000	–
Torsion Bar	145300	–	0.115

Looking at Figure 6.30, it is immediately noticeable that the deflection of the tire is not in a stationary state before it hits the bump. Contrary to the previous simulation, the deflection has great variations even when the tire is crossing the flat area of the road, posterior to the bump. Also, the mechanical energy does not vary the same way it does in the previous simulation, there is much more non-linearity that creates an ondulation of values.
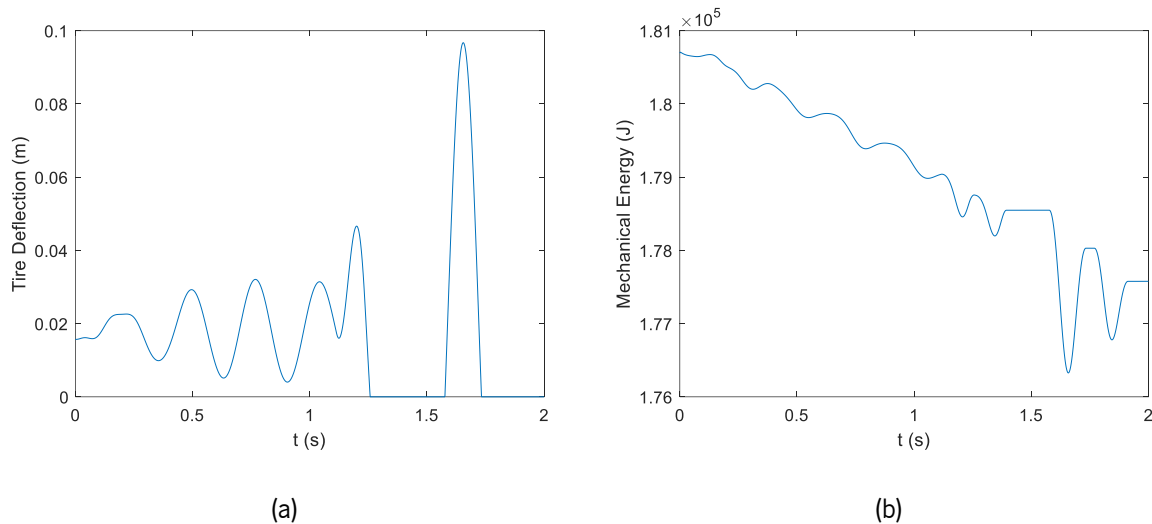
Figure 6.30 – (a) Variation of the mechanical energy of the vehicle; (b) Variation of the deflection.

The non-linear, transient state could be explained by the increase in some parameters. The stiffer a spring is, the larger the amount of energy stored in it is. However, the faster the release of energy is. Theoretically, that is what is causing those oscillations in deflection. The spring is being compressed and, thus, is storing energy, that is being release too fast, creating oscillations in the car. The damping, however, seems not to be able to dampen those oscillations properly, since the spring stiffness is extremely high, which causes the initial oscillation of deflection to raise in magnitude. Nonetheless, it is known that at $t = 1.10$ s, the wheel hits the bump, and the deflection increases naturally, reaching its first peak at the top of the bump. That first peak corresponds to $\delta_z = 0.05$ m, which is slightly smaller than the value encountered in the previous simulation ($\delta_z = 0.06$ m). The change in parameters showed to have a positive effect on the "real" peak of tire deflection.

Nevertheless, at $t = 1.25$ s, the wheel loses contact with the soil. Figure 6.31 shows the variation of the wheel's centre of mass with time. It is possible to conclude that it still lunges up into the air a considerable amount (0.016 m). The change of parameters did not prevent that from happening. The maximum value of deflection after the wheel hits the ground is never as high as it was before, which is also shown by the maximum vertical position of the wheel being lower than in the previous simulation. However, the second oscillation, which is right after the wheel hits the ground, seems to take it further

up than in the simulation 2. The centre of gravity of the wheel reaches a higher vertical coordinate that it did right after the first loss of contact. This new suspension seems to be damping the deflection but not the losses of contact. This could be caused by the exaggerated stiffness of the springs. They are required to store a lot of energy in order to compensate the exaggerated vertical force caused by the deflection. That energy is being returned too fast, as represented in Figure 6.30, hence, creating bigger oscillations, which means that the springs are, in fact, under-dampened. The mechanical energy graph shows just that there is always more energy in play in this simulation, and that energy is being stored and released by the springs, without any notorious losses. Those losses would be relevant, meaning that the dampers were dissipating energy to stabilize the springs and, therefore, the wheels.
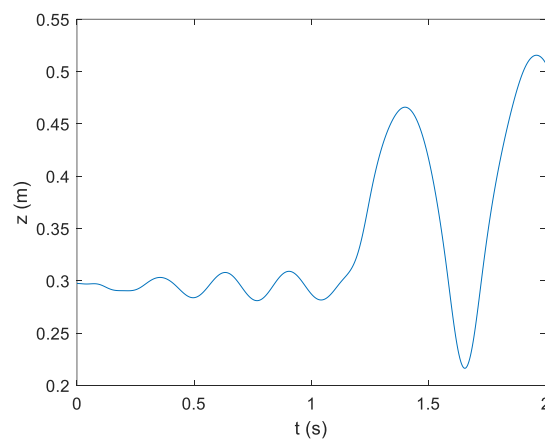
Figure 6.31 - Evolution of the vertical position of the wheel.

All in all, the limit-test showed that the algorithm created is overestimating the value of the vertical force when calculated over an obstacle, such as a bump, which can be causing the loss of contact. Nevertheless, it was shown that the spring's stiffness and the damper's damping are not directly proportional, so to say. The increase in stiffness requires a bigger increase in damping, to compensate for the fast releases of more energy that directly translate in more oscillations from the spring.

7. Concluding Remarks

In this chapter some conclusions will be withdrawn from all the work done within the scope of this dissertation. Firstly, a small overview about the compiled state of the art will be done. Some conclusions about the simulation work will be discussed, from the definition of the multibody system to the creation of the contact estimation method. Then, some results obtained will also be analysed. The second part of this chapter comprises the future works to be done to sharpen this one.

7.1   Conclusions

This work started with a thorough review of the literature about vehicles. Firstly, some general components were studied, such as the tire and the suspension system. It was seen that tires underwent some major changes over the years, culminating in a radial-layered structure, covered by a rubber tread, that acts as a surface between the vehicle and the road. Secondly, the different types of suspension systems were analysed and, although different, these, most of the time, must provide safety and driving comfort to the passengers. It was seen that the Macpherson strut, the double-wishbone, and the multilink axles are some of the most used in passenger cars these days. Lastly, the tire-road dynamics were introduced. As is known, the contact between the tire and the road provides a platform for the transmission of frictional forces in all directions, that enable the motion of the car. The physical principles behind this contact were studied and several tire force models, which depict these phenomena in different ways, were presented, with an emphasis on the mathematical ones.

The purpose of this work was to study the performance of a vehicle's suspension system when going over roads with different obstacles, such as bumps and potholes. As a vehicle can be considered a multibody system, a code, known as MUBODYNA3D (Flores P. , 2012), needed to be used to perform multibody forward dynamic analysis. The first step was, then, to create a module, inside MUDODYNA3D, capable of simulating vehicle dynamics, which was not available before the inception of this work. For this module to work properly, two algorithms were created from scratch: one for flat roads and the other for roads with obstacles.

Both algorithms work under the same basis, while achieving it in different ways. Both identify the contact point of a wheel touching a road, which can be used to predict the contact forces at a certain timestep. For flat roads, the contact identification was made by using the tire's profile and finding its lowest vertical coordinate, that would correspond to the contact point. It was possible due to the invariable normal direction of the road. This was defined as an optimization problem, which could be solved by the

simulator, MATLAB. For roads with obstacles, the approach needed to be different. Instead of formulating an optimization problem, this scenario was defined as a geometrical one, which neglected the tire's profile, by stating that the contact point is the one that creates a vector, with the wheel's centre of mass, perpendicular to the tangential directions of the road. For such, a non-linear system of equations, solvable by MATLAB iteratively, was established. Additionally, this algorithm can also predict the existence of several possible points of contact, which fundamentally change the position of the effective one. In the end, both algorithms are used to attain the tire deflection and effective velocity of the wheel at a certain timestep, which makes the computation of the slip and slip angle possible. Finally, the vertical force, due to the deflection, is obtained, and all the other contact forces and torques are estimated, using the extended Magic Formula (Pacejka, 2002; Bakker et al., 1987; Bakker et al., 1989), which was chosen over other models, due to its simplicity, reliability and fidelity when representing the contact forces.

To test the aforementioned principles and get results, a small family car based on (Ambrósio & Verissimo, 2009), was created. All the bodies/components were defined along the joints that connect them. The multibody system was simulated, with initial conditions such as the components' velocity and centre of mass. The car's trajectory was then predicted, along different road profiles.

The first simulations were relative to a flat road situation. This road had a constant height, which made the tire's deflection almost invariable. It was seen that, since the centre of mass of the car is pushed further to the front, the vertical load would be higher on the front wheels. The distribution of mass caused the front wheels to have bigger deflections and, therefore, support more normal force. The car always performed as expected, starting at an initial position, and ending further up the road, while being in a free rolling state, with almost no slip.

These first simulations were particularly useful to verify the forward analysis, which always culminated on a correct trajectory of the multibody system previously defined. It was seen that correction of initial conditions was possible and that there were no violations to the constraints imposed by the joints on the bodies. It was also possible to observe that car starts with a transient behaviour, when it comes to the deflection, that is dampened as the simulation evolves, resulting in an almost steady-state by the end. Lastly, the tire model was verified as well. The contact forces were shown to be well computed, but mostly the steady-state behaviour of the Magic Formula was confirmed, by the way the longitudinal force evolved instantaneously, like a square input, after the application of a braking or acceleration torque. There was no lag nor dynamic behaviour.

The second batch of simulations were done to refine the solver to integrate the accelerations given by the solution of the equations of motion. This time a road with a bump in the middle was used, and the

second contact method was studied. No problems arose and it was seen that this contact method takes a lot more time to simulate a case than the first one, due to the changing road gradients. With these simulations it was possible to conclude that all solvers gave almost the same results, so the choice ended up falling on the one with the best efficiency, the ode113.

The last group of simulations were done using a road with obstacles. These could be considered the kernel of this work since they were the ones to be thoroughly analysed to obtain the suspension system performance.

The first simulation, within this group, used a relatively small bump, with a height of 0.05 m. The car was rolling at an acceptable velocity of 60 km/h. The first thing to note was the action of the bump on the longitudinal force of the tire. Since there was no variation along the lateral axis, the bump would create a longitudinal reaction force on the tire. As the tire moved up the obstacle, that reaction would cause a negative longitudinal force, acting as a sort of brake. As the tire reached the flat part of the bump, this reaction would drop all the way down to zero. Then, as the tire started to descend the last part of the bump, another longitudinal reaction force was created, this time causing the tire's rotational velocity to increase, inducing a slip that caused a positive longitudinal force. The suspension system's performance was also analysed, and it was possible to conclude that the springs were storing mechanical energy, since they were being compressed, as the tire rolled over the bump. This caused a dip in the mechanical energy that would finally be restored, when the springs released that energy back, after leaving the compressed state. This meant that car was also being braked by the force of the spring. The dampers were responsible for the dissipation of energy that occurs after the bump. This is the effect of the dampers trying to stabilize the car.

Some notes about the deflection were taken. As the car ascends the bump, the deflection rises in value, which was expected as seen in (Filipozzi et al., 2021; Garcia-Pozuelo et al., 2015). As the car descends the bump, the deflection goes back to its normal state, which is the value that it possesses along the flat area of the road. However, it was seen that the maximum value was too high. The previously referred literature states that it should have been around 10000 N, while in fact it was 50% bigger, which is unrealistic. After the wheel had gone over the bump, it was noted that that valued diminished into zero. This created a lift off effect and the wheel had some airtime. When it hit the ground, the impact created some instabilities and the suspension system tried to stabilize the car, seen by the massive loss of mechanical energy provoked by the dampers that needed to stabilize the oscillations of the springs, with no effect, since the wheel lifted off again.

To dig deeper into this "lift off" effect, another simulation was performed, this time with a bigger but flatter bump. Although the suspension system was in fact working, since it was contradicting the vertical contact force when it existed, this new bump did not prevent the lift off effect. Here the tire deflection was never as big as it was in the first simulation, but the wheel still lifted off, this time to a higher vertical coordinate. This was caused by a sort of "wheelie" effect done by the car. The rear wheels ascended the bump as the front wheels were lifting, causing them to go higher. The rear wheels also lost contact and the full car stayed much longer in the air. The impact was much bigger when hitting the road, causing massive losses of energy, an increase in tire deflection and an oscillatory behaviour from the wheel.

A third and final simulation was done, where all suspension parameters were increased. This still caused the loss of contact. Nonetheless, the increase in suspension stiffness created faster releases of energy, and the oscillatory behaviour could not be dampened by the dampers. In fact, this behaviour was so violent that the car, after hitting the ground for the first time, lifted off to bigger heights than right after the first loss of contact. This shown that the increase in stiffness, and the faster releases of much more energy, could not be dealt by the same increase in damping, that could not dissipate energy to stop the oscillations. It can be concluded that these two variables, damping and stiffness, are not directly proportional. An increase in stiffness should be accompanied by a bigger increase in damping.

After all, it can be concluded that the contact estimation method is overestimating the value of the vertical force, when a tire is traveling across an obstacle, to the point where it gets somewhat unrealistic. This overestimation is, most likely, causing the loss of contact, which is creating a lift off effect on all wheels. Thus, a sensibility study on suspension parameters could not be carried out. Nonetheless, the work carried out, which lead up to the writing of this dissertation, culminated in the creation of a new module in the simulation code. This module, that can be thoroughly enhanced, is capable of simulating complex vehicle dynamics, which was not possible before within MUBODYNA3D.

Finally, this work showed that the definition of a multibody system is particularly important when carrying out simulations such as the ones presented. Complex situations, that otherwise would only be possible to be tested with the real, expensive models, can be easily described by computational methods, converging, most of the time, in precise results.

7.2   Future Works

As for future works, some must be carried out to truly augment this work. It is known that the tire-road dynamics algorithm, that comprises the contact estimation and the computation of forces, is overestimating the value of the vertical, when the car is crossing an obstacle. This, although not certain,

is mainly caused by the contact estimation method. The first work should be to hone that algorithm. The contact estimation method for roads with obstacles must be reviewed, tested, and sharpened, so that it becomes more accurate and precise. Also, an algorithm for the turning of the front wheels should be implemented. This could easily extend the practical cases that the algorithm could simulate.

The Magic Formula is an effective and precise semi-empirical tire model. However, it is a steady-state one and the dynamic physical models are more robust and can better represent what really happens in the contact between tire and road. Also, they enable the analysis of other characteristics, such as dynamic friction, tire geometry, variable inflation pressure and heating. These models can also simulate cases where the road is extremely rough, with the presence of asperities.

Ultimately, a sensibility study of the suspension parameters must be carried out, when the previous solutions have been implemented. This will make for a better understanding of the real implications of obstacles and contact forces on the suspension system of the car. Additionally, this study could prove useful for the analysis of the effect that the road has on driving conditions, such as handling, and the comfort of the driver and the passengers inside the car cabin. Finally, with a study done with ideal joints, a new one with elastic joints could be implemented, along with flexible bodies, instead of fully rigid ones.

BIBLIOGRAPHY

A. Keller, A. (2018). *Mathematical Optimization Terminology.* Academic Press.

A. Ortiz, J. A. (2006). An easy procedure to determine Magic Formula parameters: a comparative study between the starting value optimization technique and the IMMa optimization algorithm. *Vehicle System Dynamics, Vol. 44, No. 9*, pp. 689–718.

Ambrósio, & Verissimo. (2009). Sensitivity of a vehicle ride to the suspension bushing characteristics. *Journal of Mechanical Science and Technology 23*, pp. 1075-1082.

Ambrósio, J., & Verissimo, P. (2009). Improved bushing models for general multibody systems and vehicle dynamics. *Multibody Syst Dyn*, pp. 341–365.

Ambrósio, J., & Verissimo, P. (2009). Sensitivity of a vehicle ride to the suspension bushing characteristics. *Journal of Mechanical Science and Technology 23* , pp. 1075-1082.

Bakker, E., Nyborg, L., & Pacejka, H. (1987). Tyre modelling for use in vehicle dynamics studies. *SAE paper 870421*.

Bakker, E., Pacejka, H., & Lidner, L. (1989). A new tyre model with an application in vehicle. *SAE paper 890087*.

Bellis, M. (2014). *John Dunlop, Charles Goodyear, and the History of Tires*. Obtido de ThoughtCo website: https://www.thoughtco.com/john-dunlop-charles-goodyear-tires-1991641

Besselink, I. P. (2004). The SWIFT tyre model: overview and applications. *Proceedings of AVEC '04*, pp. 525-530.

Bhoraskar, A., & Sakthivel, P. (2017). A Review and a Comparison of Dugoff and Modified Dugoff Formula with Magic Formula. *2017 International Conference on Nascent Technologies in the Engineering Field* .

Bian, M. C. (2014). A Dynamic Model for Tire/Road Friction Estimation under Combined Longitudinal/Lateral Slip Situation. *SAE Technical Paper 2014-01-0123*.

Blundell, M. V. (1999). The modelling and simulation of vehicle handling Part 1: Analysis methods. *Proceedings of the Institution of Mechanical Engineers, Part K: Journal of Multi-body Dynamics*.

Blundell, M. V. (2000). The modelling and simulation of vehicle handling Part 3: Tyre modelling. *Proceedings of the Institution of Mechanical Engineers, Part K: Journal of Multi-body Dynamics*.

Blundell, M., & Harty, D. (2004). *Multibody Systems Approach to Vehicle Dynamics.* Oxford, UK: Elsevier Butterworth-Heinemann.

Burton, D., Delaney, A., Newstead, S., Logan, D., & Fildes, B. (2004). *Evalutation of Anti-Lock Braking Systems Effectiveness.* Royal Automotive Club of Victoria (RACV) Ltd.

Canudas-de-Wit, C., Olsson, H., Åström, K., & Lischinsky, P. (1995). A new model for control of systems with friction. *IEEE Transactions on Automatic Control*, pp. 419-425.

Canudas-de-Wit, Tsiotras, Velenis, Basset, & Gissinger. (2002). Dynamic Friction Models for Road/Tire Longitudinal Interaction.

Choose an ODE Solver. (s.d.). Obtido de MATLAB's website: https://www.mathworks.com/help/matlab/math/choose-an-ode-solver.html

Contact Patch. (s.d.). Obtido de Tire Rack website: https://www.tirerack.com/tires/tiretech/techpage.jsp?techid=10

Continental takes top accolades in the Auto Express Product awards 2019. (2019). Obtido de Continental website: https://www.continental-tyres.co.uk/car/about-us/media-services/newsroom/auto-express-product-awards-2019

Czop, P. (2011). Application of an Inverse Data-Driven Model for Reconstructing Wheel Movement Signals. *Metrology and Measurement Systems.*

Dahl, P. (1968). *A solid friction model.* Technical Report, The Aerospace Corporation.

Dehbari, S., & Marzbanrad, J. (2018). Kinematic and Dynamic Analysis for a New MacPherson Strut Suspension System. *Mechanics and Mechanical Engineering.*

Dugoff, H., Fancher, P., & Segel, L. (1969). Tire Performance Characteristics Affecting Vehicle. *Highway Safety Research Institute.*

Duym, S. W. (2000). Simulation Tools, Modelling and Identification, for an Automotive Shock Absorber in the Context of Vehicle Dynamics. *Vehicle System Dynamics*, pp. 261-285.

ETRTO: Standards Manual. (2003). The European Tyre and Rim Technical Organization .

Filipozzi, L., Assadian, F., Kuang, M., Johri, R., & Velazquez Alcantar, J. (2021). Estimation of Tire Normal Forces including Suspension Dynamics. *Energies.*

Flores, P. (2012). MUBODYNA3D. University of Minho, Portugal.

Flores, P. (2015). *Concepts and Formulations for Spatial Multibody Dynamics.* Springer.

fmincon Documentation. (s.d.). Obtido de MATLAB's website : https://www.mathworks.com/help/optim/ug/fmincon.html

fsolve Documentation. (s.d.). Obtido de MATLAB's website: https://www.mathworks.com/help/optim/ug/fsolve.html

Garcia-Pozuelo, D., Gauchia, A., Olmeda, E., & Diaz, V. (2015). Bump Modeling and Vehicle Vertical Dynamics Prediction. *Advances in Mechanical Engineering*.

Guiggiani, M. (2014). *The Science of Vehicle Dynamics: Handling, Braking, and Ride of Road and Race Cars.* Springer.

Hegazy, S., Rahnejat, H., & Hussain, K. (2000). Multi-Body Dynamics in Full-Vehicle Handling Analysis under Transient Manoeuvre. *Vehicle System Dynamics*, pp. 1-24.

histc Documentation. (s.d.). Obtido de MATLAB'S website: https://www.mathworks.com/help/matlab/ref/histc.html

Hoogh, J. d. (2005). *Implementing inflation pressure and velocity effects into the magic formula tyre model.* Master's thesis, Eindhoven University of Technology.

Hu, J., Rakheja, S., & Zhang, Y. (2019). Tire-Road Friction Coefficient Estimation underConstantVehicleSpeedControl. *IFAC-PapersOnLine,*, pp. 136-141.

Jugulkar, L. M. (2016). Analysis of suspension with variable stiffness and variable damping force for automotive applications. *Advances in Mechanical Engineering*.

Kahaner, D. C. (1988). *Numerical Methods and Software.* Prentice Hall.

Khaled, M., Harambat, F., Yammine, A., & Peerhossaini, H. (2010). Aerodynamic Forces on a Simplified Car Body: Towards Innovative Designs for Car Drag Reduction. *American Society of Mechanical Engineers, Fluids Engineering Division (Publication) FEDSM*.

Kissai, M., Monsuez, B., Mouton, X., Martinez, D., & Tapus, A. (2019). Adaptive Robust Vehicle Motion Control for Future Over-Actuated Vehicles. *Machines*.

Korunovic, N., Trajanovic, M., & Stojkovic, M. (2008). Finite element model for steady-state rolling tire analysis. *Journal of Serbian Society of Computational Mechanics*, pp. 63-79.

Li, L. (2009). Comprehensive prediction method of road friction for vehicle dynamics control. *Proceedings of the Institution of Mechanical Engineers Part D Journal of Automobile Engineering*.

M V Blundell, D. H. (2007). Intermediate tyre model for vehicle handling simulation. *Proceedings of the Institution of Mechanical Engineers, Part K: Journal of Multi-body Dynamics*.

Marques, F., Flores, P., & P. Souto, A. (2017). On the constraints violation in forward dynamics of multibody systems. *Multibody Syst Dyn*, pp. 385–419.

Mavros, G., Rahnejat, H., & King, P. (2005). Transient analysis of tyre friction generation using a brush model with interconnected viscoelastic bristles. *Proc. IMechE Vol.219 Part K: J. Multi-body Dynamics*, pp. 275-283.

MF-TYRE & MF-SWIFT 6.1: USER MANUAL 2008. (2008). TNO Automotive .

Nikravesh. (2007). Initial condition correction in multibody dynamics. *Multibody Syst Dyn*, pp. 107–115.

Nikravesh, P. E. (1988). *Computer Aided Analysis of Mechanical Systems.* Prentice-Hall, Inc.

Pacejka, H. B. (2002). *Tyre and Vehicle Dynamics* (2° ed.). Oxford, UK: Butterworth-Heinemann.

pchip Documentation. (s.d.). Obtido de MATLAB's website: https://www.mathworks.com/help/matlab/ref/pchip.html

ProTyre's website. (s.d.). Obtido de https://www.protyre.co.uk

Rear Axle Trailing Arm Suspension. (2012). Obtido de Maybach blog: http://maybach300c.blogspot.com/2012/09/rear-axle-trailing-arm-suspension.html

Reimpell, J., Stoll, H., & W. Betzler, J. (2001). *The Automotive Chassis: Engineering Principles.* Butterworth-Heinemann.

Rill, G. (2018). Sophisticated but quite simple contact calculation for handling tire models. *Multibody Syst Dyn (2019) 45*, pp. 131–153.

Rill, G. (2019). Sophisticated but quite simple contact calculation for handling tire models. *Multibody Syst Dyn*, pp. 131–153.

Rill, G., & Castro, A. (2020). *Road Vehicle Dynamics: Fundamentals and Modeling with MATLAB.* CRC Press.

Robinson, M. (2018). *What Actually Is Double Wishbone Suspension?* Obtido de CarThrottle website: https://www.carthrottle.com/post/what-actually-is-double-wishbone-suspension/

S Hegazy, H. R. (1999). Multi-body dynamics in full-vehicle handling analysis. *S Hegazy, H Rahnejat and K Hussain*.

Schmeitz, A., Besselink, I., Hoogh, d. J., & Nijmeijer, H. (2005). Extending the Magic Formula and SWIFT tyre models for inflation pressure changes. *In Reifen, Fahrwerk, Fahrbahn*, pp. 201-205.

Schramm, D., Hiller, M., & Bardini, R. (2014). *Vehicle Dynamics: Modeling and Simulation.* Berlin, Germany: Springer.

Shekhar, R. (2017). *Stability Analysis during Active Tire Excitation for Friction Estimation.* Stockholm, Sweden: KTH Royal Institue of Technology: School of Engineering Sciences.

spline Documentation. (s.d.). Obtido de MATLAB's website: https://www.mathworks.com/help/matlab/ref/spline.html

Suspension Springs - an introduction. (2016). Obtido de VEHICLE DYNAMICS ENGINEERING website: https://vehicledynamics.weebly.com/home/suspension-springs-a-introduction

Svendenius, J. (2007). *Tire Modeling and Friction Estimation.* Lund: Department of Automatic Control, Lund University.

Svendenius, J. (2007). *Tire Modeling and Friction Estimation.* Department of Automatic Control, Lund University.

Tan, D., Wang, Y., & Zhang , L. (2007). Research on the Parameter Identification of LuGre Tire Model Based on Genetic Algorithms.

Tire. (2021). Obtido de Wikipedia: https://en.wikipedia.org/wiki/Tire

Toyota's website. (s.d.). Obtido de https://global.toyota/en/

Uffelmann, F. (1980). *Berechnung des Lenk- und Bremsverhaltens von Kraftfahrzeugzügen auf.* Dissertation, TU Braunschweig, Braunschweig.

Uil, R. (2007). *Tyre models for steady-state vehicle handling analysis.* Eindhoven University of Technology.

Volante website. (s.d.). Obtido de https://volantesic.pt/renault/clio/2004/usado/?ID=396790

W. Hirschberg, G. R. (2007). Tire model TMeasy . *Vehicle System Dynamics*, pp. 101-119.

What is a damper. (2019). Obtido de Suspension secrets website : https://suspensionsecrets.co.uk/damper/

Wiegner, P. (1974). *Über den Einfluss von Blockierverhinderern auf das Fahrverhalten von.* Dissertation, TU Braunschweig,.

Zal, P. (s.d.). *2004 Renault Clio 1.2 (man. 5) engine Horsepower / Torque Curve*. Obtido de Automobile Catalog website: https://www.automobile-catalog.com/curve/2004/2949320/renault_clio_1_2.html

Zhao, Y.-Q., Li, H.-Q., Lin, F., Wang, J., & Ji, X.-W. (2017). Estimation of Road Friction Coefficient in Different Road Conditions Based on Vehicle Braking Dynamics. *Chin. J. Mech. Eng*, pp. 982–990.

Zhou, H., & Liu, Z. (2010). Vehicle Yaw Stability-Control System Design Based on Sliding Mode and Backstepping Control Approach. *IEEE TRANSACTIONS ON VEHICULAR TECHNOLOGY, VOL. 59, NO. 7*.

APPENDIX A – APPROACH TO FIND THE EULER PARAMETERS

The simulations made in this work were based on (Ambrósio & Verissimo, 2009). This article only gave access to the left-hand side elements of the car, stating that all the others, relative to the right-hand side, were symmetrical. This meant that Euler parameters for the right-hand side need to be computed. Unlike the centre of mass and relative position of the bodies and joints, the Euler parameters do not obey linearly a symmetrical transformation, so some computations need to be done. These computations were done with the help of (Nikravesh, 1988). Eq. (4.11) gives the transformation matrix expressed in terms of the Euler parameters. It is known that matrix, $\mathbf{A}$, can also be expressed in terms of cosines. These two formulations can be combined to find the actual Euler parameters, and vice-versa. So, (Nikravesh, 1988)

$$tr\mathbf{A} = 2(3e_0^2 + e_1^2 + e_2^2 + e_3^2) \tag{A.1}$$

With numerical computation and Eq. (4.9), (Nikravesh, 1988)

$$tr\mathbf{A} = 4e_0^2 - 1 \tag{A.2}$$

Solving to e_0

$$e_0^2 = \frac{tr\mathbf{A} + 1}{4} \tag{A.3}$$

Also, combining both transformation matrices,

$$a_{11} = 2(e_0^2 + e_1^2) - 1 \tag{A.4}$$

Substituting with Eq. (A.3)

$$a_{11} = 2\left(\frac{tr\mathbf{A} + 1}{4} + e_1^2\right) - 1 \tag{A.5}$$

The rest of the Euler parameters are given by (Nikravesh, 1988)

$$e_1^2 = \frac{1 + 2a_{11} - tr\mathbf{A}}{4} \tag{A.6}$$

$$e_2^2 = \frac{1 + 2a_{22} - tr\mathbf{A}}{4} \tag{A.7}$$

$$e_3^2 = \frac{1 + 2a_{33} - tr\mathbf{A}}{4} \tag{A.8}$$

The Euler parameters can be re-written as

$$e_1 = \frac{a_{32} - a_{23}}{4e_0} \tag{A.9}$$

$$e_2 = \frac{a_{13} - a_{31}}{4e_0} \tag{A.10}$$

$$e_3 = \frac{a_{21} - a_{12}}{e_0} \tag{A.11}$$

The previous equations correlate different ways of writing the same transformation matrix. The transformation matrix for the right-hand side components is not the same as for the left-hand side components. It is known that those components are symmetrical in relation to the y axis. Nevertheless, the new transformation matrix is not found by multiplying its middle column with -1. That would only represent a transformation in relation to the y axis, that would change the direction of z, which needs to be the same for both sides. That way, the right-hand side transformation matrix must be given by (Nikravesh, 1988)

$$\mathbf{A}_r = \begin{bmatrix} a_{11} & -a_{12} & a_{13} \\ -a_{21} & a_{22} & -a_{23} \\ a_{31} & -a_{32} & a_{34} \end{bmatrix} \tag{A.12}$$

By applying the previous methods to the new transformation matrix, the right-hand side Euler parameters can be calculated, as in Eq. (A.12).

APPENDIX B – EXTENDED EQUATIONS FOR THE MAGIC FORMULA

As was seen in the main body of this work, the tire model chosen to analyse the behaviour of the vehicle's tires was the Magic Formula, which is a semi-empirical model (Bakker et al., 1989; Bakker et al., 1987; Pacejka, 2002). The general formula of this model is only suited for pure longitudinal or lateral slip situations. A car usually drives with both types of slip at the same time, which creates a combined slip situation. To accommodate this, in (Pacejka, 2002), the equations for a combined slip situations are presented. In the current appendix, a survey of all equations used will be done.

Longitudinal Force for pure longitudinal slip (Pacejka, 2002),

$$F_{x0} = D_x \sin\left[C_x \arctan\left(B_x \cdot s - E_x(B_x \cdot s - \arctan(B_x \cdot s))\right)\right] + S_{Vx} \tag{B.1}$$

$$C_x = p_{Cx1} \tag{B.2}$$

$$D_x = \mu_x F_Z \tag{B.3}$$

$$\mu_x = (p_{Dx1} + p_{Dx2} df_Z) \tag{B.4}$$

$$E_x = (p_{Ex1} + p_{Ex2} \cdot df_Z + p_{Ex3} \cdot df_Z{}^2)(1 - p_{Ex4} \cdot \text{sgn}(s)) \tag{B.5}$$

$$B_x = k_{xk}/(C_x D_x + \varepsilon_x) \tag{B.6}$$

$$S_{Vx} = F_Z(p_{Vx1} + p_{Vx2} \cdot df_Z) \cdot |V_{Cx}|/(\varepsilon_{Vx} + |V_{Cx}|) \tag{B.7}$$

Lateral Force for pure lateral slip (Pacejka, 2002)

$$F_{y0} = D_y \sin\left[C_y \arctan\left(B_y \cdot \alpha - E_y(B_y \cdot \alpha - \arctan(B_y \cdot \alpha))\right)\right] + S_{Vy} \tag{B.8}$$

$$C_y = p_{Cy1} \tag{B.9}$$

$$D_y = \mu_y F_Z \tag{B.10}$$

$$\mu_y = (p_{Dy1} + p_{Dy2} df_Z)/(1 + p_{Dy3}\gamma^2) \tag{B.11}$$

$$E_y = (p_{Ey1} + p_{Ex2} \cdot df_Z)\left[1 + p_{Ey5}\gamma^2 - (p_{Ey3} + p_{Ey4}\gamma)\text{sgn}(\alpha)\right] \tag{B.12}$$

$$K_{y\alpha} = \frac{p_{Ky1}F_{Z0} \sin\left(p_{Ky4} \arctan\left(\frac{F_Z}{(p_{Ky2} + p_{Ky5}\gamma^2)F_{Z0}}\right)\right)}{(1 + p_{Ky3}\gamma^2)} \tag{B.13}$$

$$B_y = K_{y\alpha}/(C_y D_y + \varepsilon_y) \tag{B.14}$$

$$S_{Hy} = (p_{Hy1} + p_{Hy2} \cdot df_Z) + (K_{y\alpha o}\gamma - S_{Vy\gamma})/K_{y\alpha} \tag{B.15}$$

$$S_{Vy\gamma} = F_Z(p_{Vy3} + p_{Vy4}df_Z)\gamma \tag{B.16}$$

$$S_{Vy} = F_Z(p_{Vy1} + p_{Vy2}df_Z) + S_{Vy\gamma} \tag{B.17}$$

$$K_{y\gamma o} = F_Z(p_{Ky6} + p_{ky7}df_Z) \tag{B.18}$$

Aligning Torque (pure lateral slip) (Pacejka, 2002)

$$M_{z0} = M'_{z0} + M_{zr0} \tag{B.19}$$

$$M'_{z0} = -t_0 F_{y0} \tag{B.20}$$

$$t_0 = D_t \cos[C_t \arctan(B_t \cdot \alpha - E_t(B_t \cdot \alpha - \arctan(B_t \cdot \alpha)))] \cos(\alpha) \tag{B.21}$$

$$B_t = (q_{Bz1} + q_{Bz2} df_Z + q_{Bz3} df_Z{}^2)(1 + q_{Bz5}|\gamma^2|) \tag{B.22}$$

$$C_t = q_{Cz1} \tag{B.23}$$

$$D_{t0} = F_Z\left(\frac{r_0}{F_{Z0}}\right)(q_{Dz1} + q_{Dz2} df_Z)\text{sgn}(V_x) \tag{B.24}$$

$$D_t = D_{t0}(1 + q_{Dz3}|\gamma| + q_{Dz4}\gamma^2) \tag{B.25}$$

$$E_t = \left(q_{Ez1} + q_{Ez2} df_Z + q_{Ez3} df_Z{}^2\right)\left[1 + (q_{Ez4} + q_{Ez5}\gamma)\frac{2}{\pi}\arctan(B_t C_t \alpha)\right] \tag{B.26}$$

$$B_r = (q_{Bz9} + q_{Bz10} B_y C_y) \tag{B.27}$$

$$C_r = 1 \tag{B.28}$$

$$D_r = F_Z r_0[q_{Dz6} + q_{Dz7} df_Z + (q_{Dz8} + q_{Dz9} df_Z)\gamma + (q_{Dz10} + q_{Dz11} df_Z)\gamma|\gamma|]\cos(\alpha)\text{sgn}(V_x) \tag{B.29}$$

$$K_{y\alpha o} = D_{t0} K_{y\alpha} \tag{B.30}$$

$$K_{y\gamma o} = F_Z r_0 (q_{Bz8} + q_{Bz9} df_Z) - D_{t0} K_{y\gamma o} \tag{B.31}$$

Longitudinal Force (combined slip) (Pacejka, 2002)

$$F_x = G_{x\alpha} F_{x0} \tag{B.32}$$

$$G_{x\alpha} = \cos\left[G_{x\alpha} \arctan(B_{x\alpha}\alpha - E_{x\alpha}(B_{x\alpha}\alpha - \arctan(B_{x\alpha}\alpha)))\right] \tag{B.33}$$

$$G_{x\alpha 0} = \cos\left[G_{x\alpha} \arctan(B_{x\alpha}S_{Hx\alpha} - E_{x\alpha}(B_{x\alpha}S_{Hx\alpha} - \arctan(B_{x\alpha}S_{Hx\alpha})))\right] \tag{B.34}$$

$$B_{x\alpha} = (r_{Bx1} + r_{Bx3}\gamma^2)\cos\left[\arctan(r_{Bx2}s)\right] \tag{B.35}$$

$$C_{x\alpha} = r_{Cx1} \tag{B.36}$$

$$E_{x\alpha} = r_{Ex1} + r_{Ex2} df_Z \tag{B.37}$$

$$S_{Hx\alpha} = r_{Hx1} \tag{B.38}$$

Lateral Force (combined slip) (Pacejka, 2002)

$$F_y = G_{ys} F_{y0} \tag{B.39}$$

$$G_{ys} = \cos\left[G_{ys} \arctan\left(B_{ys}s - E_{ys}\left(B_{ys}s - \arctan(B_{ys}s)\right)\right)\right]/G_{ys0} \tag{B.40}$$

$$G_{ys0} = \cos\left[G_{ys} \arctan(B_{ys}S_{Hys} - E_{ys}(B_{ys}S_{Hys} - \arctan(B_{ys}S_{Hys})))\right] \tag{B.41}$$

$$B_{ys} = \left(r_{By1} + r_{By4}\gamma^2\right)\cos\left[\arctan(r_{By2}(\alpha - r_{By3}))\right] \tag{B.42}$$

$$C_{ys} = r_{Cy1} \tag{B.43}$$

$$E_{ys} = r_{Ey1} + r_{Ey2} df_Z \tag{B.44}$$

$$S_{Hys} = r_{Hx1} + r_{Hy2} df_Z \tag{B.45}$$

$$D_{Vys} = \mu_y F_Z (r_{Vy1} + r_{Vy2} df_Z + r_{Vy3}\gamma)\cos\left[\arctan\left(r_{Vy4}\alpha\right)\right] \tag{B.46}$$

Overturning Couple (Pacejka, 2002)

$$M_x = F_Z r_0 (q_{sx1} - q_{sx2}\gamma + q_{sx3}F_y/F_{Z0}) \tag{B.47}$$

Rolling Resistance (Pacejka, 2002)

$$M_y = -F_Z r_0 \left(q_{sy1}\arctan\left(\frac{r_{dyn}w_s}{\|\mathbf{V}_T\|}\right) + q_{sy2}F_x/F_{Z0} \right) \tag{B.48}$$

Aligning Torque (combined slip) (Pacejka, 2002)

$$M_z = M_z' + M_{zr} + sF_x \tag{B.49}$$

$$M_z' = -t_0 F_y \tag{B.50}$$

$$M_{zr} = D_r \cos\left[C_r \arctan\left(B_r\alpha\right)\right] \tag{B.51}$$

$$s_y = r_0\big(s_{sz1} + s_{sz1}\big(F_y/F_{Z0}\big) + (s_{sz3} + s_{sz4}df_Z)\gamma\big) \tag{B.52}$$

APPENDIX C – CORRECTION OF INITIAL CONDITIONS

Multibody systems are usually defined by a set of initial conditions, that indicate the position and velocity of the bodies in the first instant of simulation. In fact, a set of initial conditions is necessary to solve the equations of motion of a system (Flores P. , 2015). Many times, the initial conditions of a particular system are inaccurate and make up a bad representation of that system's initial state. Constraints violations appear during long simulations, due to inaccurate initial conditions and bad integration (Marques et al., 2017). To avoid this problem several methods were created, although in this work the method proposed in (Flores P. , 2015; Nikravesh, 2007) will be used.

Let us start to cite Eq. (4.16), also known as constraint equation. The initial conditions for the position level are given as $\mathbf{q}^0$. If it does not satisfy Eq. (4.16), then corrections need to be made (Flores P. , 2015). The corrected positions are given as (Flores P. , 2015)

$$\mathbf{q}^c = \mathbf{q}^0 + \delta\mathbf{q} \tag{C.1}$$

So

$$\mathbf{\Phi}(\mathbf{q}^c) = \mathbf{\Phi}(\mathbf{q}^0) + \delta\mathbf{\Phi} = 0 \tag{C.2}$$

Through mathematical manipulation Flores (2015) states that

$$\delta\mathbf{q} = -\mathbf{D}^T(\mathbf{D}\mathbf{D}^T)^{-1}\mathbf{\Phi}(\mathbf{q}^0) \tag{C.3}$$

Eq. (C.3) must be solved iteratively. (Flores P. , 2015; Nikravesh, 2007) use a Newton-Raphson algorithm (Kahaner, 1988) to solve it. With such kind of algorithm, only a few numbers of iterations are necessary for a result to converge. For $\mathbf{q} = \mathbf{q}^i$

$$\mathbf{\Phi}(\mathbf{q}^i) = 0 \tag{C.4}$$

is evaluated.

If $\mathbf{q}^i$ does not satisfy the previous condition, then (Flores P. , 2015)

$$\delta\mathbf{q}^i = -\mathbf{D}^T(\mathbf{D}\mathbf{D}^T)^{-1}\mathbf{\Phi}(\mathbf{q}^i) \tag{C.5}$$

is computed. The correction is made as

$$\mathbf{q}^{i+1} = \mathbf{q}^i + \delta\mathbf{q}^i. \tag{C.6}$$

If there is no convergence, the process needs to be repeated.

With the positions level initial conditions corrected, the velocity level is corrected using the same method. The corrected velocities are given by

$$\mathbf{v}^c = \mathbf{v}^0 + \delta\mathbf{v} \tag{C.7}$$

Flores (2015) states that

$$\mathbf{v}^c = \mathbf{v}^0 - -\mathbf{D}^T(\mathbf{D}\mathbf{D}^T)^{-1}\dot{\boldsymbol{\Phi}}(\mathbf{q}^c, \mathbf{v}^0) \qquad\qquad (C.8)$$

ANNEX A – MAGIC FORMULA PARAMETERS

$R_o(=r_o) = 0.313\text{m}$, $\quad F_{z0}(=F_{N0}) = 4000\text{N}$, $\quad m_o = 9.3\text{kg}$, $\quad V_o = 16.67\text{m/s}$

$p_{Cx1} = 1.685$	$p_{Dx1} = 1.210$	$p_{Dx2} = -0.037$	$p_{Ex1} = 0.344$	$p_{Ex2} = 0.095$
$p_{Ex3} = -0.020$	$p_{Ex4} = 0$	$p_{Kx1} = 21.51$	$p_{Kx2} = -0.163$	$p_{Kx3} = 0.245$
$p_{Hx1} = -0.002$	$p_{Hx2} = 0.002$	$p_{Vx1} = 0$	$p_{Vx2} = 0$	
$r_{Bx1} = 12.35$	$r_{Bx2} = -10.77$	$r_{Bx3} = 0$	$r_{Cx1} = 1.092$	$r_{Hx1} = 0.007$
$q_{sx1} = 0$	$q_{sx2} = 0$	$q_{sx3} = 0$		
$p_{Cy1} = 1.193$	$p_{Dy1} = -0.990$	$p_{Dy2} = 0.145$	$p_{Dy3} = -11.23$	$p_{Ey1} = -1.003$
$p_{Ey2} = -0.537$	$p_{Ey3} = -0.083$	$p_{Ey4} = -4.787$	$p_{Ky1} = -14.95$	$p_{Ky2} = 2.130$
$p_{Ky3} = -0.028$	$p_{Ky4} = 2$	$p_{Ky5} = 0$	$p_{Ky6} = -0.92$	$p_{Ky7} = -0.24$
$p_{Hy1} = 0.003$	$p_{Hy2} = -0.001$	$p_{Hy3} = 0$		
$p_{Vy1} = 0.045$	$p_{Vy2} = -0.024$	$p_{Vy3} = -0.532$	$p_{Vy4} = 0.039$	
$r_{By1} = 6.461$	$r_{By2} = 4.196$	$r_{By3} = -0.015$	$r_{By4} = 0$	$r_{Cy1} = 1.081$
$r_{Hy1} = 0.009$	$r_{Vy1} = 0.053$	$r_{Vy2} = -0.073$	$r_{Vy3} = 0.517$	$r_{Vy4} = 35.44$
$r_{Vy5} = 1.9$	$r_{Vy6} = -10.71$			
$q_{Bz1} = 8.964$	$q_{Bz2} = -1.106$	$q_{Bz3} = -0.842$	$q_{Bz5} = -0.227$	$q_{Bz6} = 0$
$q_{Bz9} = 18.47$	$q_{Bz10} = 0$	$q_{Cz1} = 1.180$	$q_{Dz1} = 0.100$	$q_{Dz2} = -0.001$
$q_{Dz3} = 0.007$	$q_{Dz4} = 13.05$	$q_{Dz6} = -0.008$	$q_{Dz7} = 0.000$	$q_{Dz8} = -0.296$
$q_{Dz9} = -0.009$	$q_{Dz10} = 0$	$q_{Dz11} = 0$		
$q_{Ez1} = -1.609$	$q_{Ez2} = -0.359$	$q_{Ez3} = 0$	$q_{Ez4} = 0.174$	
$q_{Ez5} = -0.896$	$q_{Hz1} = 0.007$	$q_{Hz2} = -0.002$	$q_{Hz3} = 0.147$	$q_{Hz4} = 0.004$
$s_{sz1} = 0.043$	$s_{sz2} = 0.001$	$s_{sz3} = 0.731$	$s_{sz4} = -0.238$	
$q_{Iay} = 0.109$	$q_{ma} = 0.237$	$q_{cbx0,z} = 121.4$	$q_{kbx,z} = 0.228$	$q_{cb\theta0} = 61.96$
$q_{Iaxz} = 0.071$	$q_{mb} = 0.763$	$q_{cby} = 40.05$	$q_{kby} = 0.284$	$q_{cby,\psi} = 20.33$
$q_{Iby} = 0.696$	$q_{mc} = 0.108$	$q_{ccx} = 391.9$	$q_{kcx} = 0.910$	$q_{ccy} = 55.82$
$q_{Ibxz} = 0.357$		$q_{ccy} = 62.7$	$q_{kcy} = 0.910$	$q_{kb\theta} = 0.080$
$q_{Ic} = 0.055$				$q_{kby,\psi} = 0.038$
				$q_{kcy} = 0.834$
$q_{V1} = 7.1 \times 10^{-5}$	$q_{F23} = 0$	$q_{a1} = 0.135$	$B_{reff} = 9$	$q_{Fcx1} = 0.1$
$q_{V2} = 2.489$	$q_{sy1} = 0.01$	$q_{a2} = 0.035$	$D_{reff} = 0.23$	$q_{Fcy1} = 0.3$
$q_{Fz1} = 13.37$	$q_{sy3} = 0$	$q_{bvx,z} = 3.957$	$F_{reff} = 0.01$	$q_{Fcx2} = 0$
$q_{Fz2} = 14.35$	$q_{sy4} = 0$	$q_{bv\theta} = 3.957$		$q_{Fcy2} = 0$

This table was directly adapted from (Pacejka, 2002).

ANNEX B – POWER/TORQUE CURVES FOR A SMALL FAMILY CAR
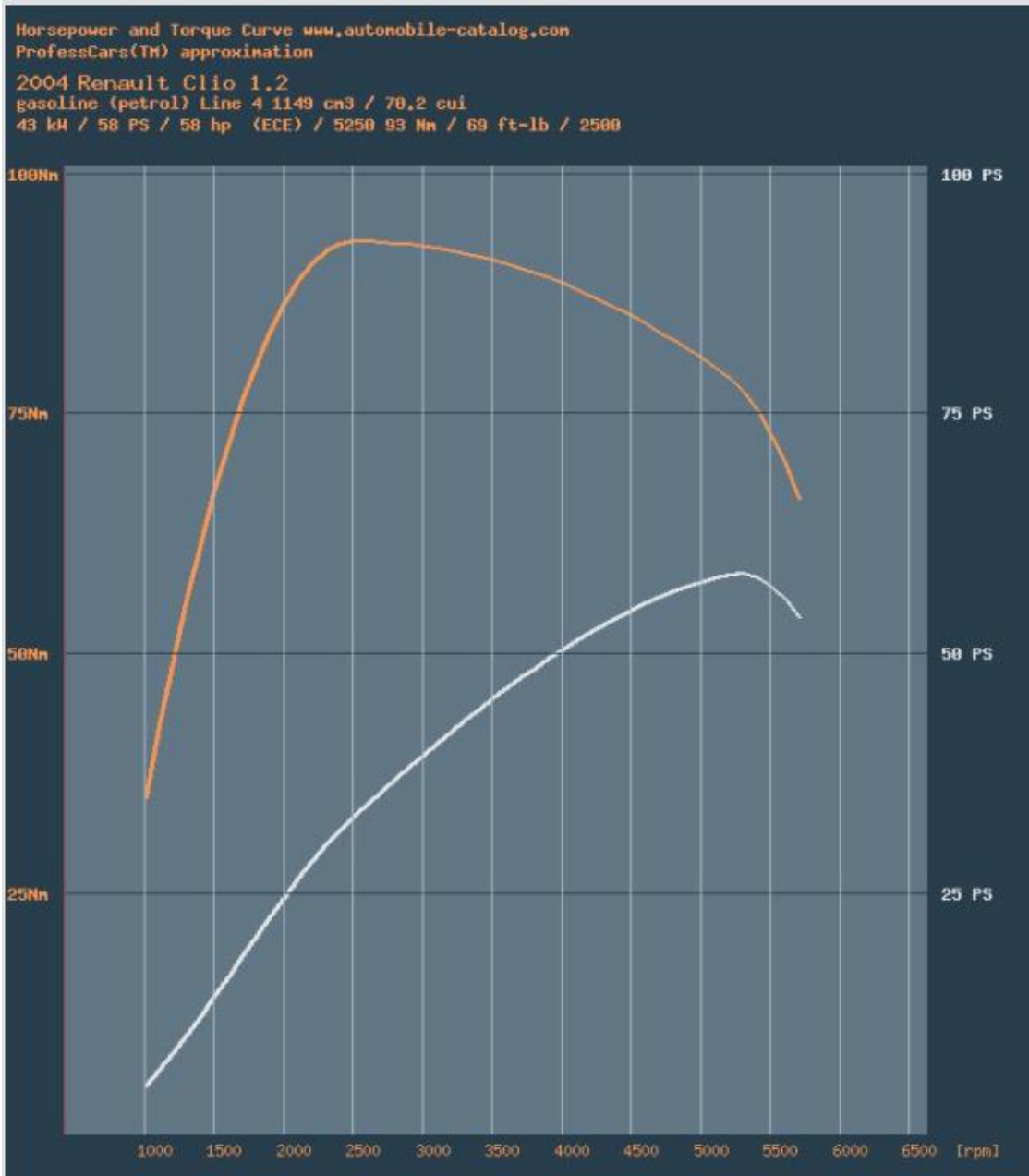
These curves were directly adapted from (Zal, s.d.).